Chakkrapong Chaiburi, M.Eng., M.Sc.

Decrease of fuel cell performance caused by coolant leakage

DOCTORAL THESIS

to achieve the university degree of

Doktor der technischen Wissenschaften

submitted to

Graz University of Technology

Supervisor

Assoc.Prof. Dipl.-Ing. Dr.techn. Viktor Hacker

Institute of Chemical Engineering and Environmental Technology

Faculty of Technical Chemistry, Chemical and Process Engineering, Biotechnology

Graz, October 2016

AFFIDAVIT

I declare that I have authored this thesis independently, that I have not used other than the declared sources/resources, and that I have explicitly indicated all material which has been quoted either literally or by content from the sources used. The text document uploaded to TUGRAZonline is identical to the present doctoral thesis.

Date

Signature

TABLE OF CONTENTS

ACKNOWLEDGMENTS

First, I would like to thank my advisor Assoc. Prof. Dipl.-Ing. Dr. techn. Viktor Hacker for the opportunity to work in Fuel Cell Group, Institute of Chemical Engineering and Environmental Technology, Graz University of Technology and also thanks for advice and guidance.

I would like to acknowledge my lab-mates Bernd Cermenek, Christoph Grimmer, Alexander Schenk, Stephan Weinberger and Birgit Pichler for assistance, discussion and sharing their experience.

I also would like to thank Gernot Voitic for general information, advice and sharing his experience and Sudkate Chaiyo for TEM and EDX results.

Next, I would like to thank Royal Thai Government scholarship for the opportunity to study in Fuel Cell Group, Institute of Chemical Engineering and Environmental Technology, Graz University of Technology.

Finally, thanks to my wife Suchada, my daughter Donut, my son Namo and my family for support, stand with me and walk together.

Thank you very much

“A Person Who Never Made a Mistake, Never Tried Anything New”

Albert Einstein

Abstract

In a fuel cell, the catalyst on the anode side facilitates the oxidation of hydrogen, which releases electrons. Subsequently, the electrons are utilized as electric current and transported to the cathode via an external load. The catalyst on the cathode side receives these electrons and catalyzes the reduction of oxygen. The only by-products of these electrochemical reactions are heat and water. The most common methods for heat removal from the fuel cell stack include air-cooling and liquid-cooling using water, ethylene glycol or a combination of these two liquids as coolant. In the case of coolant leakage, when the cell compartment is not appropriately sealed or leaks occur, glycol-based coolants could come into contact with the Pt based electrocatalyst of the fuel cell. The ethylene glycol based coolant interacts with the electrocatalyst and thereby influences the performance of proton exchange membrane fuel cells (PEMFCs). In the current study, the performance degradation of the fuel cell catalyst regarding the catalyst surface area and the activity towards the oxygen reduction reaction (ORR) was investigated by mean of cyclic voltammetry (CV). The loss of Pt electrochemical surface area (ECSA) was determined and respective methods for mitigating the negative effects were investigated. Electrodes contaminated with coolant showed extremely poor catalytic activity for the oxygen reduction reaction (ORR) due to side reactions such as ethylene glycol oxidation. By adding Triton-X as non-ionic surfactant to the coolant the electrooxidation rate of ethylene glycol was lowered. The Triton-X prevents CO formation from the ethylene glycol oxidation, thus reduces the poisoning of the Pt catalyst surface during coolant contamination.

High ORR activity and ethanol-tolerance with varied molar concentrations of ethanol at different temperature were obtained with Ag/C, MnO_2/C, $Ag_2V_4O_{11}$/C, V_2O_5/C and $AgMnO_2$/C electrocatalysts (Section 2). The electrocatalysts structure and compositions were investigated by transmission electron microscopy (TEM) and X-ray spectroscopy (EDX). TEM images exhibited aggregated-spherical and branch-like morphologies. At different temperatures, the ORR electrocatalysts showed reasonable ethanol-tolerance in case of ethanol crossover through membranes from anode to cathode compartments or in the presence of ethanol in liquid KOH electrolyte. The $AgMnO_2$/C catalyst proved significant ethanol tolerance and thus the highest activity and current density were obtained with this catalyst during investigations.

Kurzfassung

In Brennstoffzellen ermöglicht der Katalysator auf der Anode die Oxidation von Wasserstoff, wodurch Elektronen freigesetzt werden. Diese Elektronen werden anschließend über einen externen Verbraucher zur Kathode geleitet und als elektrische Energie genützt. Der Katalysator an der Kathode reduziert den Sauerstoff mithilfe der zugeführten Elektronen. Als Nebenprodukte dieser elektrochemischen Reaktionen entsteht Wärme und Wasser. Die am häufigsten eingesetzten Verfahren zur Abfuhr der überschüssigen Wärme sind die Kühlung mit Luft oder der Einsatz von flüssigen Kühlmedien, wie Wasser oder Ethylen-Glykol beziehungsweise ein Gemisch der beiden Kühlflüssigkeiten. Im Fall einer Kühlflüssigkeitsleckage kann es zum Kontakt der Platin- Elektrokatalysatoren mit dem Kühlmedium kommen. Ein auf Ethylen-Glykol basierendes Kühlmedium wechselwirkt mit dem Katalysator und beeinflusst die Leistungsfähigkeit einer PEM-Brennstoffzelle. In der vorliegenden Arbeit wurde die Abnahme der Leistungsfähigkeit von Brennstoffzellenkatalysatoren mittels zyklischer Voltametrie (CV) untersucht. Der Fokus wurde dabei auf den Rückgang der katalytischen Oberfläche und auf die Abnahme der katalytischen Aktivität zur Sauerstoffreduktion gelegt. Der Verlust an Platin-Oberfläche wurde bestimmt und Methoden zur Abschwächung der negativen Effekte erarbeitet. Elektroden, welche mit Kühlflüssigkeit kontaminiert wurden, zeigten eine extrem niedrige katalytische Aktivität zur Sauerstoffreduktion (ORR). Diese wurde durch die Nebenreaktionen, wie die Oxidation des Ethylen-Glykols verursacht. Der Zusatz von Triton-X, einem nicht-ionischen Tensid, zum Kühlmittel konnte die elektrochemische Oxidation von Ethylen-Glykol reduzieren. Triton-X verhindert die Bildung von CO aus Ethylen-Glykol, wodurch die Pt-Katalysatorvergiftung, im Falle einer Kühlmittelkontamination, vermieden wird.

Eine hohe ORR-Aktivität und Ethanol-Toleranz bei unterschiedlichen Ethanolkonzentrationen und verschiedenen Temperaturen wurde mit elektrochemischen Katalysatoren Ag/C, MnO_2/C, $Ag_2V_4O_{11}$/C, V_2O_5/C und $AgMnO_2$/C erreicht. Die Struktur und Zusammensetzung dieser Katalysatoren wurden mithilfe von Transmissions-Elektronen Mikroskopie (TEM) und energiedispersive Röntgenspektroskopie (EDX) analysiert. Die TEM-Aufnahmen zeigten sphärische Aggregate und verästelte Strukturen. Im Falle eines Ethanoldurchtritts von der Anode zur Kathode durch die Membran beziehungsweise bei Anwesenheit von Ethanol im flüssigen KOH-Elektrolyt konnte bei unterschiedlichen Temperaturen eine zufriedenstellende Ethanol-Toleranz des Katalysators nachgewiesen werden. Der Katalysator aus $AgMnO_2$/C zeigt eine stark verbesserte Ethanol-Toleranz, wodurch die höchste Aktivität und Stromdichte bei den Versuchen erzielt werden konnte.

1. Introduction

Different types of fuel cells have been designed for different kinds of fuel for continuous conversion from electrochemical reaction to electrical energy. The key components of a fuel cell include the cathode, anode and membrane. The reaction is an electrochemical process at the anode consisting of oxidation and reduction reactions occurring at the cathode. The flow of electrons occurs simultaneously. A fuel cell stack consists of several individual cells in a series. Fuel cells possess the benefit of creating minimal noise pollution. However, power for the fuel cell also requires modification as well as improvement on several points such as the security of the system, electrocatalysts, and more efficient storage of raw materials. Various causes can account for performance loss during the operation of a fuel cell, including exposure to impurities. On the cathode side, impurities of interest include coolant and alcohol. Such impurities are adsorbed on the surface of electrocatalyts, which block and prevent the adsorption of new oxygen molecules at the cathode compartment.

1.1 Research Objectives

Section 1: Performance decrease of platinum fuel cell catalyst by coolant leakage

This section studies the influence of glycol-based coolant formulations such as glycol/water and glycol/water/Triton-X on the activity of Pt/C electrocatalysts when coolant leakage occurs in the system. The investigations were performed with ex-situ cyclic cyclic voltammetry (CV), rotating disk electrode (RDE) and oxygen reduction reaction (ORR) method.

Section 2: Investigation of decrease of performance of non-Pt based electrocatalysts during ethanol leakage

Non Pt-based electrocatalysts are investigated for their tolerance towards ethanol in alkaline direct ethanol fuel cells. In this section electrochemical methods are employed from the ex-situ of CV, RDE and ORR in order to study the catalytic properties of used materials.

2. Fundamental

2.1 Type of Fuel Cells

Several fuel cell technologies exist, which are customarily classified by the kind of the electrolyte employed, the kind of electrocatalysts required, and the temperature range, as well as the kind of electrochemical reactions occurring in the fuel cell.

2.1.1 Proton Exchange Membrane Fuel Cells (PEMFCs)

The polymer electrolyte membrane in this fuel cell is a fluorinated sulfonic acid polymer or other similar polymer such as Nafion, which is a good proton conductor and electrically insulating. The anode reaction involves the oxidation of hydrogen and the cathode reaction involves the reduction of oxygen. The only liquid in this fuel cell is water-formed on the cathode side as a by-product of the reaction. The electrode reactions and the overall reaction in the PEMFC are given below.

Anode:	H_2	$\rightarrow$	$2H^+ + 2e^-$	E^0	=	0 V	(1)
Cathode:	$1/2O_2 + 2H^+ + 2e^-$	$\rightarrow$	H_2O	E^0	=	1.23 V	(2)
Over all reaction:	$H_2 + 1/2O_2$	$\rightarrow$	H_2O	E^0	=	1.23 V	(3)

At the anode of the PEMFCs hydrogen (H_2) is consumed, which is usually stored fuel in high-pressure hydrogen tanks or metal hydride containers. The H_2 fuel is released into the anode channel with the required pressure, flow rate, temperature, and humidification. At the cathode, the oxygen is supplied directly from atmospheric air. (Gasteiger *et al*., 2009).

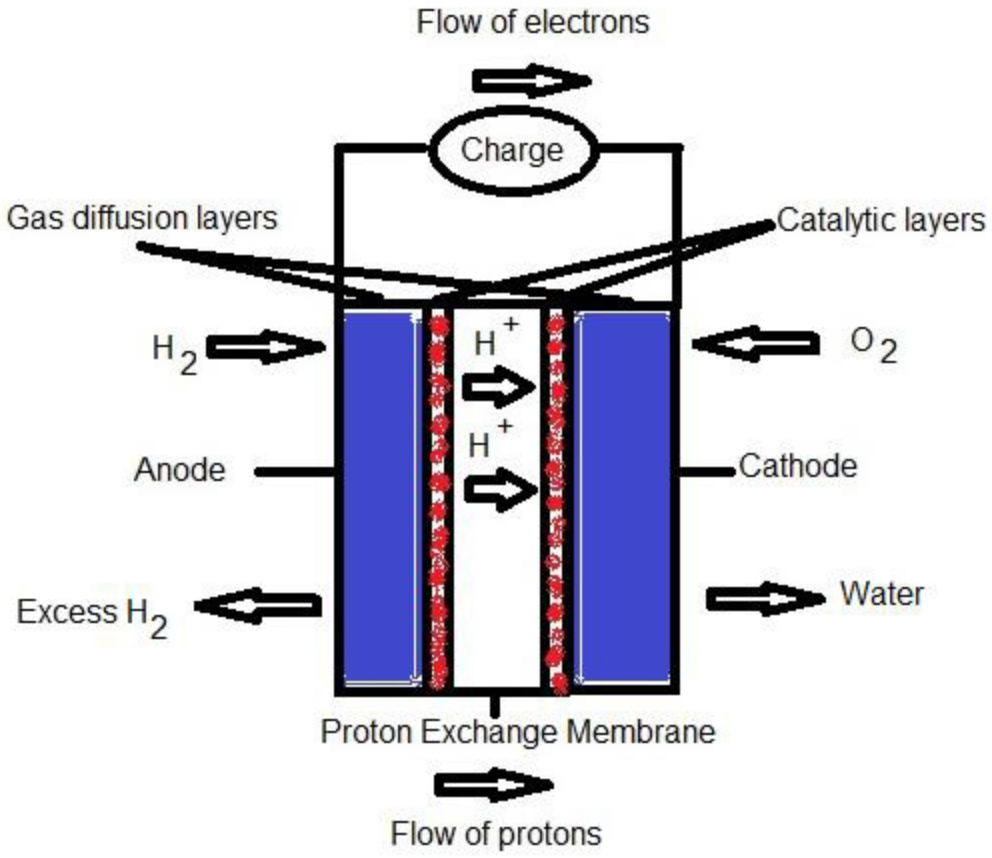

Fig.1. Proton exchange membrane fuel cells (PEMFCs)

2.1.2 Direct Methanol Fuel Cells (DMFCs):

The electrodes as anode and cathode are in collaboration with the ion exchange membrane. The electrocatalysts are coated on the electrode layer, which is a mixture of electrocatalyst and ionomer. Activated carbon is often used to supported materials for active sites of electrocatalysts. The membrane is a perfluorosulfonic acid polymer. Oxygen molecules migrate via the diffusion layer to active sites on the cathode side. This layer is a mixture of carbon and polytetrafluoroethylene (Teflon), as well as hydrophobic properties. The anode is fed directly by a mixture of methanol with water. Methanol displays a methanol oxidation reaction to carbon dioxide (CO_2) and possible formation materials such as formaldehyde, formic acid and other organic compounds. The cathode feed the inlet of humidified oxygen to the system. The overall reaction process for a protonic electrolyte is outlined below (Liu *et al*., 2009):

Anode: $CH_3OH + H_2O \rightarrow CO_2 + 6H^+ + 6e^-$ $E^0 = 0.02V$ (4)

Cathode: $3/2O_2 + 6H^+ + 6e^- \rightarrow 3H_2O$ $E^0 = 1.23V$ (5)

Overall reaction: $CH_3OH + 3/2O_2 \rightarrow CO_2 + 2H_2O$ $E^0 = 1.21V$ (6)

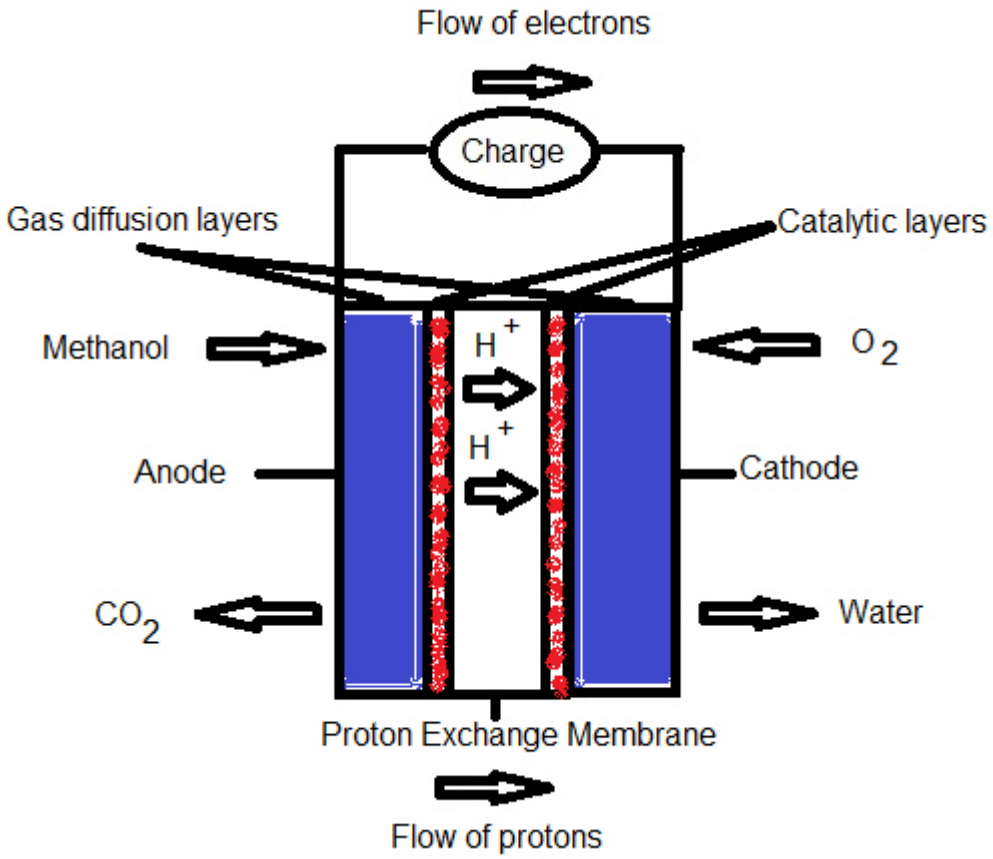

Fig. 2. Direct methanol fuel cells (DMFCs) in an acid medium

The reaction of alkaline electrolyte based DMFCs can be exhibited as follows (Liu *et al*., 2009):

Anode: $CH_3OH + 6OH^- \rightarrow CO_2 + 5H_2O + 6e^-$ $E^0 = -0.81V$ (7)

Cathode: $3/2O_2 + 3H_2O + 6e^- \rightarrow 6OH^-$ $E^0 = 0.402V$ (8)

Overall reaction: $CH_3OH + 3/2O_2 \rightarrow CO_2 + 2H_2O$ $E^0 = 1.21V$ (9)

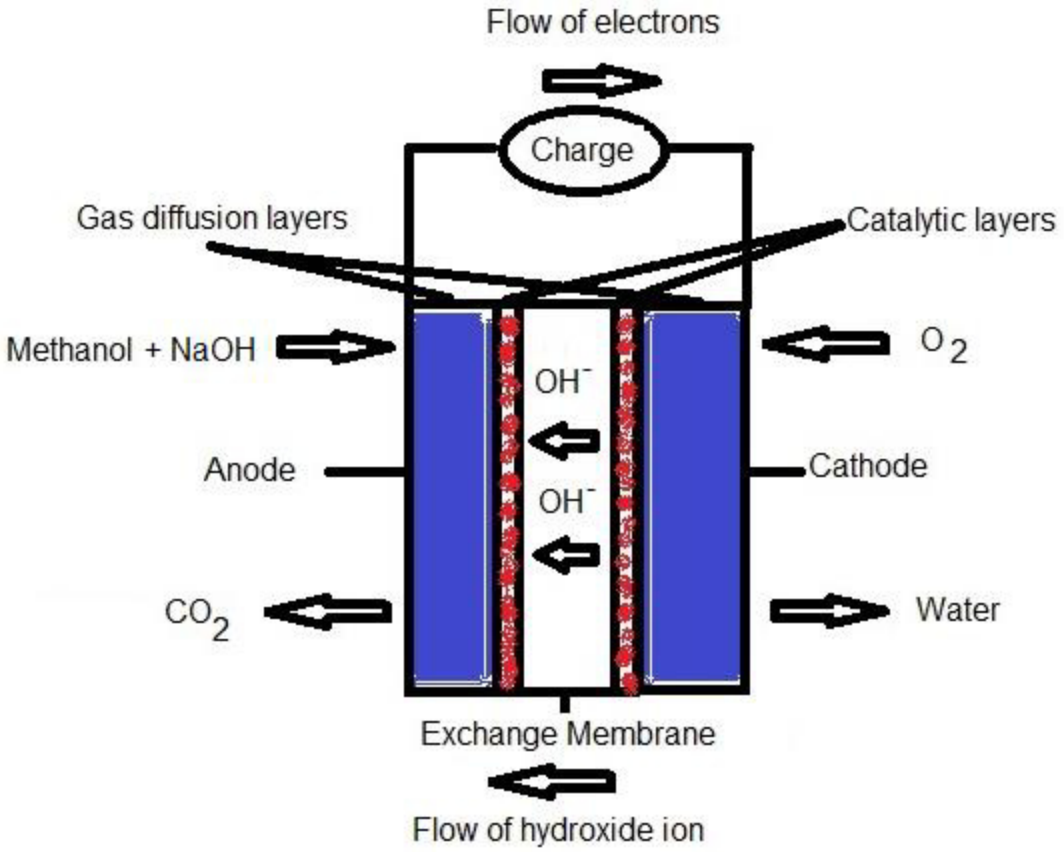

Fig. 3. Direct methanol fuel cells (DMFCs) in alkaline medium

2.1.3 Direct Ethanol Fuel Cells (DEFCs)

In acid medium

The principle of the DEFC process is displayed in Figure 4. The anode and cathode contain an ethanol solution and humidified air or oxygen, respectively. Ethanol produces carbon dioxide via an oxidation reaction, which generates protons and electrons in the anode compartment. Protons move through the membrane to the cathode side, where the electrocatalysts on the cathode react with oxygen and electrons to create water (Eqs. (7) – (9)).

Anode: $CH_3CH_2OH + 3H_2O \rightarrow 2CO_2 + 12H^+ + 12e^-$ $E^0 = 0.084V$ (10)

Cathode: $3O_2 + 12H^+ + 12e^- \rightarrow 6H_2O$ $E^0 = 1.223V$ (11)

Over all reaction: $CH_3CH_2OH + 3O_2 \rightarrow 2CO_2 + 3H_2O$ $E^0 = 1.145V$ (12)

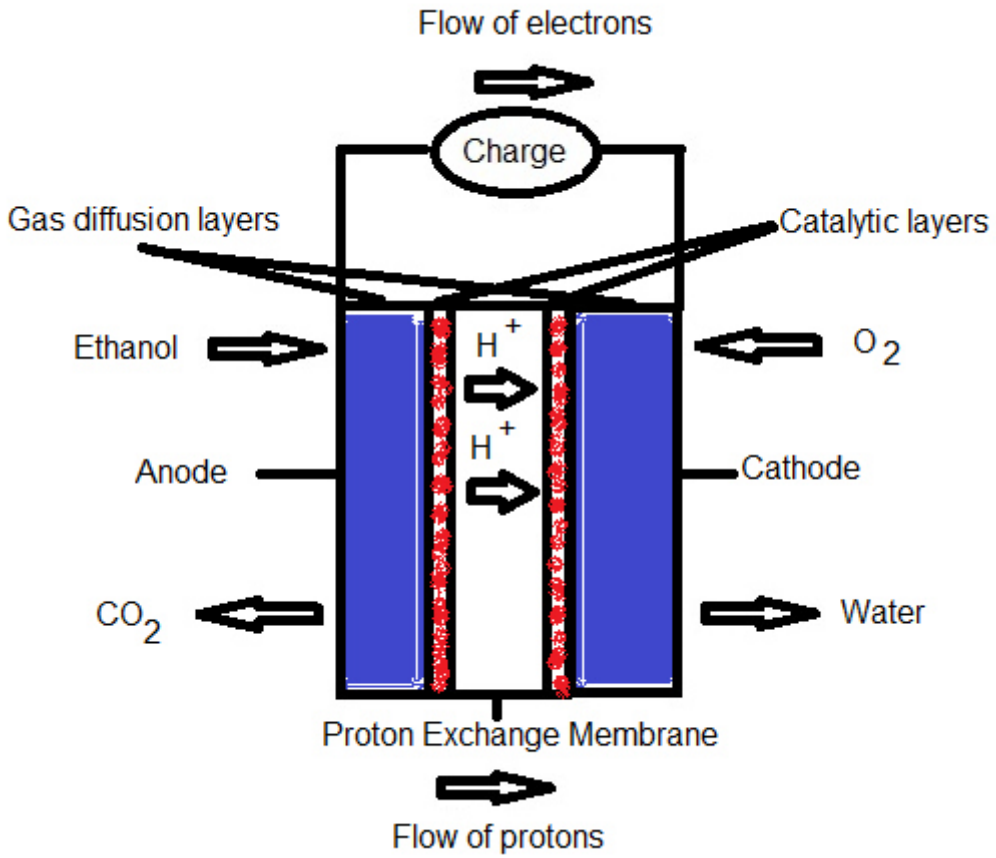

Fig. 4. Direct ethanol fuel cells (DEFCs) in an acid medium

This process releases 12 electrons for the complete oxidation of ethanol to CO_2, which shows the maximum theoretical density energy. At a temperature below 120 °C in membrane, the process is related to the slow kinetics of an oxygen reduction reaction (ORR). On the other hand, strong adsorption with the ethanol intermediate via oxidation reaction onto the Pt electrocatalyst, which conducts less efficient energy in the fuel cell system (Lamy *et al*., 2004, Antolini, 2007). The ethanol oxidation reaction for application in direct ethanol fuel cells was recognised (Delime *et al*., 1998, Wang *et al*., 1995). Different mechanisms for ethanol oxidation reaction were proposed in literature (Vigier *et al*., 2004, Kutz *et al*., 2011).

$$CH_3CH_2OH \rightarrow [CH_3CH_2OH]_{ads} \rightarrow CO_2 \quad \text{(total oxidation)} \quad (13)$$

$$CH_3CH_2OH \rightarrow [CH_3CH_2OH]_{ads} \rightarrow CH_3CHO \rightarrow CH_3COOH \quad \text{(partial oxidation)} \quad (14)$$

In alkaline medium

The operation principle of an alkaline direct ethanol fuel cell (DEFC) is exhibited in Figure 5. On the anode side, a mixture of ethanol and NaOH or KOH is applied. On the cathode, humidified oxygen (air) is a mixture of air with moisture moving to the system. Due to an ethanol oxidation reaction, carbon dioxide and electrons are generated on the anode, while hydroxide ions are produced from the reaction of oxygen with electrons on the cathode side. Next, hydroxide ions are transferred to the anode side through the electrolyte. According to the above, the electrocatalyst of a fuel cell has been made to improve and enable the application of this type of electronic device. The equations for an alkaline direct ethanol fuel cell are shown below (Modestov *et al*., 2009):

Anode : $CH_3CH_2OH + 12OH^- \rightarrow 2CO_2 + 9H_2O + 12e^-$ $E^0 = -0.74V$ (15)

Cathode : $3O_2 + 6H_2O + 12e^- \rightarrow 12OH^-$ $E^0 = 0.40V$ (16)

Over all reaction: $CH_3CH_2OH + 3O_2 \rightarrow 2CO_2 + 3H_2O$ $E^0 = 1.24V$ (17)

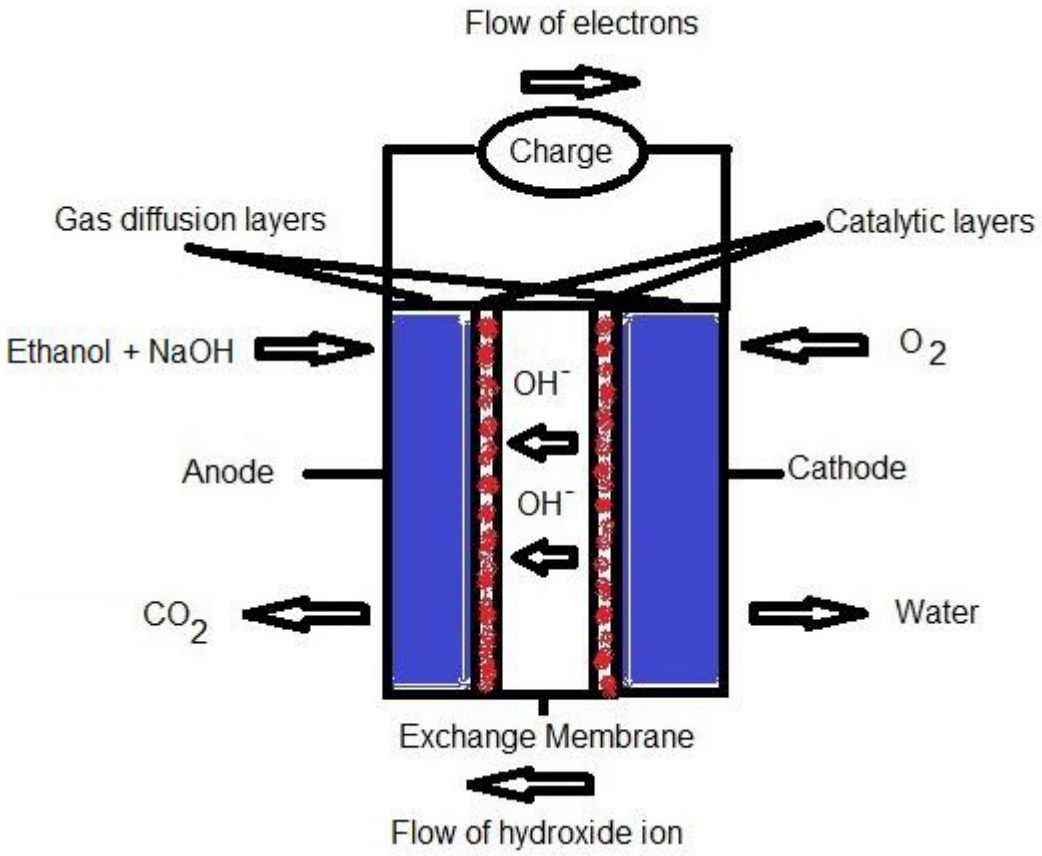

Fig. 5. Direct ethanol fuel cells (DEFCs) in alkaline medium

The electrochemical reaction in an alkaline medium is more efficient than in an acidic medium (Parsons *et al*., 1988, Spendelow *et al*., 2007, Yu *et al*., 2010). However, this system in fuel cell technology does not support improvements in electrocatalysts, with high catalytic efficiency of ethanol oxidation reaction transferring to the carbonation of the alkaline electrolyte as CO_2 formed. This formed reacts with OH^- generating CO_3^{-2} in the alkaline electrolyte. Then carbonate salts precipitate on the electrode, thereby blocking the active sites of electrocatalysts (Gulzow, 1996). Therefore, high reactivity of the system is displayed as the initial system reduces fuel (Wang *et al*., 2003). Many researchers have been studying the ethanol oxidation mechanism in an alkaline medium. In the literature, the mechanism for ethanol oxidation is complex. However, possible mechanism proposal is carried out during the oxidation reaction, which generates by products (Jiang *et al*., 2010, Lai *et al*., 2009, Lai *et al*., 2010).

2.1.4 Alkaline Acid Direct Ethanol Fuel Cells (AADEFCs)

The rapid poisoning of active sites on Pt electrocatalysts reduces cell performance. Likewise, the kinetics for both oxygen reduction (ORR) and ethanol oxidation reaction (OER) in an alkaline medium are more enhanced than in an acidic medium. The chemical and physical properties are limitations of system performance (Varcoe *et al*., 2005). As previously reported, An et al. developed new direct alcohol fuel cells, with higher performance than DEFCs working in acid or alkaline medium by using mixture of NaOH with ethanol at the anode side and mixture of sulfuric acid with hydrogen peroxide (H_2O_2) instead of humidified oxygen, on the cathode side (An *et al*., 2011). With H_2O_2, the operation of AADEFCs showed lower activation loss in the system, which was absent of the reduction reaction through $2e^-$ transfer, not to mention water flooding (Miley *et al*., 2007). The AADEFCs include an anode, cathode (inlet as alkaline and acid solution, respectively) and cation exchange membrane separator (An *et al*., 2011). The basic medium (NaOH) initially oxidises, ethanol into CO_2 in the anode compartment (shown in Eq. (18)). Hydrogen peroxide (H_2O_2) disintegrates into water (H_2O) in the presence of the H_2SO_4 solution on the cathode side, (Eq. (19)).

Anode : $CH_3CH_2OH + 12OH^- \rightarrow 2CO_2 + 9H_2O + 12e^-$ $E^0 = -0.74V$ (18)

Cathode : $6\,H_2O_2 + 12H^+ + 12e^- \rightarrow 12H_2O$ $E^0 = 1.78V$ (19)

Over all reaction: $CH_3CH_2OH + 6\,H_2O_2 \rightarrow 2CO_2 + 9H_2O$ $E^0 = 2.52V$ (20)

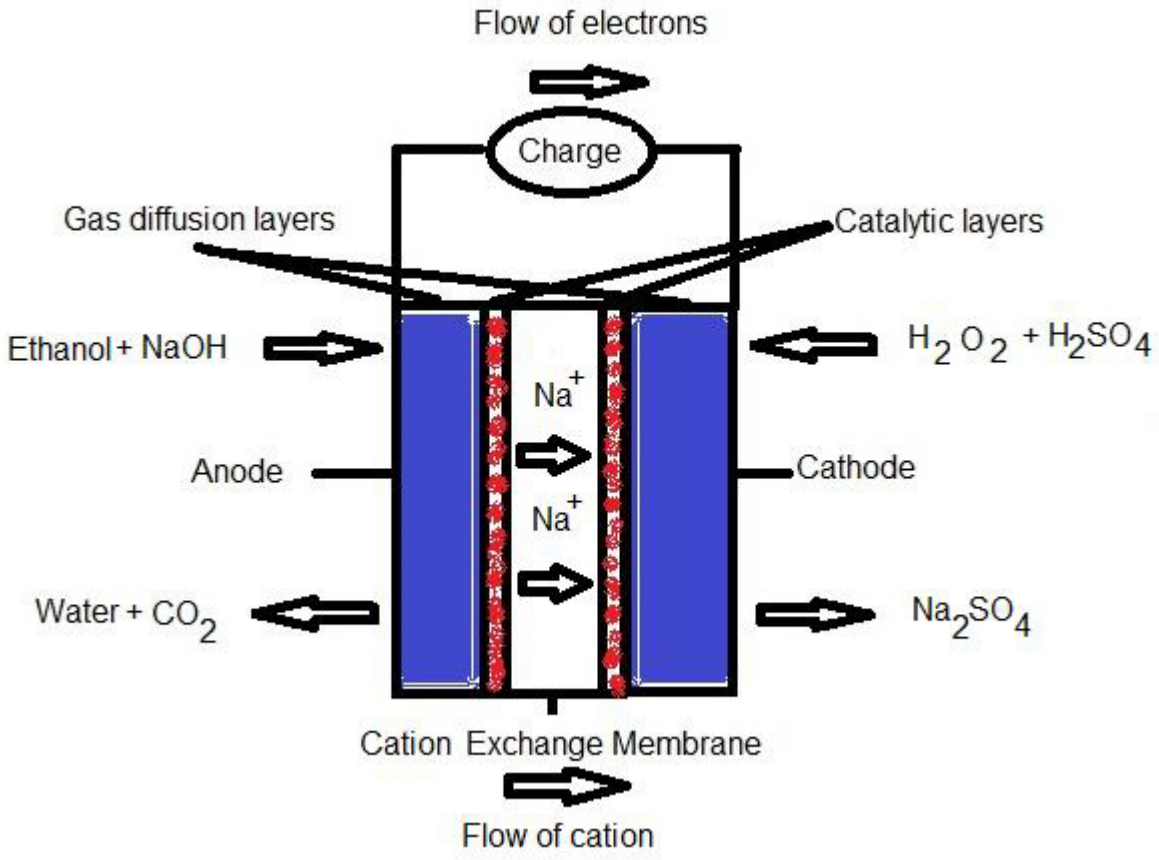

Fig. 6. Alkaline acid direct ethanol fuel cells (AADEFCs)

The resulting power density was higher than 240 mW cm^{-2} at 60 ˚C for conventional DEFCs (An *et al*., 2011). Researchers need to improve these fuel cells further for wider employability. The actual OCV showed 1.60V, which was lower than the theoretical value of 2.52 V. The ethanol crossover membrane reduced cell performance and hydrogen peroxide decomposed in the active site of the electrocatalysts.

2.2 Fuel Cell Theory

The purpose of this topic is to describe and better understand the chemistry and thermodynamics involved in fuel cells. The influences of variables such as temperature, pressure, and gas relate to the performance activity of fuel cells, which are developing in their design to maximize the performance of systems applications. Accordingly, ideal performance can be determined and loss activity can be calculated to describe actual operation.

2.2.1 Gibbs free energy and Nernst potential

The Gibbs free energy change (ΔG) from the electrochemical reaction in the fuel cell operating at constant temperature and pressure is equal the maximum amount of electrical energy produced (W_{el}) (EG&G Technical Services Inc, 2007, Pilatowsky *et al*., 2011).

$$W_{el} = \Delta G = -nFE \quad (21)$$

where n is the number of electrons participating in the reaction, F is Faraday's constant (96,487 $Cmol^{-1}$), and E is the ideal potential of the cell or electromotive force (EMF).

In the hydrogen oxidation reaction, two electrons are transferred (Rayment *et al*., 2003).

$$\text{Maximum Electrical work} = \text{charge X voltage}$$

$$W_{el} = -2FE \quad \text{Joules}$$

when rearranged from Equation 21, it gives:

$$E = -\frac{\Delta G}{2F} \quad (22)$$

where E is the EMF or reversible open circuit voltage for a hydrogen fuel cell.

Gibbs free energy change is also defined as:

$$\Delta G = \Delta H - T\Delta S \quad (23)$$

where ΔH is the enthalpy change, T is the temperature and ΔS is the entropy change. The enthalpy change has less quantity than TΔS equal to the free energy, which demonstrates the unavailable energy resulting from the entropy change in the full cell system.

Reactions in a fuel cell have negative entropy change of heat, such as hydrogen oxidation. On the other hand, direct solid carbon oxidation results in positive entropy change and may extract heat during operation of the system.

For a general reaction,

$$\alpha A + \beta B \quad \rightarrow \quad cC + \delta D \tag{24}$$

the standard state Gibbs free energy change of reaction is given by:

$$\Delta G^0 = cG_C^0 + \delta G_D^0 - \alpha G_A^0 - \beta G_B^0 \tag{25}$$

where G_i^0 is the partial molar Gibbs free energy for species i at temperature T. The heat capacities (C_P) of the i species act as a function of T (298K) and can be given by:

$$C_P = a + bT + cT^2 \tag{26}$$

where a, b, and c are constants values. The specific enthalpy for any species present during the reaction is given by:

$$H_i = H_i^0 + \int_{298}^{T} C_{pi} dT \tag{27}$$

Specific entropy at temperature T and constant pressure is given by:

$$S_i = S_i^0 + \int_{298}^{T} \frac{C_{pi}}{T} dT \tag{28}$$

Then;

$$\Delta H = \sum n_i H_i \Big|_{out} - \sum n_i H_i \Big|_{in} \tag{29}$$

For entropy;

$$\Delta S = \sum niSi \Big|_{out} - \sum niSi \Big|_{in} \tag{30}$$

The Gibbs free energy change can be expressed by:

$$\Delta G = \Delta G^0 + RT \ln \frac{f_C^c f_D^\delta}{f_A^\alpha f_B^\beta} \tag{31}$$

where ΔG^0 is the Gibbs free energy change at standard pressure (1atm), with temperature T and f_i as the fugacity of species i. Equation 21 instead of Equation 30 provides:

$$E = E^0 + \frac{RT}{nF} \ln \frac{f_C^c f_D^\delta}{f_A^\alpha f_B^\beta} \tag{32}$$

For the general form, it gives:

$$E = E^0 + \frac{RT}{nF} \ln \frac{product\ fugacity}{reactant\ fugacity} \tag{33}$$

Equation 33 is the general form of the Nernst equation.

2.2.2 Fuel Cell Efficiencies

Fuel cell efficiency is determined by Gibbs free energy of formation, ΔG_f, and the enthalpy of formation, ΔH_f. The enthalpy of formation is conducted by burning the fuel and commonly mentioned calorific value (Rayment *et al*., 2003). The efficiency of a fuel cell is given by:

$$\frac{electrical\ energy\ produced\ per\ mole\ of\ fuel}{-\Delta H_f} = \frac{\Delta G_f}{\Delta H_f} \quad (34)$$

Therefore, the maximum efficiency for a fuel cell is determined by Equation 35:

$$\text{the maximum efficiency} = \frac{\Delta G_f}{\Delta H_f} x\ 100\% \quad (35)$$

where ΔG_f is Gibbs free energy of formation or the actual energy produced by the reaction and ΔH_f is enthalpy of formation or the ideal energy produced by the reaction.

The maximum efficiency of PEMFC

Anode: $H_2 \rightarrow 2H^+ + 2e^-$ $\Delta G_f = 0$ kJ (36)

Cathode: $1/2O_2 + 2H^+ + 2e^- \rightarrow H_2O$ $\Delta G_f = -237.2$ kJ/mol (37)

$\Delta H_f = -285.8$ kJ (38)

The Gibbs free energy of formation and enthalpy of formation value (Equation 37, 38) substitute into Equation 35 as:

$$\text{the maximum efficiency} = \frac{\Delta G_f}{\Delta H_f} x\ 100\% = \frac{237.2}{285.8} x\ 100 = 83\% \quad (39)$$

The ideal potential of the cell of PEMFC (from Equation 22)

$$E = -\frac{\Delta G}{2F} = \frac{(-237200)}{(2)(96{,}485)} = 1.229 \approx 1.23\ V \quad (40)$$

2.3 Electrochemical reactions

2.3.1 Cyclic Voltammetry (CV)

Qualitative information concerning electrochemical surface of catalysts and corresponding reactions can be obtained using the cyclic voltammetry technique. The redox potential of the active sites is obtained rapidly in inert electrolyte. In this thesis, the initial electrochemical characterisation of catalysts and electrode surface was performed by cyclic voltammetry.

2.3.1.1 Fundamentals of Cyclic Voltammetry

The standard CV experiment uses the three electrode arrangement. These are the reference electrode, the working electrode, and the counter electrode, which are immersed in an unstirred electrolyte solution during cyclic voltammetry. Glassy carbon, platinum, and gold are used as for the working electrode. The potential of the working electrode is measured versus a reference electrode, such as a saturated calomel electrode (SCE), a reversible hydrogen electrode (RHE), or a silver/silver chloride electrode (Ag/AgCl). The counter electrode, as auxiliary electrode,

needs be electrochemically and chemically inert in the used electrolyte, thus relatively inert materials such as platinum, graphite or glassy carbon. The operating potential can be considered as excitation signal, which is applied to the working electrode and the respective current response is detected (Kissinger *et al*., 1983). Typically, potential sweep cycles with a triangular waveform are employed as the excitation signal as shown in Figure 7.

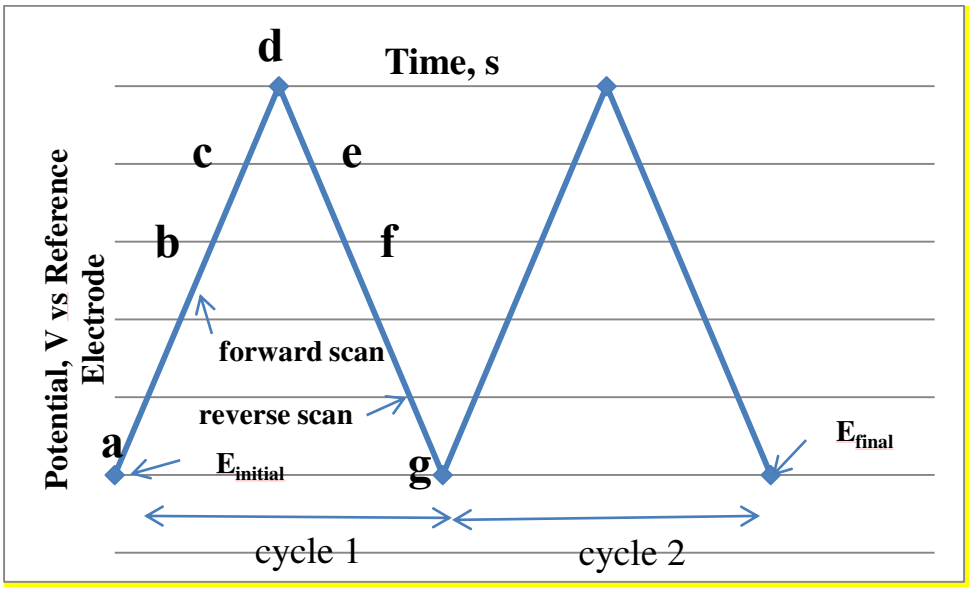

Fig. 7. Typical excitation signal for cyclic voltammetry

The potential cycle starts with a sweep from potential (a) to potential (d) for the forward scan. At potential (d), which is called the switching potential the reverse scan starts and ends at potential (g), where the first potential cycle finished (Fig. 7, 8). Typically, the forward scan is known as anodic sweep, meaning that anodic currents (i.e. positive currents) deriving from oxidation reactions are measured. Whereas the reverse scan is called the cathodic sweep as reducing or negative currents are measured as corresponding response signal (see Fig. 7 and 8).

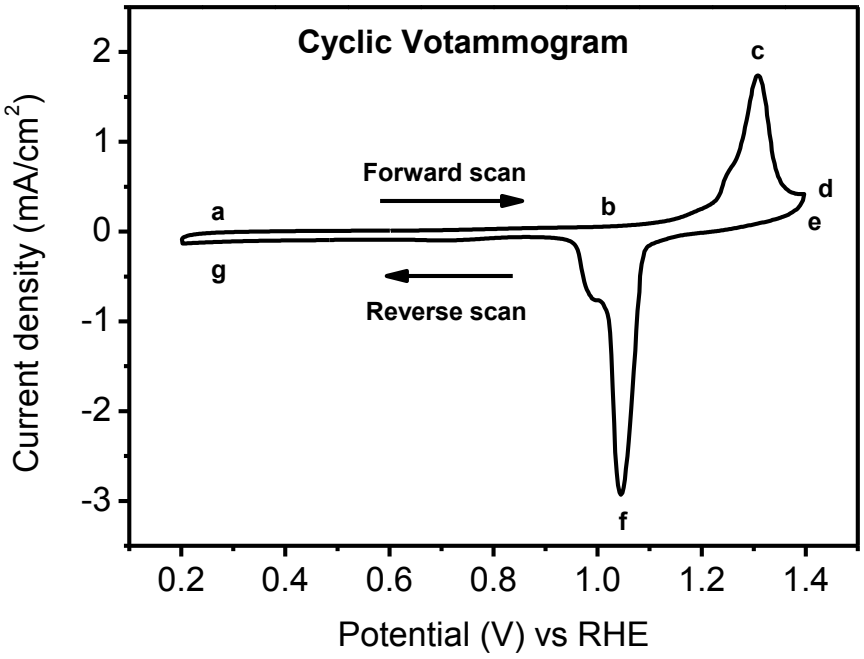

Fig. 8. Cyclic voltammogram of Ag/C in 0.1M KOH at scan rate 10 mVs^{-1}

2.3.2 Oxygen Reduction Reaction (ORR)

Normally in the fuel cells, the ORR reaction on the cathode is usually catalysed by platinum (Pt) - based electrocatalysts. In order to obtain practical ORR activities large quantities of platinum are used due to the sluggish reaction kinetics. However, Pt-based electrocatalysts are rather expensive (Zhang *et al*., 2006). Therefore, novel electrocatalysts, including non-noble electocatalysts, were developed by several researchers. These electrocatalysts include non-noble metals, alloys, metal-organic complexes and platinum alloys.

The reaction mechanism of the ORR is complex and consists of many intermediate steps. The complete reduction of oxygen involves a $4e^-$ transfer and is of course favoured. However, the ORR could also proceed via a $2e^-$ transfer leading to H_2O_2 production. (Yeager, 1986, Bard *et al*., 1980).

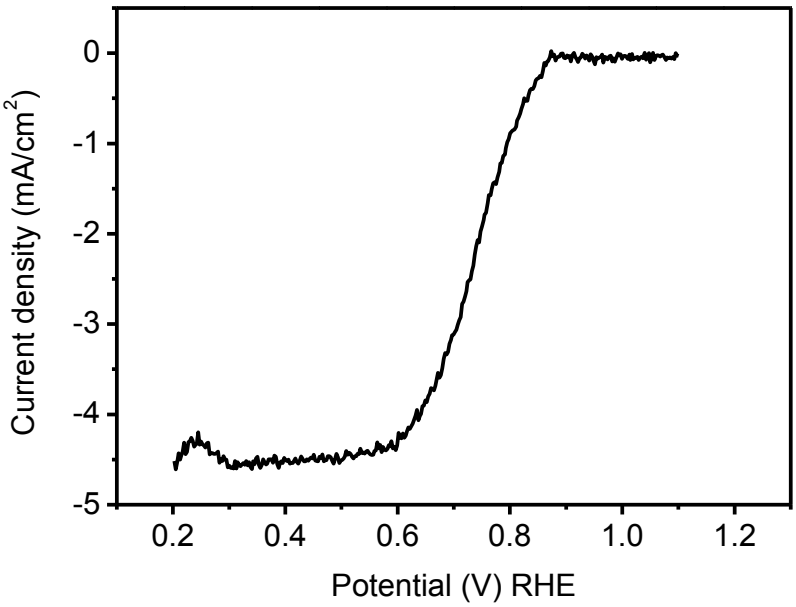

Fig. 9. Linear potential scan curves of Pt/C on a rotating disk electrode (RDE) 0.1 M of KOH in O_2 saturated at 30 °C, with a sweep rate of 10 mV s^{-1} and rotation rate of 1600 rpm

The ORR polarisation curve shows a well-defined diffusion-limiting current at E = 0.20-0.60V, followed by the region under mixed kinetic-diffusion control at 0.70 < E < 0.90 V (Fig. 9) (Garsany *et al*., 2012).

2.3.2.1 ORR on glassy carbon

The reaction mechanism of the ORR was proposed by Yeager as below (Yeager, 1986):

$$O_2 \rightarrow O_{2(ads)} \quad (41)$$

$$O_{2(ads)} + e^- \rightarrow [O_{2(ads)}]^- \quad (42)$$

$$[O_{2(ads)}]^- \rightarrow O_{2(ads)}^- \quad (43)$$

$$O_{2(ads)}^- + H_2O \rightarrow HO_{2(ads)} + OH^- \quad (44)$$

$$HO_{2(ads)} + e^- \rightarrow HO_{2(ads)}^- \quad (45)$$

$$HO_{2(ads)}^- \rightarrow HO_2^- \quad (46)$$

The subscript “ads” refer to adsorbed species on the electrode surface. Two different forms of the superoxide ion on the glassy carbon surface are displayed at the reaction (43). The $[O_{2(ads)}]^-$ in

reaction (43) refer to the inert form of the superoxide ion adsorbed on the inert glassy carbon surface. Reaction (43) is the rate determining step. The rate-determining step is considering on the pH of the electrolyte (Taylor *et al*., 1975, Taylor *et al*., 1975). At pH > 10, reaction (43) is the rate-determining step, whereas at a pH < 10. Reaction (42) is the rate determining step for the ORR. On a glassy carbon electrode surface found $2e^-$ transfer, producing H_2O_2.

2.3.2.2 ORR on Pt electrocatalysts

The ORR on Pt as electrocatalyst is a multi-electron transfer process producing different intermediates products. The main mechanism produces only two products such as H_2O_2 and H_2O (Markovic *et al*., 2002).

$$O_2 \rightarrow O_{2(ads)} \quad (47)$$

$$O_{2(ads)} \xrightarrow{k_1} H_2O \quad (48)$$

$$O_{2(ads)} \xrightarrow{k_2} H_2O_{2(ads)} \quad (49)$$

$$H_2O_{2(ads)} \xrightarrow{k_3} H_2O \quad (50)$$

$$H_2O_{2(ads)} \xrightarrow{k_4} O_{2(ads)} \quad (51)$$

$$H_2O_{2(ads)} \xrightarrow{k_5} H_2O_2 \quad (52)$$

Firstly, oxygen adsorbs on the surface of the Pt electrocatalysts. The adsorbed oxygen on the Pt electrocatalysts can be directly converted into water with following reaction (48) via a $4e^-$ transfer or into the hydrogen peroxide ($H_2O_{2(ads)}$) intermediate via a $2e^-$ transfer as in reaction (49). $H_2O_{2(ads)}$ can be further converted into water according to reaction (50) or be either decomposed as in reaction (51) or desorbed from the Pt electrocatalysts surface into the electrolyte (Reaction (52)).

The ORR mechanism on Pt has also been widely investigated by density function theory (Zhdanov *et al*., 2006, Norskov *et al*., 2004, Shi *et al*., 2006). Two different mechanisms, i.e. the dissociative and the associative mechanism, for ORR on Pt surfaces have been identified.

Dissociative Mechanism:

$$1/2O_2 + Pt_{surface} \rightarrow Pt_{surface}\text{-}O \quad (53)$$

$$Pt_{surface}\text{-}O + H^+ \rightarrow Pt_{surface}\text{-}OH \quad (54)$$

$$Pt_{surface}\text{-}OH + H^+ \rightarrow H_2O + Pt_{surface} \quad (55)$$

where $Pt_{surface}$ is an active site on the Pt surface. In the dissociative mechanism, oxygen is adsorbed on the Pt surface, where the O-O bond broken and forming OH with H^+ on the Pt surface (see Reaction (54)). Finally, this mechanism produces water. H_2O_2 cannot be formed on the Pt surface.

Associative Mechanism (Zhdanov *et al*., 2006, Norskov *et al*., 2004, Shi *et al*., 2006):

$$O_2 + Pt_{surface} \rightarrow Pt_{surface}\text{-}O_2 \quad (56)$$

$$Pt_{surface}\text{-}O_2 + H^+ + e^- \rightarrow Pt_{surface}\text{-}HO_2 \quad (57)$$

$$Pt_{surface}\text{-}HO_2 + H^+ + e^- \rightarrow H_2O + Pt_{surface}\text{-}O \quad (58)$$

$$Pt_{surface}\text{-}O + H^+ + e^- \rightarrow Pt_{surface}\text{-}OH \quad (59)$$

$$Pt_{surface}\text{-}OH + H^+ + e^- \rightarrow H_2O + Pt_{surface} \quad (60)$$

O_2 is adsorbed on the Pt catalyst surface. In the consecutive reaction steps with H^+ the O-O bond may not be broken. Thus the reaction to the final product water proceeds via peroxide and hydroxide intermediates on the Pt surface.

2.3.3 Rotating Disk Electrode (RDE)

The rotating disk electrode (RDE) has been used in order to rapidly screen the activity of various electrocatalysts for the ORR. The experimental set-up of the RDE technique is shown in Figure 10.

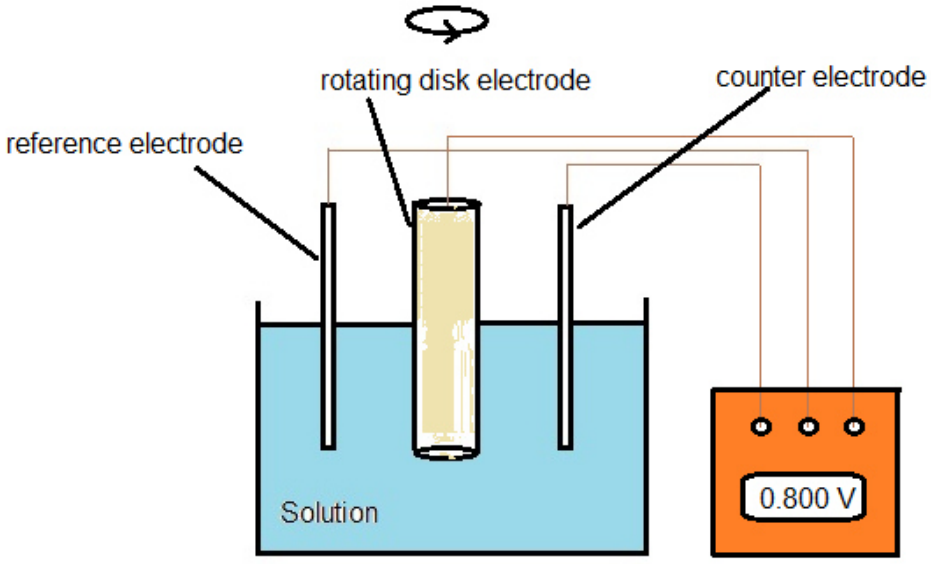

Fig. 10. Components of a rotating disk electrode (RDE)

A standard RDE experiment consists of three electrodes setup as described above including a reference electrode, a working electrode as RDE, and a counter electrode.

The equation used for RDEs is expressed as follows (Bard *et al*., 1980):

$$\frac{1}{i} = \frac{1}{i_k} + \frac{1}{i_l}$$

(Koutecky-Levich Equation) where i is the disk current density, i_l is limiting or Levich current density and i_k is the kinetic current density (A/cm^2).

2.3.4 Levich Equation

The Levich equation is an empirical equation and used to determine the number of electrons from mass transport limited current following the relationship:

$$\left| i_l \right| = 0.620nFAD^{2/3}\omega^{1/2}\upsilon^{-1/6}C^* \qquad (41)$$

where i_l is the limiting or Levich current density (A/cm^2), n is the number of electrons involved in the reaction, F is Faraday's constant, A is the geometric surface area of the electrode (cm^2), D is the diffusion coefficient (cm^2/s), ω is the rotation rate (rad/s), υ is the kinematic viscosity (cm^2/s) and C* is the oxygen concentration in the electrolyte (mol/cm^3).

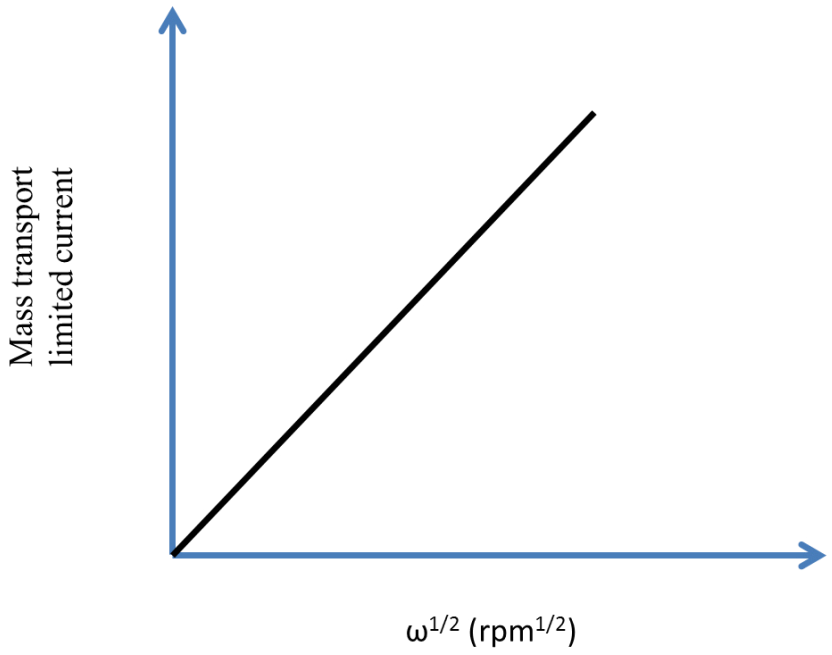

Fig. 11. A Levich plot

The corresponding Levich plot is shown in Figure 11, where the mass transport limited current is plotted versus at different rotation rates of the RDE. If the requirements for mass transport limitation are fulfilled, the regression line is linear and intercepts the vertical axis at zero. From the slope of the regression curve, $0.620nFAD^{2/3}\upsilon^{-1/6}C^*$, the number of transferred electrons can be determined. On the other hand, if the requirements for mass transport limitation are not fulfilled, the regression line displays non-linear behaviour, indicating that the system is under kinetic limitation. In the case, the Levich plot cannot be used to determine the number of electron (n) (Bard *et al*., 1980, Chaparro *et al*. 2010).

2.3.5 Koutecky-Levich Equation

The Koutecky-Levich equation can be used to determine the kinetic current density (i_k) and the heterogeneous rate constant when mass transport is not a factor. The Koutecky-Levich equation is shown below:

$$\frac{1}{i} = \frac{1}{i_k} + \frac{1}{i_l} = \frac{1}{i_k} + \frac{1}{0.62nFAD^{2/3}\gamma^{-1/6}\omega^{1/2}\,C^*} \qquad (42)$$

where i_l is limiting current or Levich current (A/cm^2), i_k is the kinetic current density, n is the number of electrons involved in the reaction, F is Faraday's constant, A is the geometric surface

area of the electrode (cm^2), D is the diffusion coefficient (cm^2/s), ω is the rotation rate (rad/s), υ is the kinematic viscosity (cm^2/s) and C* is the electrolyte concentration (mol/cm^3).

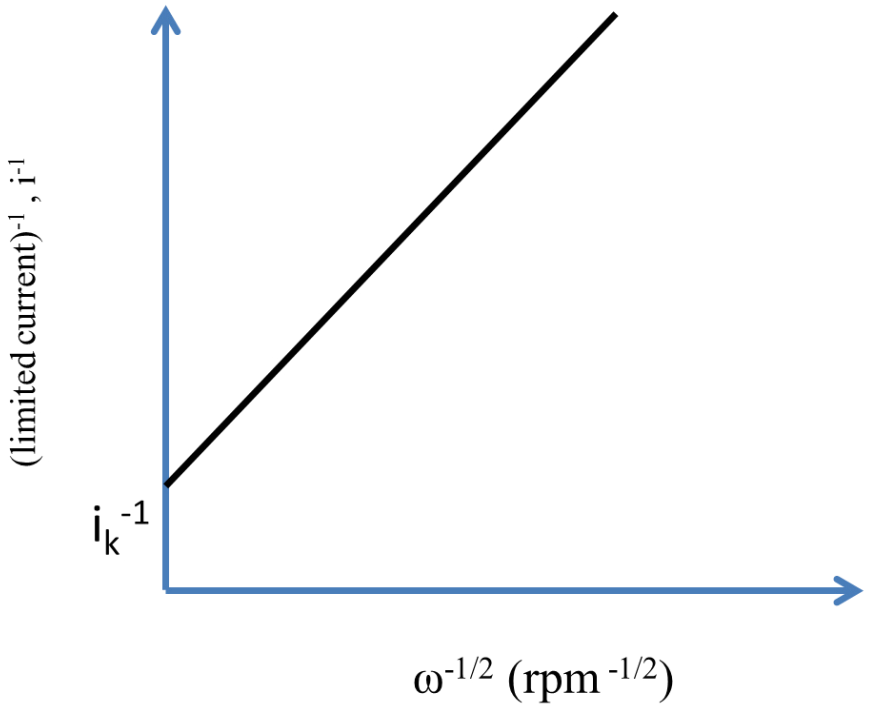

Fig. 12. A Koutecky-Levich plot

The Koutecky-Levich plot enables to determine the kinetic limited current density, i.e. the point where the regression line intercepts the y-axis. From the slope of the regression line it is also possible to determine the number of transferred electrons.

2.4 Morphology of catalysts and their active components

2.4.1 Scanning electron microscopy

A scanning electron microscope (SEM) is used for producing high-resolution images of material morphology and giving information concerning elements in the material. The information of signal is obtained from the interaction between an electron beam and hits the specimen. The scanning electron microscopy technology used a beam of electrons to scan the surface of a sample to generate a three-dimensional image. A variety of signals are generated and collected in related detectors. These signals include (Zhang, 2008):

● secondary electrons (electrons from the sample itself),

● back-scattered electrons (form an electron beam from the filament cathode, which throw off the nuclei of atoms in the specimen),

● X-rays, light and heat.

The secondary electron detector will detect low-energy electrons dislodged from the specimen surface depending on the sample composition. The back-scattered electron detector will detect high-energy electrons reflected by the sample surface and offer on the distribution atomic numbers within a specimen. The initial SEM images obtain information from secondary electrons. An electron beam is created from an electron gun. A tungsten filament cathode is commonly used in thermionic electron gun, which has the lowest vapour pressure compared to other metals, the highest melting point, and most importantly, low cost. Other types of electron filaments consist of a lanthanum hexaboride (LaB_6) cathode. This filament can be used under vacuum atmosphere.

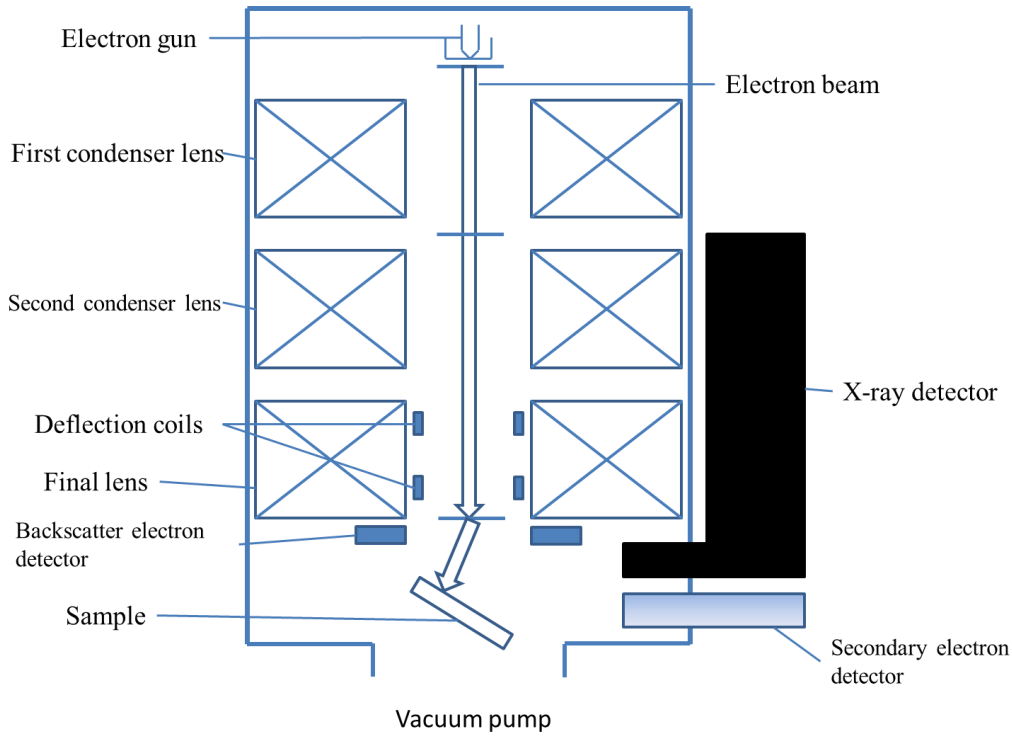

Fig. 13. Components of a scanning electron microscope (SEM)

2.4.2 Transmission electron microscopy (TEM)

The transmission electron microscope (TEM) is the instrument for the electron microscope technique. An electron beam is transmitted through an ultra-thin specimen (50-300 A), which increases magnification and creates higher-resolution. An imaging device such as a CCD camera records received electrons transmitted by scattered specimen atoms. The TEM can display the inside of a sample rather than the surface. Though, the refractive index of the medium does not affect to TEM image when the illumination beam is deflected. Accordingly, the vacuum levels in the lens and column are the same. The electromagnetic properties of the lens are deflective focusing the electron towards the CCD device. Then, It can only be effect on all of the electron paths; meanwhile, the electrons conduct a negative charge. Glass lenses in a light microscope have a homologous function to the plates. In this main point, the electron beam is focused accurately on a CCD camera. On the CCD device transfers data to computer for produce an image. The electron beam is moved across the specimen go to fluorescent screen or CCD camera. The dense atoms in the specimen are subtracted from the image. As a result, they are stopped or deflected. In this way, a black and white image is formed and displayed on the CCD camera. TEM is used for investigating the structure and composition of materials, which can see a few Angstroms (10^{-10} m) of the objects, such as for inorganic material. The possibility exists for obtaining a high-resolution image of biological and medical materials for research (Zhang, 2008).

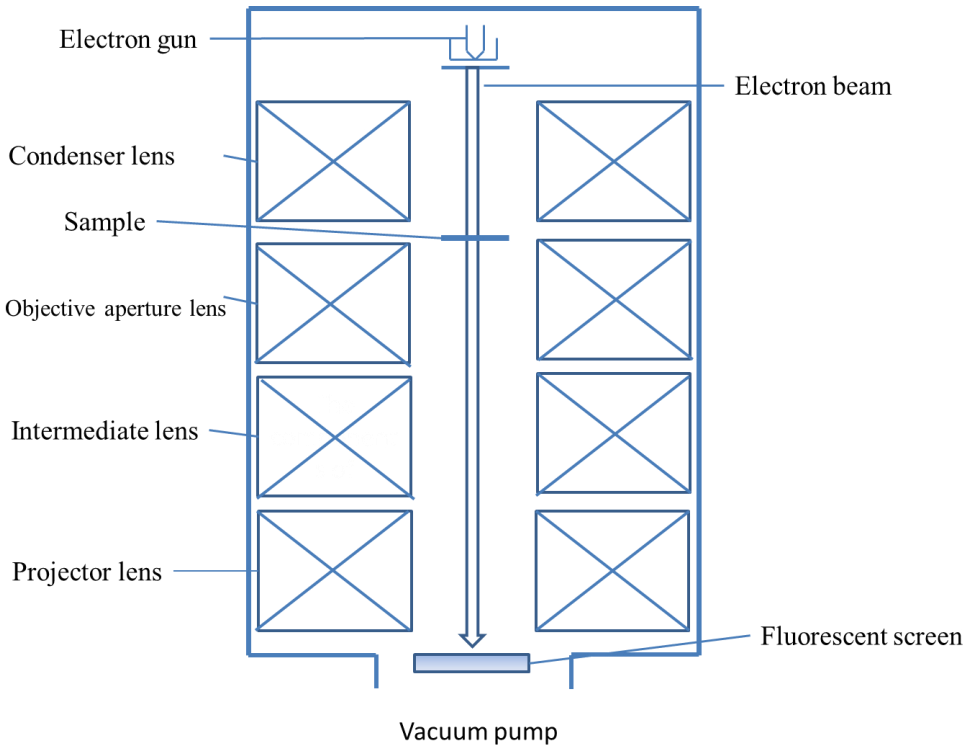

Fig. 14. Components of a transmission electron microscope (TEM)

2.4.3 Energy dispersive X-ray spectroscopy (EDX)

A crystal spectrometer fitted with a diffracting crystal can select the desired wavelength when a specimen is bombarded with high-energy electrons in an electron microscope. X-rays are generated in the process and separated according to their energy levels in a crystal spectrometer fitted with a diffracting crystal. The previous method was called wavelength-dispersive spectroscopy (WDS), while the present is called energy-dispersive spectroscopy (EDS). A solid sample is bombarded with an electron beam. Then, an X-ray spectrum is generated by the movement electrons in atoms. The electrons consist of different energy levels as orbitals. Electrons in the lower orbital hit by X-rays are moved out of the atoms. The created void is replaced by electrons from higher orbital into the lower orbital, which releases the extra energy and hits the detector to obtain chemical analysis. The measured energy levels depend on the gap both orbital levels and are characteristic for each element. Thus EDS can determine the composition of specific elements inside solid materials. In a fundamental source, elements from atomic numbers 4 (Be) to 92 (U) can be detected. On the other hand, light elements such as B, C,

N, O and F (≈ Z < 10) are more difficult to detect due to their low energies, which gives a low yield of X-rays and high absorption in the specimen with in the detector (Heath, 2015).

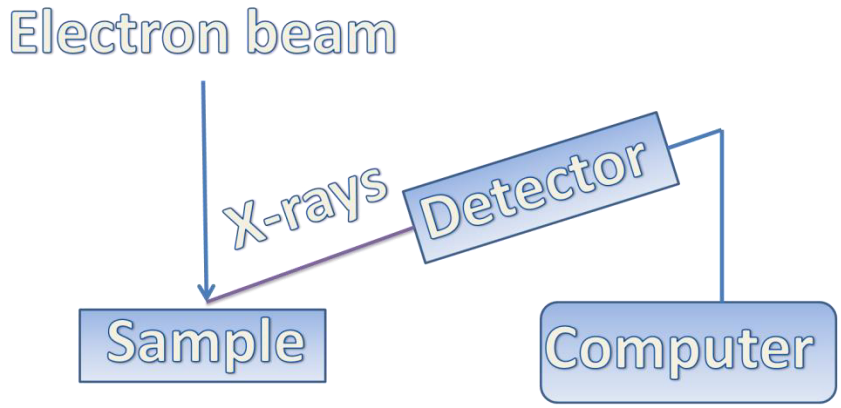

Fig.15. Components of an energy dispersive X-ray spectroscope (EDX)

3. Performance decrease of platinum fuel cell catalyst by coolant leakage (section 1)

3.1 State of the art

Proton exchange membrane fuel cells (PEMFCs) convert hydrogen and oxygen directly into electricity and heat by means of electrochemical reactions. The only by-product generated by these reactions is water. A PEMFC stack is comprised of steel endplates, bipolar plates, a membrane electrode assembly (MEA), a humidifier, and cooling loops. The heat generated by electrochemical reactions or the passing of electrons through the fuel cells is ejected by the system. Liquids can remove heat from a fuel cell better than air cooling because liquid coolant (500-1000 $W.m^{-2}$ K^{-1}) has higher heat transfer coefficients than air cooling (15-30 $W.m^{-2}$ K^{-1}) (Pham, 2014). As such, improved utilisation of fluid coolant has been alluring (Incropera, 1999). Piston engines utilise ethylene glycol (EG) as coolant (boiling point 198 ˚C and freezing point below -40 ˚C) that can likewise be used to cool a fuel cell. However, the performance of PEMFCs may be diminished in the event of coolant leakage into the cell. The coolant can harm the catalyst due to the oxidation of EG on the Pt catalyst sites (Chaiburi *et al*., 2014). CO_2 and CO are produced when the C-C bond is broken by the oxidation of EG with the Pt electrocatalyst (Wieland *et al*., 1996). Carbon monoxide (CO) is a well-known catalyst poison in fuel cells that is strongly adsorbed on Pt and blocks the active sites of the catalyst, thus causing a significant activity decrease (Cheng *et al*., 2007). Subsequently, fuel cell performance is reduced. Additionally, CO obstructs the desired oxidation of hydrogen. Nonetheless, there have been only few studies that examine the maximum quantity of coolant, such as EG, that is acceptable during leakage events without influencing the performance of PEMFCs. Garsany *et al*. observed that coolants such as glycol/water and glycol/water/surfactant mixtures lead to a loss of Pt electrochemical surface area (ECSA). The surfactant was ethoxylated nonylphenol. After 20 cycles using a standard cyclic voltammetry (CV) procedure for cycling between 0.05 V to 1.20 V in N_2-purged 0.10 M $HClO_4$ at a scan rate of 50 mV s^{-1}, the poisoned Pt/C on working electrodes were inspected again. The Pt recovered completely in a clean electrolyte after being contaminated prior (Garsany *et al.*, 2012).

3.2 Goal of Section 1

In this section studies on coolants such as glycol/water and glycol/water/Triton-X are conducted by means of ex-situ CV and ORR method. Triton-X ($C_{14}H_{22}O(C_2H_4O)_n$) is a non-ionic surfactant which has a hydrophilic polyethylene oxide group (on average it has 9.5 ethylene oxide units) and a lipophilic or hydrophobic group as an aromatic hydrocarbon (Chauhan *et al.*, 2011). Triton-X ($C_{14}H_{22}O(C_2H_4O)_n$) is a non-ionic surfactant which has a hydrophilic polyethylene oxide group (on average it has 9.5 ethylene oxide units) and a lipophilic or hydrophobic group as an aromatic hydrocarbon (Chauhan *et al.*, 2011).

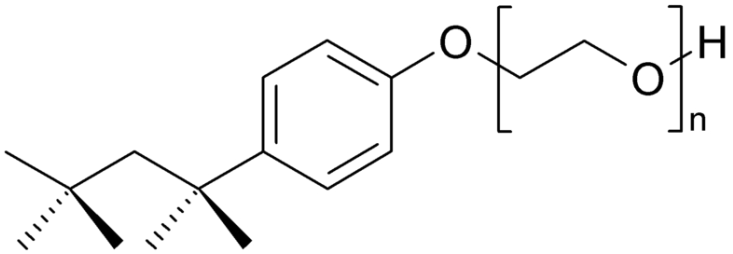

Fig. 1. Triton-X ($C_{14}H_{22}O(C_2H_4O)_n$) (Ethoxylate Octylphenol).

The requirements of the liquid coolant for fuel cells must be a high flash point, high atmospheric boiling point, inflammable, economical, and with a freezing point less than -40 ˚C. Generally, ethylene glycol (EG) is used as a coolant in piston engines (bp. 198 ºC) and it can also be used to cool a fuel cell. For the Pt ECSA, comparisons are given for the Pt ECSA between initial CV and CV after contamination, and then the loss of Pt electrochemical surface area (ECSA) is calculated.

3.3 Experimental

3.3.1 Physical characterization methods

A scanning electron microscopy (SEM) was used to determine the morphology of 30 wt. % Pt/C commercial catalysts (E-Tek). In addition, an energy dispersive X-ray spectroscopy (EDX) was used to analyse the element compositions of Pt/C catalysts.

3.3.2 Coolant materials

The coolant was made from ethylene glycol, ultra-pure water (18 mΩ-cm, Barnstead Nanopure) and Triton-X. The coolant formulation description is listed in Table 1.

Table 1. Selected coolants for fuel cells.

Coolant Number	Description	Ratio
Coolant no.1	Ethylene Glycol / water	1:1
Coolant no.2	Ethylene Glycol / 0.0077 M of Triton-X	1:1
Coolant no.3	Ethylene Glycol / 0.0231 M of Triton-X	1:1
Coolant no.4	Ethylene Glycol / 0.0386 M of Triton-X	1:1
Coolant no.5	Ethylene Glycol / 0.0541 M of Triton-X	1:1

3.3.3 Electrochemical measurements

A standard three-electrode set-up at 303 K was employed to conduct all electrochemical measuring techniques. The 0.10 M H_2SO_4 working electrolyte was set up from ultra-pure water (18 MΩ-cm, Barnstead Nanopure). The reference electrode was a reversible hydrogen electrode (RHE) and a platinum electrode was utilized as the counter electrode. The working electrode was glassy carbon with a ∅ equal to 5 mm and the respective surface area of 0.196 cm^2, on which a commercial 30 wt % Pt on Vulcan carbon XC-72, Pt/C (E-Tek) was deposited. The working electrode Pt- loading was 28 $\mu g_{Pt}\ cm^{-2}$. Ultra high purity nitrogen (N_2) was used to render the electrolyte inert. After measuring the CV and ORR in different electrolytes (i.e. with and without coolant) and the loss of Pt ECSA was calculated (Garsany *et al*., 2012, Beak *et al*., 2010, Bae *et al*., 2012).

$$ECSA_{Pt,cat}(m^2 g_{Pt}^{-1}) = \frac{[Q_{H-adsorption}\,(C)]}{[210\mu C cm_{Pt}^{-2} L_{Pt}(mg_{Pt}cm^{-2})Ag(cm^2)}X10^5 \quad (1)$$

where ECSA is the Pt ECSA ($m^2 g_{Pt}^{-1}$) obtained via calculation (Fig. 2) and Q_H = 210 μCcm^{-2}. L_{Pt} ($mg_{Pt}cm^{-2}$) is Pt loading on the surface of the working electrode and A_g (cm^{-2}) is the geometric surface area of the glassy carbon working electrode (Garsany *et al.*, 2012). The loss of Pt ECSA due to contamination by the coolant is calculated as follows:

$$ECSA_{loss}(\%) = \frac{(ECSA_{initial} - ECSA_{final})}{ECSA_{initial}} \text{x} 100 \quad (2)$$

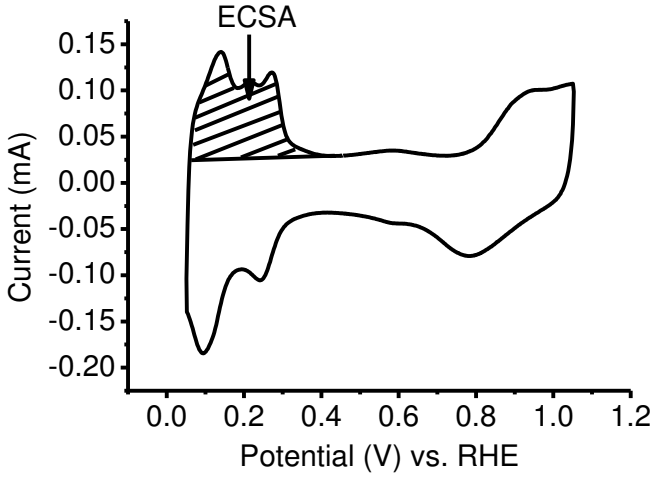

Fig. 2. Pt electrochemical surface area (ECSA)

The kinetic current i_k can be calculate by equation 3, where i_o is the observed current at potential 0.9 V and i_d is the limiting current that can be directly obtained from the ORR curve

$$i_k = \frac{(i_d x i_o)}{(i_d - i_o)} \quad (3)$$

The MA of the catalyst is therefore calculated by equation 4,

$$MA = \frac{i_k}{L_{Pt}} \quad (4)$$

where MA (mA/ μg_{Pt}) is the mass activity of the catalyst, L_{Pt} (mg_{Pt} cm^{-2}) is Pt loading on the surface of the working electrode.

The experimental procedures of the CV at 303K are shown in Table 2.

Table 2. Cyclicvoltammetry (CV) at 303K

Procedure	Cell Number	Potential range (V) vs. RHE	Cycles	Scan rate ($mV\ s^{-1}$)	Purge
Cleaning	Cell Number 1	0.05-1.255	250	500	N_2

Base CV	Cell Number 1	0.05-1.055	3	20	N_2
Contamination	**Cell Number 2**	0.05-1.055	20	20	N_2
After Contamination	Cell Number 1	0.05-1.055	20	20	N_2
Cleaning	Cell Number 1	0.05-1.255	20	50	N_2
Extended CV	Cell Number 1	0.05-1.055	3	20	N_2

Note: **Cell Number 1** is 0.10 M H_2SO_4

Cell Number 2 is 0.10 M H_2SO_4 + 1 ml coolant

The experimental procedures of the ORR at 303K are shown in Table 3.

Table 3. Oxygen reduction reaction (ORR) at 303K

Procedure	Cell Number	Potential range (V) vs. RHE	Cycles	Scan rate ($mV\ s^{-1}$)	Purge
Cleaning	Cell Number 1	0.05-1.255	250	500	N_2
Base ORR in N_2	Cell Number 1	1.03-0.05	3	20	N_2
Base ORR in O_2	Cell Number 1	1.03-0.05	3	20	O_2
Contamination	**Cell Number 2**	1.03-0.05	3	20	O_2

After Contamination	Cell Number 1	1.03-0.05	20	20	O_2
Base ORR in N_2	Cell Number 1	1.03-0.05	3	20	N_2
Cleaning	Cell Number 1	0.05-1.255	20	50	N_2
Base ORR in N_2	Cell Number 1	1.03-0.05	3	20	N_2
Extended ORR	Cell Number 1	1.03-0.05	3	20	O_2

Note: **Cell Number 1** is 0.10 M H_2SO_4

Cell Number 2 is 0.10 M H_2SO_4 + 1 ml coolant

3.4 Results and Discussions

3.4.1 Physical characterisation

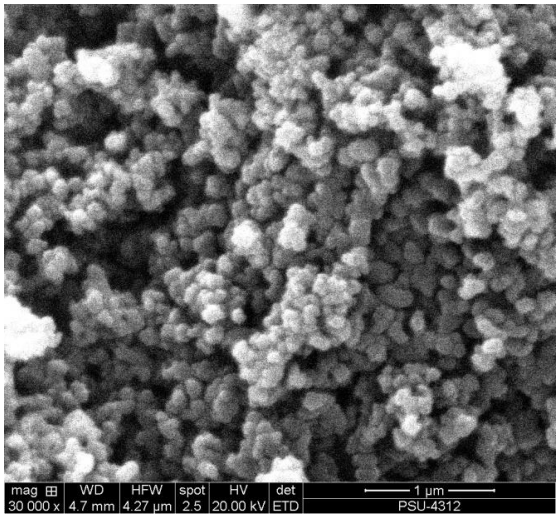

Fig. 3. Typical SEM for a commercial 30% Pt/C (E-Tek) (magnification is 30000) (Chaiburi *et al*., 2014).

According to Fig. 3, the morphology of a commercial 30% Pt/C catalyst sample before contamination with coolant shows the spherical powder aggregated structure.

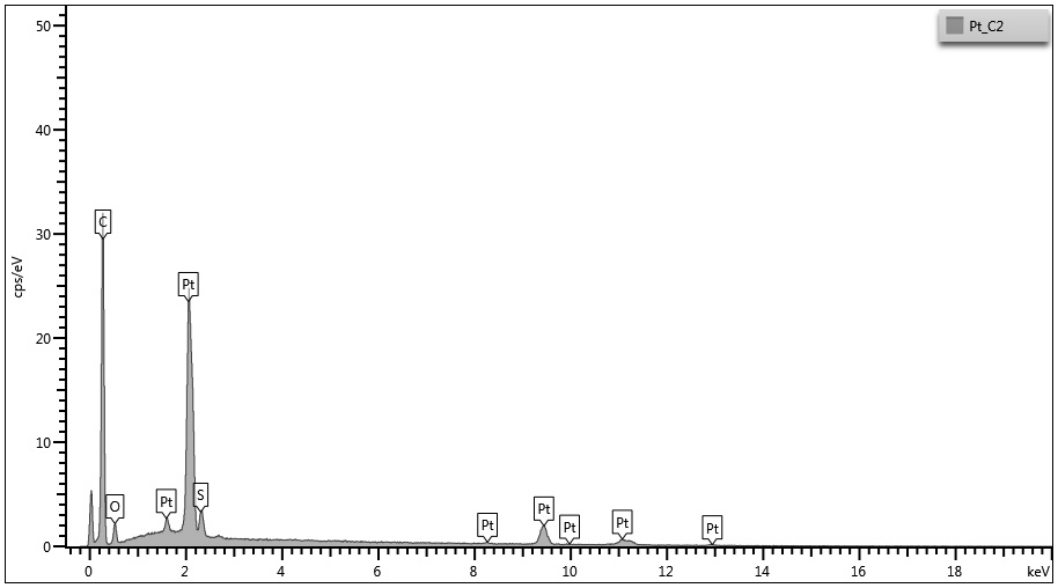

Fig. 4. Typical EDX for a commercial 30% Pt/C (E-Tek) (Chaiburi *et al*., 2014).

According to Fig. 4, the composition of commercial, 30% Pt/C catalyst before contamination illustrates an average of the elements at 63.80% of C, 4.65% of O, 1.11% of S and 30.44% of Pt.

3.4.2 Effect of ethylene glycol-based coolant on CV characteristics

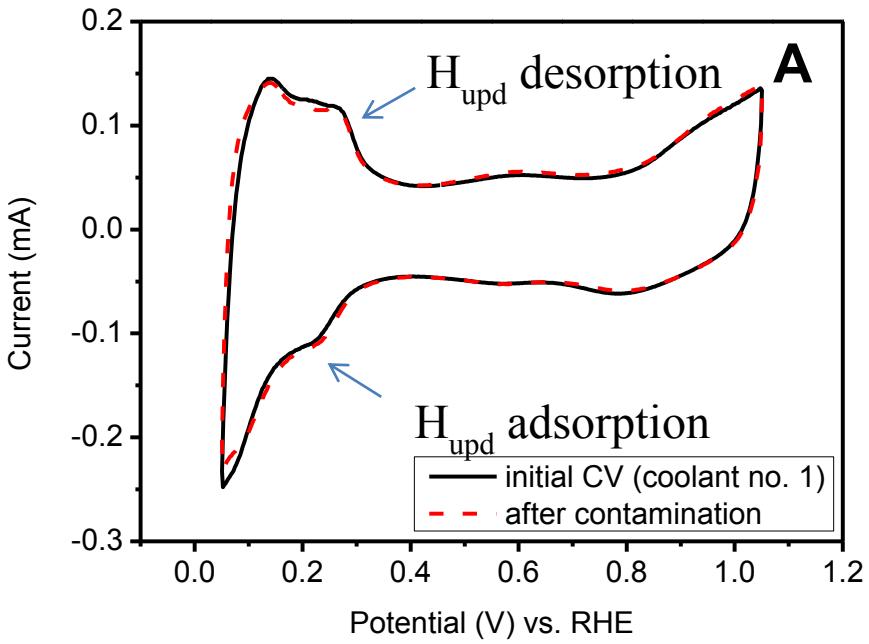

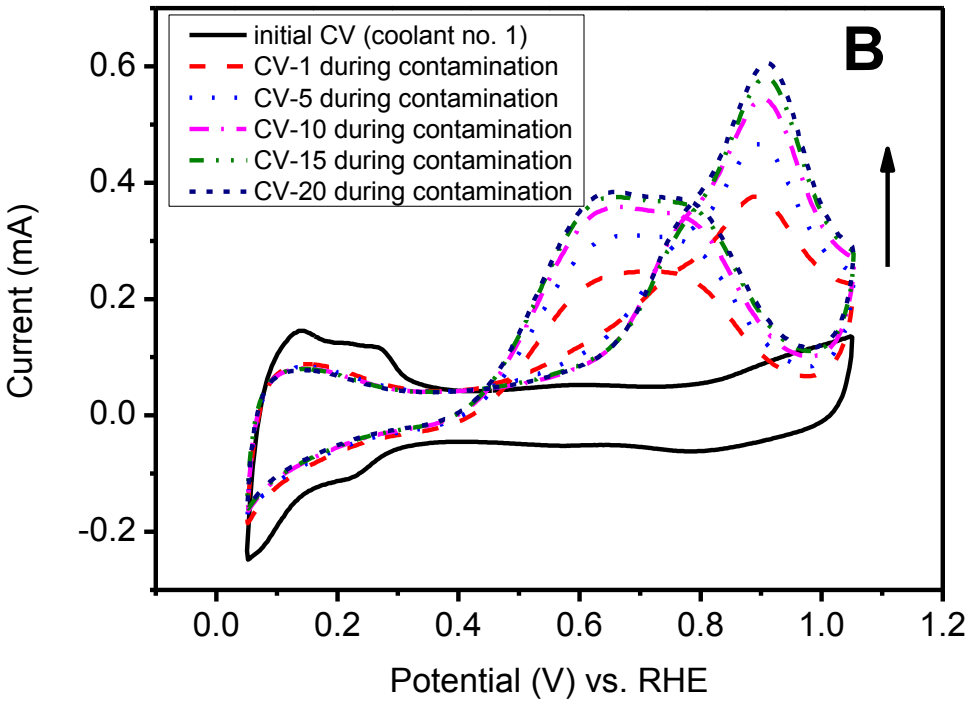

Fig. 5. **A)** Comparison of initial cyclic voltammogram of Pt/C and after contamination with coolant no. 1 in N_2 purged 0.10 M H_2SO_4 electrolyte. **B)** Comparison of initial cyclic voltammogram of Pt/C and cyclic voltammogram of Pt/C (during contamination with coolant no. 1) in N_2 purged 0.10 M H_2SO_4 electrolyte (CV-1 as 1 cycle, CV-5 as 5 cycles, CV-10 as 10 cycles, CV-15 as 15 cycles, CV-20 as 20 cycles).

The loss of Pt ECSA during contamination was 46.98%. On the other hand, the loss of Pt ECSA after contamination was reduced to 3.63% (see Table 3).

A s the CV cycle increases, the anodic current peaks increase slowly cycle by cycle during contamination. As seen from figure 5B, an oxidation peak around 0.9 V is observed in the anodic scan region. At the lower potentials, EG adsorbs on the electrode surface and when the potential reaches 0.4-0.9 V, the current increases due to the electrooxidation of ethylene glycol (Fig. 5B). Vaithilingam Selvaraj *et. al.* suggested a probable mechanism of the EG electrooxidation following steps 1 until 8 (Selvaraj *et al.,* 2008).

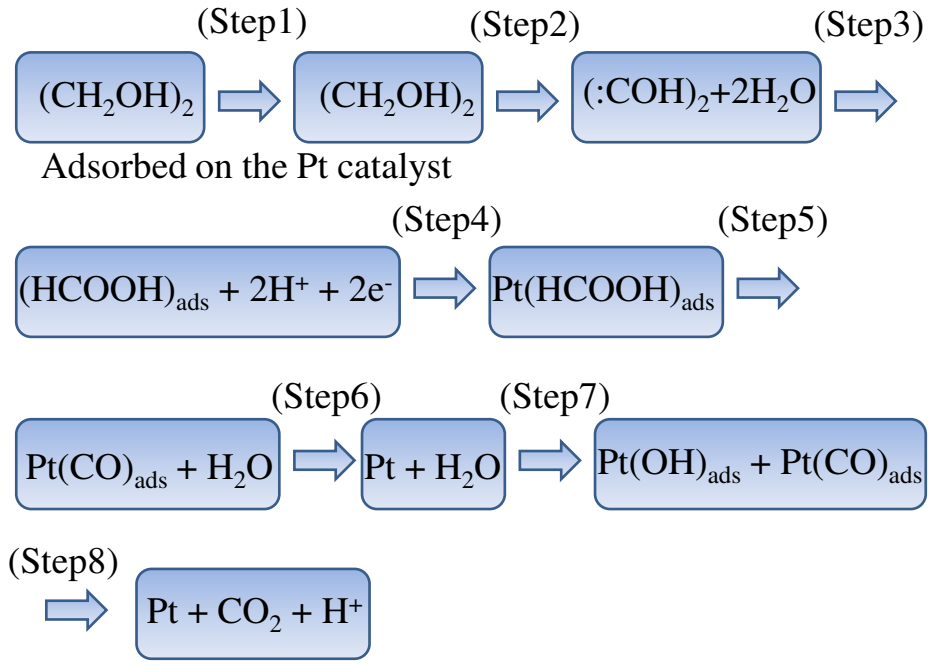

Fig. 6. Mechanism of ethylene glycol electrooxidation

First, EG is adsorbed on the Pt catalyst (Step 1). Then, the oxidation of the EG gives off formic acid as one of the major products (Step 2). Next, the reaction can cause the rearrangement of formic acid into an intermediate $(CO)_{ads}$ (Step 5) on the active sites of Pt. The mechanism possibly removes $(CO)_{ads}$ via an oxidation reaction to CO_2 by reacting with OH_{ads}. Thus, the dissociation of water molecules happens on Pt catalyst surfaces (Steps 7 and 8) (Selvaraj *et al.,* 2008, Jung *et al*., 2013). The water activation process on the active sites of Pt occurs at a higher potential and hence also CO oxidation occurs at potentials of around 0.5 to 0.9 V. Accordingly, the higher potential shows CO oxidation on Pt surfaces. Since the amount of CO species and the EG molecules (Step 1) are adsorbed on Pt catalyst, for a long time the CO species take over on active catalyst sites and reduce Pt ECSA. At a potential of 0.9 V, the mechanism of EG electrooxidation depends on the amount of CO oxidation via the active sites of Pt on the electrode surface (Selvaraj *et al.,* 2008).

Table 4. The loss of ECSA.

	Coolant no.1	Coolant no.2	Coolant no.3	Coolant no.4	Coolant no.5
Origin ECSA	346.76 cm^2/mg_{Pt}	318.31 cm^2/mg_{Pt}	277.32 cm^2/mg_{Pt}	211.84 cm^2/mg_{Pt}	279.55 cm^2/mg_{Pt}
ECSA-loss (during contamination)	46.98%	46.39%	42.18%	37.74%	38.77%
ECSA-loss (after contamination)	3.63%	1.13%	0.53%	0.02%	6.46%

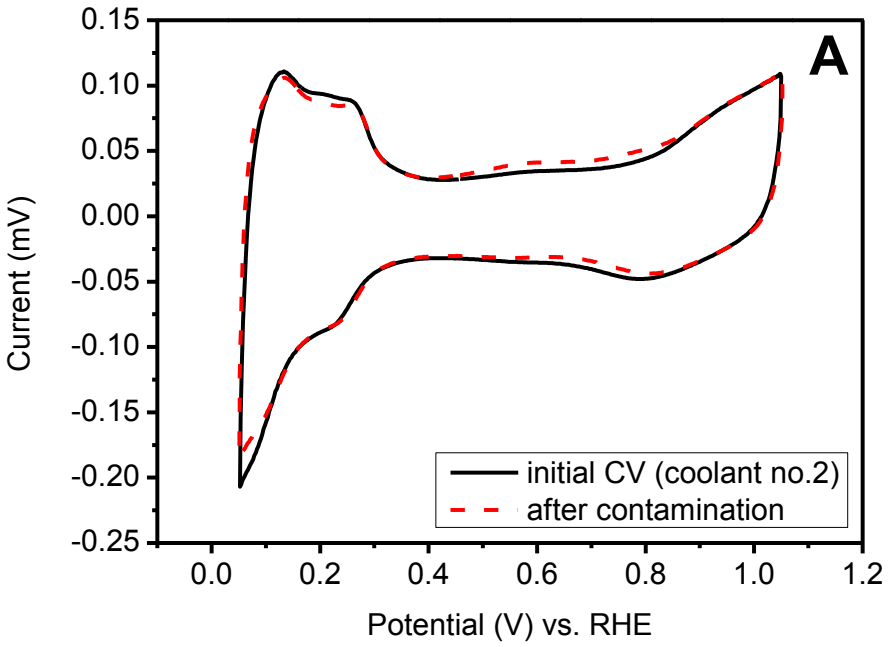

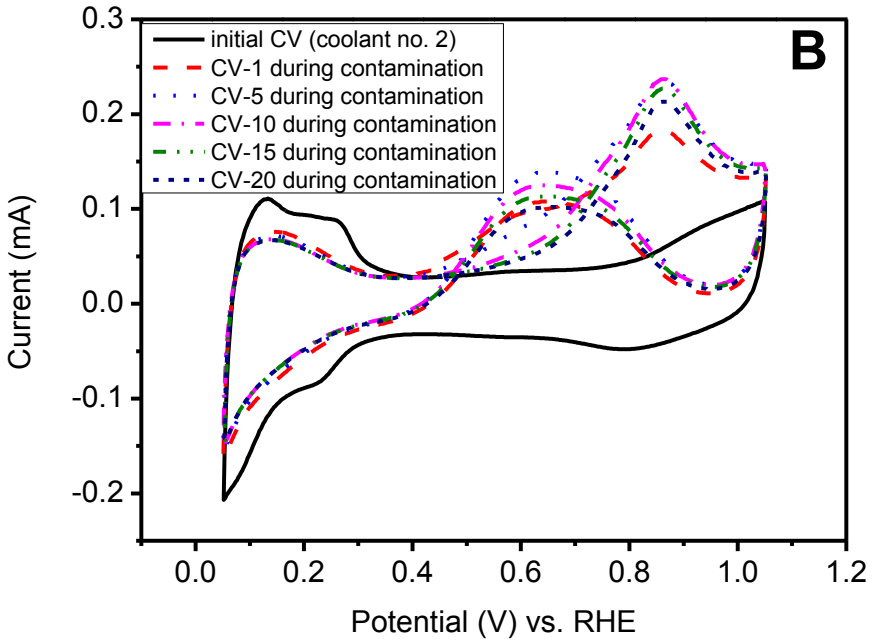

Fig. 7. **A)** Comparison of initial cyclic voltammogram of Pt/C and after contamination with coolant no. 2 in N_2 purged 0.10 M H_2SO_4 electrolyte. **B)** Comparison of initial cyclic voltammogram of Pt/C and cyclic voltammogram of Pt/C (during contamination with coolant no. 2) in N_2 purged 0.10 M H_2SO_4 electrolyte (CV-1 as 1 cycle, CV-5 as 5 cycles, CV-10 as 10 cycles, CV-15 as 15 cycles, CV-20 as 20 cycles).

The loss of Pt ECSA during contamination with initial CV demonstrates 46.39%. Furthermore the loss of Pt ECSA after contamination with initial CV illustrates 1.13% (see Table 3). The CV cycle increases until the 5^{th} cycle, then the CV cycle decreases cycle by cycle (Fig. 7B). Triton-X may reduce the amount of coolant that adsorbs onto the Pt surface.

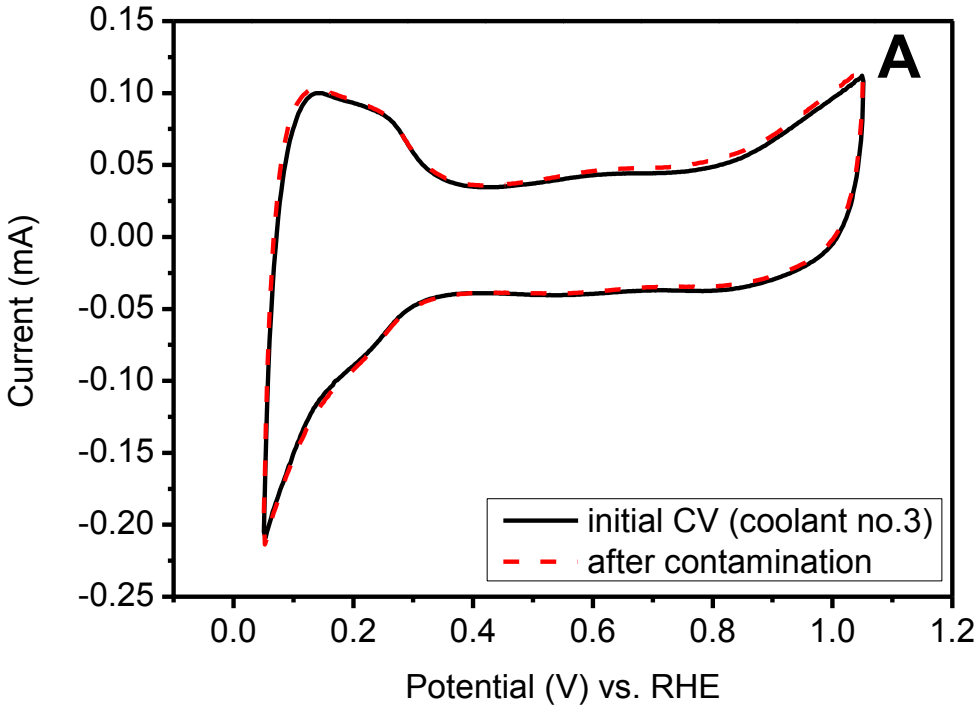
A
Current (mA)
Potential (V) vs. RHE
initial CV (coolant no.3)
after contamination
0.15
0.10
0.05
0.00
-0.05
-0.10
-0.15
-0.20
-0.25
0.0
0.2
0.4
0.6
0.8
1.0
1.2

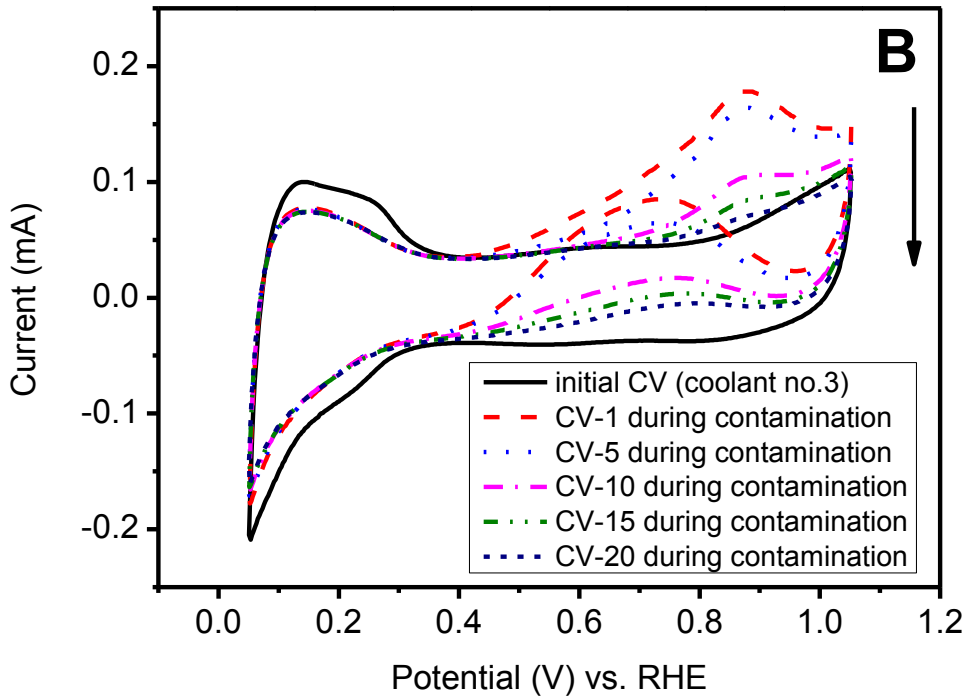
B
Current (mA)
Potential (V) vs. RHE
initial CV (coolant no.3)
CV-1 during contamination
CV-5 during contamination
CV-10 during contamination
CV-15 during contamination
CV-20 during contamination
0.2
0.1
0.0
-0.1
-0.2
0.0
0.2
0.4
0.6
0.8
1.0
1.2

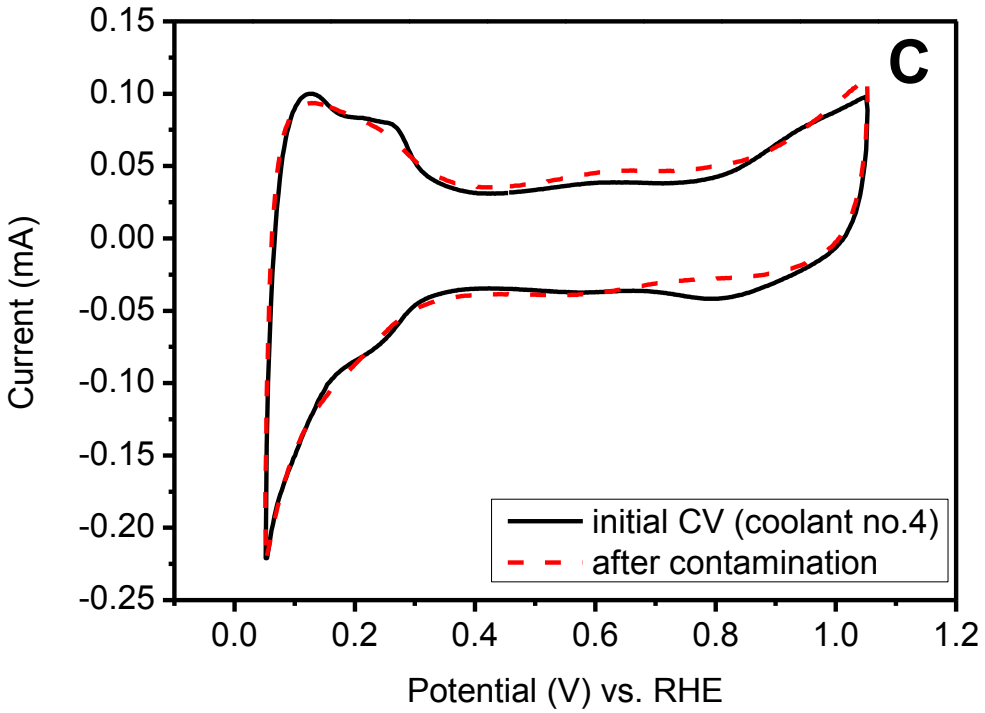
C
Current (mA)
Potential (V) vs. RHE
initial CV (coolant no.4)
after contamination
0.15
0.10
0.05
0.00
-0.05
-0.10
-0.15
-0.20
-0.25
0.0
0.2
0.4
0.6
0.8
1.0
1.2

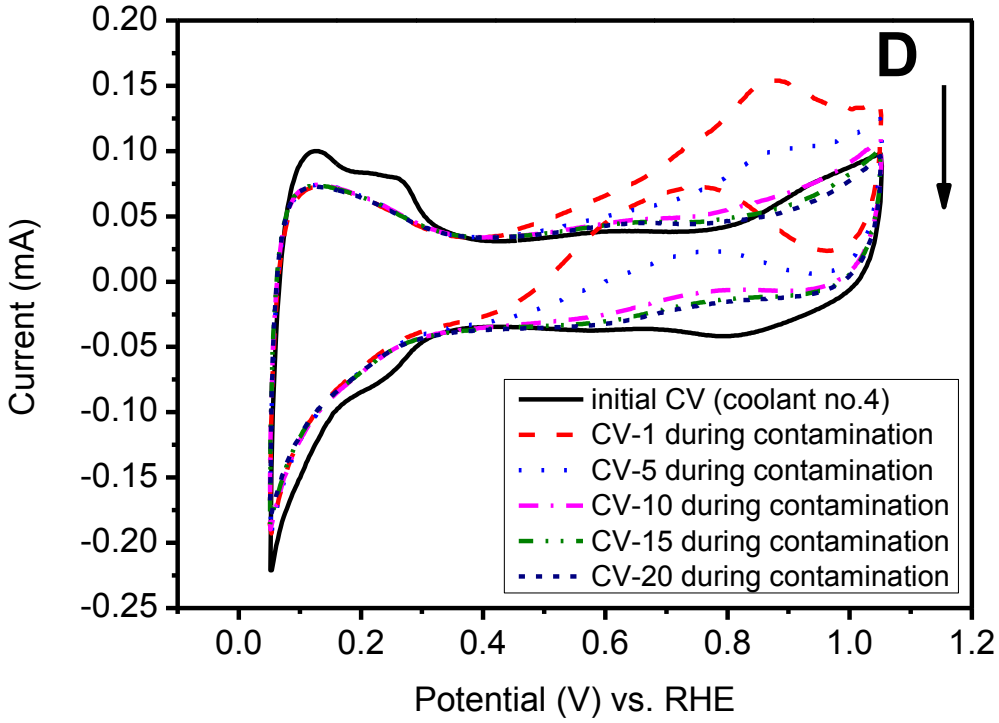
D
Current (mA)
Potential (V) vs. RHE
initial CV (coolant no.4)
CV-1 during contamination
CV-5 during contamination
CV-10 during contamination
CV-15 during contamination
CV-20 during contamination
0.20
0.15
0.10
0.05
0.00
-0.05
-0.10
-0.15
-0.20
-0.25
0.0
0.2
0.4
0.6
0.8
1.0
1.2

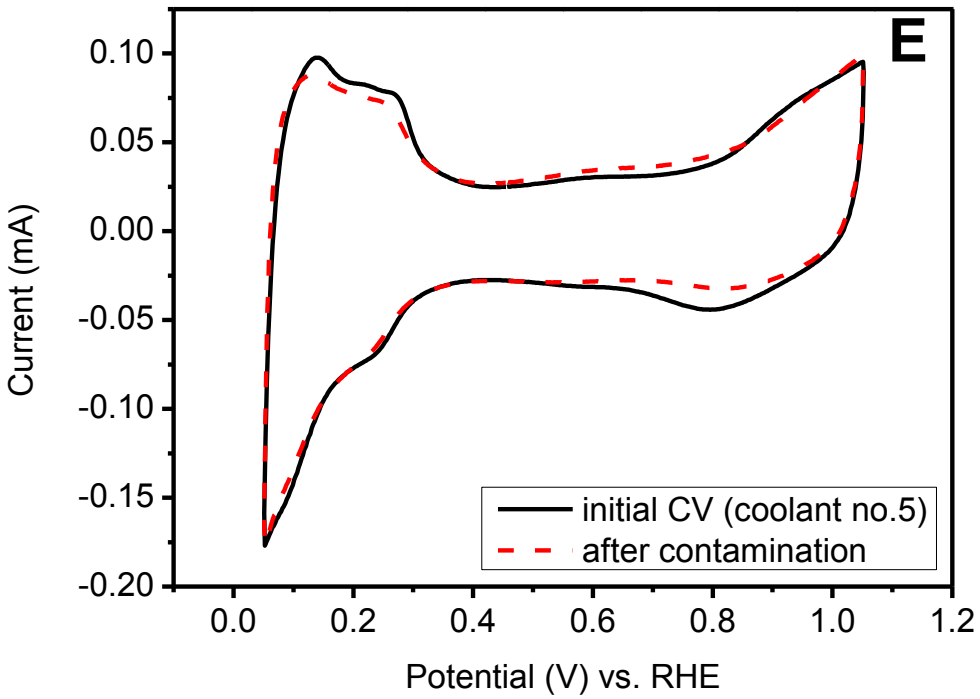
E
0.10
0.05
0.00
-0.05
-0.10
-0.15
-0.20
Current (mA)
0.0
0.2
0.4
0.6
0.8
1.0
1.2
Potential (V) vs. RHE
initial CV (coolant no.5)
after contamination

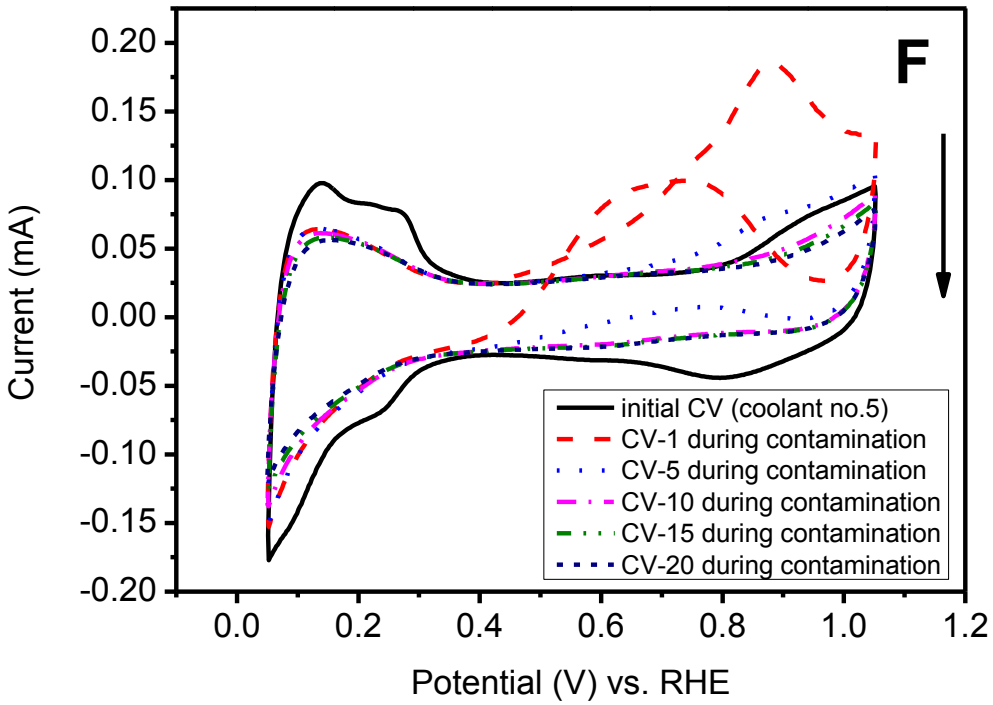
F
0.20
0.15
0.10
0.05
0.00
-0.05
-0.10
-0.15
-0.20
Current (mA)
0.0
0.2
0.4
0.6
0.8
1.0
1.2
Potential (V) vs. RHE
initial CV (coolant no.5)
CV-1 during contamination
CV-5 during contamination
CV-10 during contamination
CV-15 during contamination
CV-20 during contamination

Fig. 8. **A)** Comparison of initial cyclic voltammogram of Pt/C and after contamination with coolant no. 3. **B)** Comparison of initial cyclic voltammogram of Pt/C and cyclic voltammogram of Pt/C (during contamination with coolant no. 3). **C)** Comparison of initial cyclic voltammogram of Pt/C and after contamination with coolant no. 4. **D)** Comparison of initial cyclic voltammogram of Pt/C and cyclic voltammogram of Pt/C (during contamination with coolant no. 4). **E)** Comparison of initial cyclic voltammogram of Pt/C and after contamination with coolant no. 5 in N_2 purged 0.10 M H_2SO_4 electrolyte. **F)** Comparison of initial cyclic voltammogram of Pt/C and cyclic voltammogram of Pt/C (during contamination with coolant no. 5) in N_2 purged 0.10 M H_2SO_4 electrolyte (CV-1 as 1 cycle, CV-5 as 5 cycles, CV-10 as 10 cycles, CV-15 as 15 cycles, CV-20 as 20 cycles).

The loss of Pt ECSA during contamination with coolant no. 3, no. 4 and no. 5 was 42.18%, 37.74% and 38.77%, respectively. The loss of Pt ECSA after contamination however was only 0.53%, 0.02% and 6.46%, respectively (see Table 4). Comparison of Fig. 8B, 8D and 8F. As the CV cycle increases, the anodic current peak decreases cycle by cycle (Fig. 8B, 8D, 8F). Further, the Triton-X, non-ionic surfactant, may inhibit the EG oxidation during contamination with the coolant.

The alkyl group, isooctyl chain, (Fig. 1) of the non-ionic surfactant could adsorb onto the carbon support material of the catalysts and the benzene ring could react to the carbon surface support material via π-π stacking (Bin *et al*., 2009, Zhang *et al*., 2013). Garsany *et al.* studied the observed EG oxidation peak around 0.7 - 0.9 V in the anodic scan region. The current increases due to the electrooxidation of ethylene glycol. At the lower potentials, EG adsorbs on the electrode surface and when the potential reaches 0.4-0.9 V.The ethoxylated nonylphenol, non-ionic surfactant, might not inhibit the mechanism of EG electrooxidation during contamination with 1 ml of coolant (Garsany *et al.*, 2012). With increasing amounts of Triton-X in the coolant mixture (see coolant no.5), the surfactant might start inhibiting the activity of the Pt electrocatalyst by encapsulation of the Pt active sites, resulting in a higher loss of Pt ECSA (see Table 4). As shown in Fig. 5A and Table 4, the loss of Pt ECSA after contamination with coolant (surfactant-free) was 3.63% due to adsorption of EG electrooxidation products (such as CO) that poison the Pt electrocatalyst active sites. In contrast, as demonstrated in Fig. 7A, 8A and 8C and Table 4, the loss of Pt ECSA after contamination with surfactant containing coolant mixtures

decreases with increasing concentration of Triton-X. This insinuates that Triton-X might inhibit the adsorption of EG and its electrooxidation products, thus preventing the blockage of the active catalyst sites. Therefore, the cyclic voltammograms show full recovery of Pt/C electrocatalyst after contamination and reduced activity towards EG electrooxidation (Fig. 8B, 8D, 8F). However, at some point the concentration of the surfactant reaches a critical level and starts to encapsulate the Pt catalysts, reducing the number of available active sites (see coolant no. 5 and Table 4).

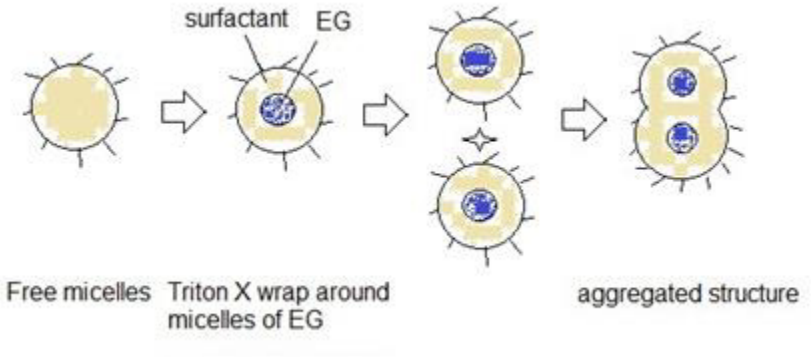

Fig. 9. Micelles of Triton-X wrap around EG (Chaiburi *et al*., 2014).

As can be seen in Fig. 8B, 8D, and 8F, the anodic EG oxidation currents lessen cycle by cycle and finally diminish. According to Fig. 9, at first the surfactant assembles in micelles due to its hetero-polar nature and then Triton-X micelles wraparound EG molecules in the electrolyte (Ge *et al*., 2007). This is the reason why Triton-X restrains EG and thus prevents the electrooxidation of EG. Due to the reduced the number of CO for adsorption on the Pt catalyst sites and anticipates EG adsorbing on the working electrode. According to Fig. 8B, 8D, and 8F, EG oxidation diminished.

3.4.3 Effect of glycol-based coolants on the ORR characteristics

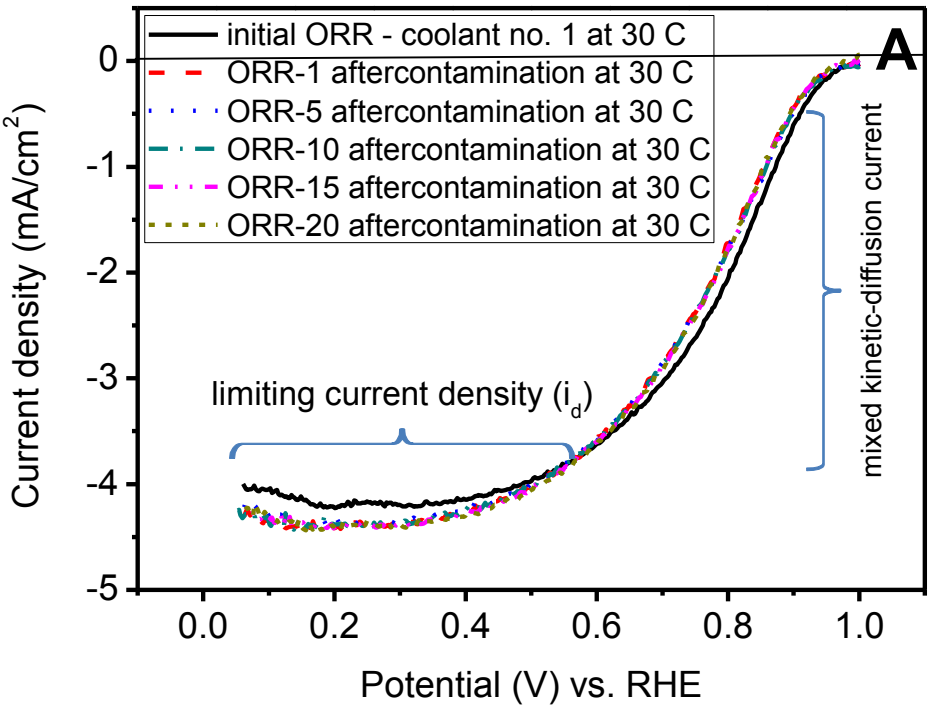

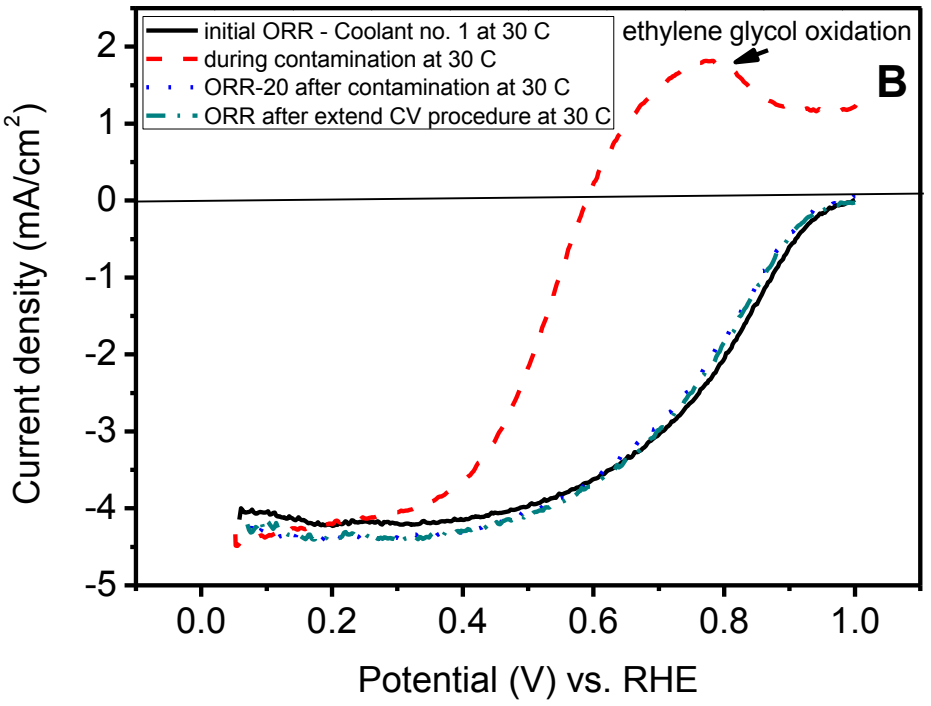

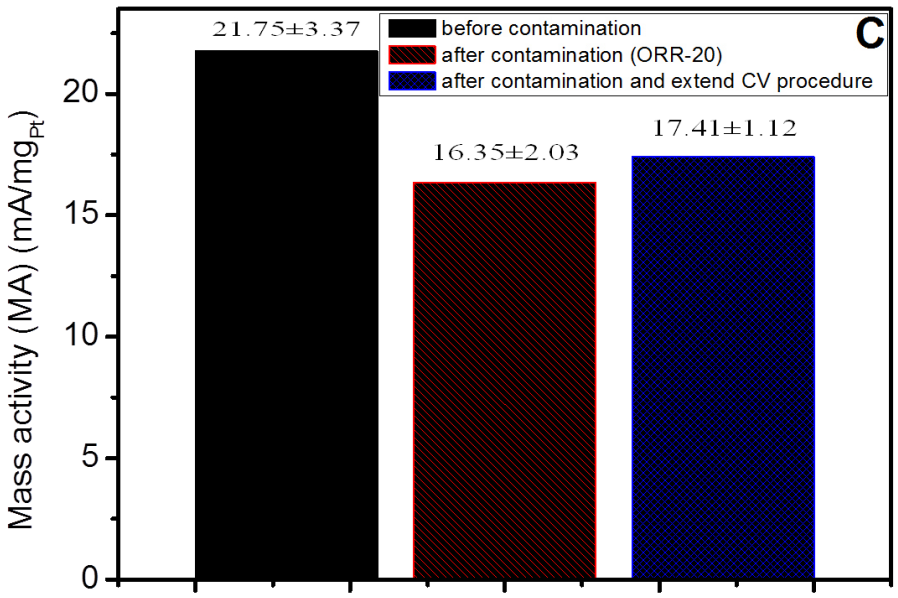

Fig. 10. **A)** Comparison initial ORR to after contamination with coolant no. 1 of ORR-1, ORR-5, ORR-10, ORR-15 and ORR-20 of the ORR polarization curve obtained in a 0.1M H_2SO_4 electrolyte at temperature 303K **B)** Comparison initial ORR, during contamination, after contamination with coolant no. 1 of ORR-20 and ORR after extened CV procedure **C)** Comparison MA calculated for initial MA to after contamination of ORR-1, ORR-5, ORR-10, ORR-15 and ORR-20 at temperature 303K. (ORR-1 as 1 cycle, ORR-5 as 5 cycles, ORR-10 as 10 cycles, ORR-15 as 15 cycles, ORR-20 as 20 cycles)

The initial ORR curve of the initial Pt/C working electrode has a defined diffusion-limiting current as mass transfer region from potential 0.10 to 0.50 V. The rotation rate controls the diffusion of oxygen process on the working electrode surface. The kinetic-diffusion control is under mixed region from kinetic and diffusion control at potential between $0.70 < E < 0.90$ V (Garsany *et al*., 2012). The catalytic activity of Pt/C electrocatalyst for the ORR is compared by its mass activity (MA) as calculated from the ORR curves shown in Fig. 10B using equation (3) and (4). The MA value is calculated using the mass transport-correction for catalyst-film RDEs normalization to the Pt-loading of the disk electrode, where the kinetic current, i_k, is obtained

from the value of the polarization curve at 0.90 V and the i_d at E = 0.30 V vs. RHE. These Pt MAs are compared in Fig. 9C. The MA measured for the clean Pt/C electrode is 21.75 ± 3.37 mA/mg_{Pt}. After contamination, the MA obtained for CV20 is equal to 16.35 ± 2.03 mA/ mg_{Pt}. By extending CV procedure of contaminated, the MA measured as 17.41 ± 1.12 mA/ mg_{Pt}. Fig. 9B, the ORR during contamination shows ethylene glycol oxidation at potential *ca.* 0.5-0.9 V.

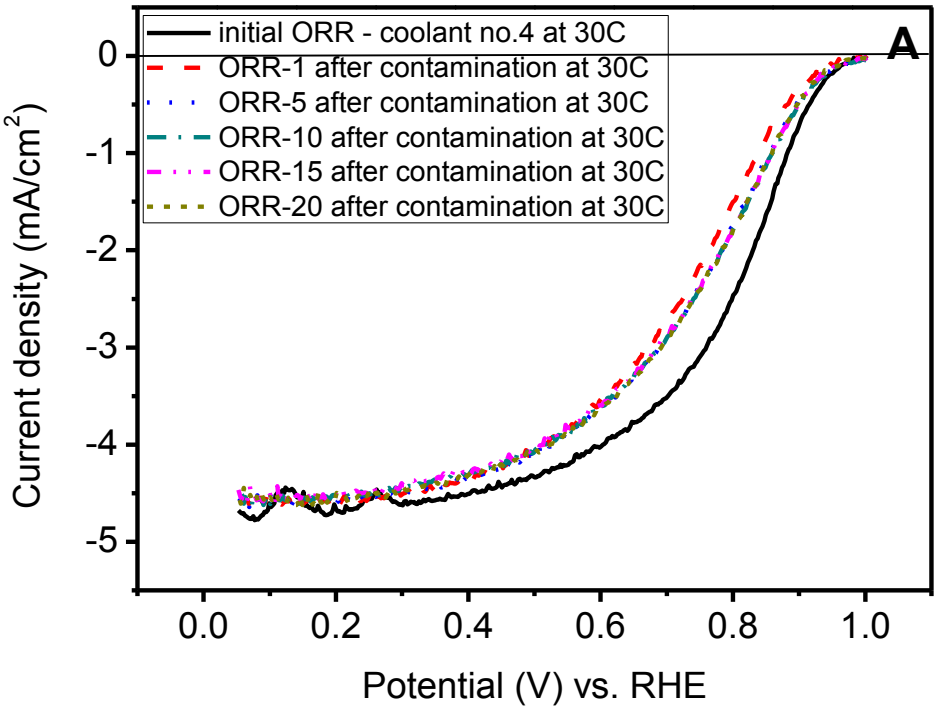

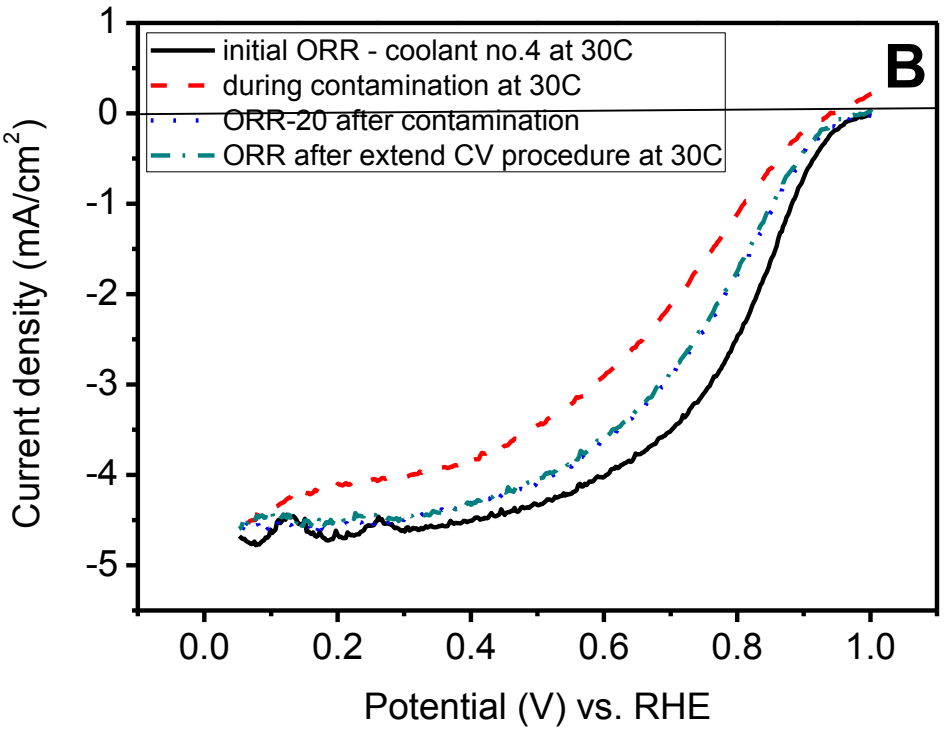
B
initial ORR - coolant no.4 at 30C
during contamination at 30C
ORR-20 after contamination
ORR after extend CV procedure at 30C
Current density (mA/cm^2)
Potential (V) vs. RHE
1
0
-1
-2
-3
-4
-5
0.0
0.2
0.4
0.6
0.8
1.0

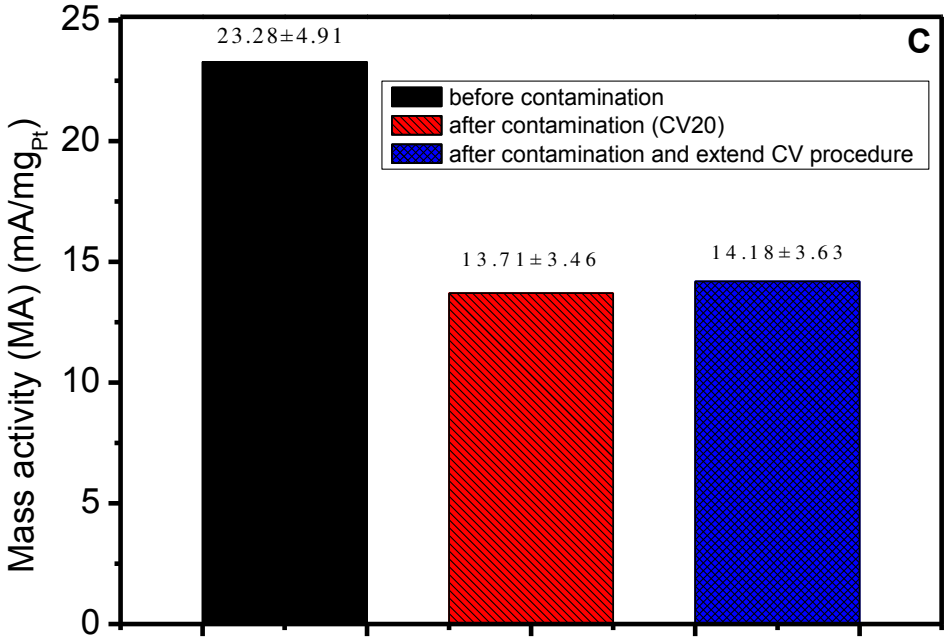
C
23.28±4.91
13.71±3.46
14.18±3.63
before contamination
after contamination (CV20)
after contamination and extend CV procedure
Mass activity (MA) (mA/mg$_{Pt}$)
25
20
15
10
5
0

Fig. 11. **A)** Comparison initial ORR to after contamination with coolant no. 4 of ORR-1, ORR-5, ORR-10, ORR-15 and ORR-20 of the ORR polarization curve obtained in a 0.1M H_2SO_4 electrolyte at temperature 303K **B)** Comparison initial ORR, during contamination, after contamination with coolant no. 4 of ORR-20 and ORR after extened CV procedure **C)** Comparison MA calculated for initial MA to after contaminated of ORR-1, ORR-5, ORR-10, ORR-15 and ORR-20 at temperature 303K. (ORR-1 as 1 cycle, ORR-5 as 5 cycles, ORR-10 as 10 cycles, ORR-15 as 15 cycles, ORR-20 as 20 cycles)

These Pt MAs for the measurements with coolant no.4 are compared in Fig. 11C. The MA measured for the initial Pt/C on working electrode is equal to 23.28 ± 4.91 mA/mg_{Pt}. After contamination with coolant no.4, the MA obtained for CV20 is equal to 13.71 ± 3.46 mA/mg_{Pt}. After contamination and extended CV procedure, the MA measured as 14.18 ± 3.63 mA/ mg_{Pt}. Fig. 11B, the ORR during contamination shows decreasing ethylene glycol oxidation, since the Triton-X in the coolant inhibits the adsorption of EG on the working electrode due to micelle formation.

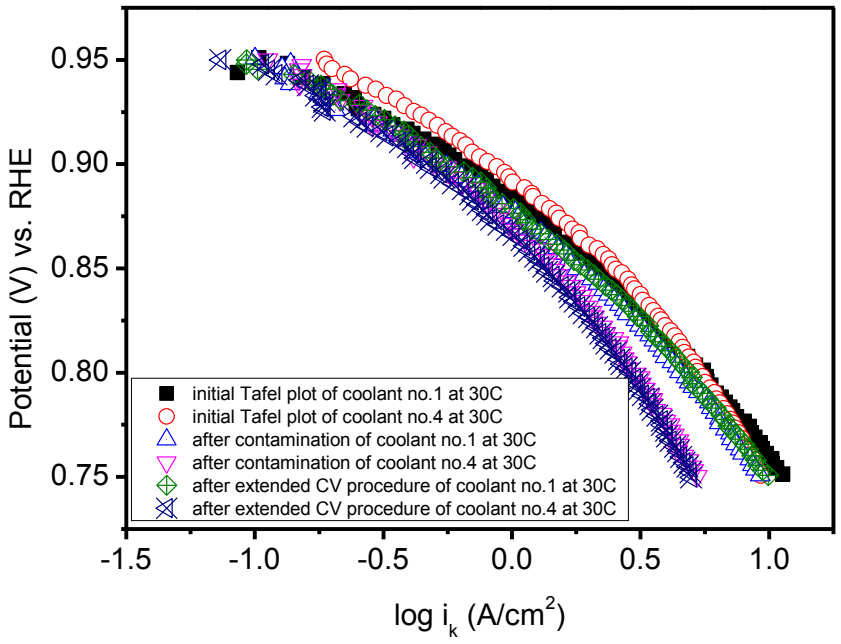

Fig. 12. Tafel plots of oxygen reduction on Pt electrocatalyst initial Tafel plots, after contamination and after extended CV procedure with coolant at 303K.

These results in Fig. 12 show the Tafel plot (log kinetic current (A/cm^2) vs. potential (V)) for Pt/C electrode in O_2 -purged, 0.1 M H_2SO_4 at 303 K. At low current densities (*lcd*) and potentials of E > 0.85 V, the Tafel slope is ~ -74 to -91 mV/decade. At high current densities (*hcd*) and potentials of E < 0.85 V to the Tafel slope increases to ~ -139 to -184 mV/decade. It is assumed that the Tafel slopes are controlled by both "energetic effects" (i.e. Temkin and Langmuir adsorption) (He *et al.*, 2010, Yang *et al.*, 2013, Gómez-Marin *et al.*, 2013). The Temkin adsorption isotherm for the ORR reaction considers the indirect changes of O_2 adsorption behavior due to the coverage of the Pt electrocatalyst surface with already chemisorbed oxygen-containing species as well as the heterogeneous reaction between adsorbed EG and the surface oxide (Gómez-Marin *et al.*, 2013, Vijh, 1971).

The Temkin adsorption isotherm mechanism (Vijh *et al.*, 1971):

$$Pt + H_2O \leftrightarrow PtOH + H^+ + e^- \quad (5)$$

$$Pt + RH \leftrightarrow PtR + H^+ + e^- \quad (6)$$

$$PtR + PtOH \leftrightarrow PtR' + H_2O + Pt \quad (7)$$

where RH as the EG and reaction (7) as rate determining step.

The Langmuir adsorption isotherm mechanism (Vijh *et al.*, 1971) :

$$Pt + H_2O \leftrightarrow PtOH + H^+ + e^- \quad (8)$$

$$RH + Pt \leftrightarrow PtRH \quad (9)$$

$$PtRH + PtOH \leftrightarrow PtR + H_2O \quad (10)$$

where RH as the EG and reaction (10) as rate determining step.

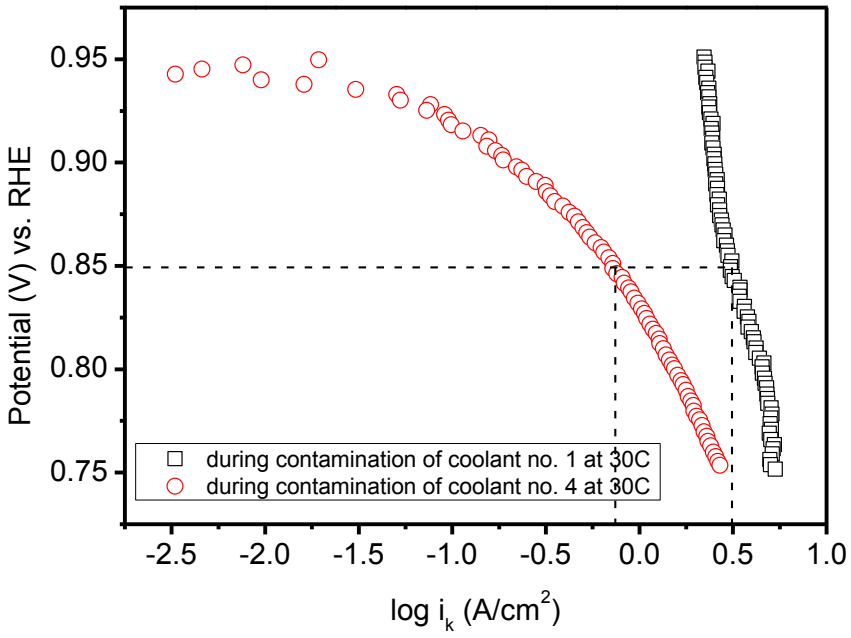

Fig. 13. Tafel plots of oxygen reduction on Pt electrocatalyst during contamination with coolant at 303K.

The Tafel slope during contamination with coolant no. 4 (Fig. 13) for the Pt/C electrode in O_2 - purged, 0.1 M H_2SO_4 at 303 K was ~ -78 mV/decade at low current densities (*lcd*) and potentials of E > 0.85 V. At high current densities (*hcd*) and potentials of E < 0.85 V it increases to ~ -171 mV/decade. The performance of the electrocatalysts is evaluated from kinetic current density (i_k), as seen in Figure 13. Pt/C electrocatalyst during contamination with coolant no. 1 displays higher mass activity than Pt/C electrocatalyst during contamination with coolant no. 4. Supposition, the Tafel slopes are controlled by Temkin adsorption isotherm at low current densities (*lcd*) and by Langmuir adsorption isotherm at high current densities (*hcd*) (He *et al.*,2010, Yang *et al.*, 2013, Gómez-Marin *et al.*, 2013). The ORR curve during contamination with coolant no.1 shows a significant oxidation peak in the range of approximately 0.5 to 0.9 V (see Fig. 10B). Hence, the Tafel slope for the ORR in presence of coolant no. 1 presents an abnormal slope (see Fig. 13) (Vijh *et al.*, 1971). On the other hand, the ORR curve for the measurements with coolant no.4 (during contamination) demonstrates a less pronounced oxidation of EG (Fig. 11B). Therefore, the corresponding shows Tafel slope typical value (see Fig. 13).

3.5 Summary and conclusion

The morphology of a commercial 30% Pt/C catalyst sample indicates a spherical powder aggregated structure with an average composition of 63.80% C, 4.65% O, 1.11% S, and 30.44% Pt. According to the effect of the ethylene glycol-based coolant on CV characteristics, ethylene glycol (EG) is adsorbed on the electrode surface at lower potentials, and the current starts increasing due to the electrooxidation of EG when the potential reaches 0.4-0.9 V. The oxidation of the EG produces formic acid as one of the major products and this acid is then further converted into intermediate $(CO)_{ads}$ on the active sites of Pt. By reacting with OH_{ads} from water, $(CO)_{ads}$ can be removed from the catalyst surface through the oxidation to CO_2. The water activation process on the active sites of Pt takes place at a higher potential and CO oxidation thus occurs at higher potentials of 0.5 to 0.9 V. As a result, the higher potential indicates CO oxidation on Pt surfaces while, on the other hand, the electrooxidation reaction of ethylene glycol can be reduced by Triton-X, a non-ionic surfactant. During contamination with the coolants no. 3, 4 and 5 (i.e. ethylene glycol/water and different concentrations of Triton-X), ethylene glycol electrooxidation at 0.5-0.9 V was reduced cycle by cycle, in comparison to coolant no.1 (ethylene glycol/water). The EG chains may be enclosed into Triton-X micelles. Triton-X can prevent the formation of CO from ethylene glycol oxidation on the active sites of the Pt electrocatalyst and thus the poisoning of the catalyst. Measurements with coolant no.4 (ethylene glycol / 0.0386 M of Triton-X) support this assumption. After and during contamination, with coolant no. 4 the loss of Pt ECSA was 0.02% and 37.74%, respectively.

Regarding the effect of the glycol-based coolant on the ORR characteristics, the ORR during contamination with coolant no. 1 indicates ethylene glycol oxidation in a potential range of *ca.* 0.5-0.9 V while, the ORR during contamination with coolant no. 4 shows reduced ethylene glycol electrooxidation, probably due to Triton-X. The MA measured for the clean Pt/C electrode was 21.75 ± 3.37 mA/mg_{Pt}. The MA obtained for CV20 after contamination with coolant no.1 was 16.35 ± 2.03 mA/ mg_{Pt} and MA measured after extending the CV procedure was 17.41 ± 1.12 mA/ mg_{Pt}. For measurement with coolant no. 4, the MA measured of the initial Pt/C working electrode was 23.28 ± 4.91 mA/mg_{Pt}, and after contamination only 13.71 ± 3.46 mA/mg_{Pt}. After further CV cycling (i.e. cleaning), the MA was 14.18 ± 3.63 mA/ mg_{Pt}.

At low current densities (*lcd*) and potentials of E > 0.85 V, Tafel slope values of ~ -74 to -91 mV/decade were obtained for the Pt/C electrode in O_2 –purged electrolyte after contamination

with coolant and after extending the CV procedure and region (O_2 evolution region). At high current density (*hcd*) and potentials of E < 0.85 V values of ~ -139 to -184 mV/decade were obtained. Therefore, it can be assumed that both "energetic effects" (Temkin and Langmuir adsorption) control the Tafel slopes.

4. Investigation of performance decrease of non-Pt based electrocatalysts in presence of ethanol leakage (section 2)

4.1 State of the art

Energy-converting equipment, either basic part or applications, alkaline direct ethanol fuel cells (ADEFCs) are deemed a fascinating option. They show positive attributes when compared to alternative type of fuel cells, e.g. high energy density for portable power sources. The fuel is ethanol in alkaline solution. Oxygen receives electrons originating from the anode through the outer circuit from the cathode. Recognized as reduction, the receipt of the electrons creates negatively charged oxygen ions. Chemical activity dictates the quantity of direct current generated by the electron flow from anode to cathode. One of the main areas of study into the enhanced activity of electron transfer, kinetic performance and oxygen adsorption on operational sites of electrocatalysts is the oxygen reduction reaction (ORR) on the cathode surface (Bikkarolla *et al*., 2014). The advancement of electrocatalysts in fuel cells for ORR is an important subject. Employing a non-noble electrocatalyst rather than a noble electrocatalyst serves as an incentive for this issue. ADEFCs are an appealing substitute because they are applicable for moveable as well as stationary power sources (Hung *et al*., 2014). Ethanol needs no pressurisation for storage. Further, it is economical, has low toxicity and good market possibility, as well as an elevated energy concentration compared to methanol at 8.0 and 6.1 kW kg^{-1}, respectively (Garcia *et al*., 2014). For the generation of carbon dioxide, water and electricity, ethanol is employed directly in ADEFCs. Researchers have tried to enhance the execution of ADEFCs through the advancement of electrocatalysts. The significant test for ADEFCs is examining the impact of non-noble metal electrocatalysts for reducing the cost of respectable platinum-based materials. Analysts have endeavoured to reduce the harming of the cathode surface because of ethanol crossing through the film. The efficiency of a fuel cell is influenced by ethanol crossover via a membrane from the anode to the cathode side. Electrical function loss is the consequence of cathode exposure to ethanol. Jamming or restraint of adsorption in oxygen molecules on the active catalyst surface occurs as the result of ethanol being adsorbed on the surface of the electrocatalyst. This study has examined the advancement of ethanol-tolerant cathode electrocatalysts for use in ADEFCs. A thermodynamic examination to explain the pH effect in assisting the 4 -electron transfer procedure in a fuel cell at high pH

(0.1 M KOH) was offered by Blizanac *et al*. (Blizanac *et al*., 2007), which had a comparatively negligible effect in comparison with the potential needed at low pH (0.1 M $HClO_4$). Very low concentration of peroxide was identified in 0.1 M of KOH electrolyte, 0.5-2.5%. Using an Ag (1 1 1) catalyst at a high pH, no specific chemical interaction between the catalyst and O_2 or O_2^- was required. However, a robust chemical connection was needed at low pH. The ORR displayed a $2e^-$ transfer with 100% H_2O_2 production in 0.1 M $HClO_4$. Ag/C electrocatalysts with various loading were investigated (Demarconnay *et al*., 2004). A colloidal procedure was employed to prepare the electrocatalysts, which displayed methanol-tolerance at concentrations higher than 0.1 M MeOH in NaOH electrolyte. The outcome of tungsten carbide on carbon (W_2C/C) and Ag with tungsten carbide deposited on carbon (Ag-W_2C/C) for ORR in alkaline media was researched. (Meng *et al*., 2006). They described no consequence of methanol on the performance of ORR. Enhancing ORR activity in methanol-possessing electrolyte, Ag-W_2C/C electrocatalysts displayed a synergistic effect. The most effective ORR activity and methanol-tolerance for varied molar intensities of methanol is displayed by FeCo-Fe-Pd/C (Fashedemi *et al*., 2013). A one-step process for synthesis was used for the preparation of the Ag/Mn_yO_x/C electrocatalyst. The supplement of methanol in 0.1 M NaOH solution for the Ag/Mn_yO_x/C composites exhibited minimal effect on ORR activity (Tang *et al*., 2011). A manganese oxide-based $NiMnO_x$/C material was promoted by Amanda *et al*. (Garcia *et al*., 2014). Electrochemical activity in an alkaline medium as ethanol-tolerant cathodes was identified by this $NiMnO_x$/C electrocatalyst. However, these catalysts showed high activity for ORR and ethanol-tolerance with an ethanol concentration of 1.0 M. Vanadium oxides are specified as important catalysts in many electronic technologies (Chakrabarti *et al*., 1999). Further, V_2O_5 is used in semiconductors, optical switching devices and write-erase media (Chain, 1991). Huang et al. studied vanadium nitride (VN) for ORR in alkaline electrolyte (Huang *et al*., 2014).

4.2 Goal of section 2

In this study, the ORR activity of Ag/C, $AgMnO_2$/C, $Ag_2V_4O_{11}$/C, V_2O_5/C and MnO_2/C electrocatalysts was investigated in 0.1 M and 1.0 M KOH solution with and without the presence of ethanol in different concentrations.

4.3 Experimental

Synthesis of Ag/C electrocatalyst

The Ag/C electrocatalyst was synthesized by the colloid method (Tang *et al*., 2011). The 20 wt. % Ag/C catalyst was prepared using a mixture of 599 mg trisodium citrate dehydrate (2.32 mmol) and 69.3 mg $AgNO_3$ (0.408 mmol), which were dissolved in 50 ml of ultra-pure water in a 250 ml beaker (first beaker). Next, the mixed solution was stirred until transparent. In a second beaker, 15.5 mg of $NaBH_4$ (0.410 mmol) was dissolved in 50 ml of ultra-pure water. After several minutes of stirring the Ag solution, a droplet of $NaBH_4$ solution was added to the first beaker solution. The colloid solution exhibited a yellowish-brown colour, indicating Ag nanomaterial. Over a period of 15-20 min, the entire $NaBH_4$ solution was dropped slowly into the fast-stirred Ag solution, with the resulting solution turning from yellowish-brown to dark brown. Then the Ag nanomaterial was dispersed for about 15-30 min. Afterward, 176 mg of Vulcan XC-72R carbon black was disseminated in 30 ml of ultra-pure water with an ultrasonic probe for about 10 min and was added slowly to the Ag nanoparticle solution under different stirring in order to obtain the supported electrocatalysts. Next, the mixture was stirred for 3 h. The suspension was centrifuged at 11400 rpm for 10 min. The Ag particle were filtrated and washed twice with ultrapure water. After that, the Ag/C catalyst was dried overnight in an oven at 90 °C. The resulting yield was between 88% and 93%.

Synthesis of MnO_2/C electrocatalyst

The MnO_2/C catalyst (Tang *et al*., 2011) was prepared by blending 140 mg of Vulcan XC-72R dispersed in 300 ml of an ethanol-water mixed solution (8:2 v/v). Afterward, 198 mg of $Mn(NO_3)_2{\cdot}4H_2O$ was added and the solvent from the slurry was removed by stirring over night at 60 °C. Finally, the MnO_2/C catalyst was calcined in a furnace at 400 °C for 2 h under a N_2 atmosphere (heating rate 5 °C min^{-1}).

Synthesis of $AgMnO_2$/C electrocatalyst

The $AgMn_xO_y$ electrocatalyst (Tang *et al*., 2011, Wu *et al*., 2014, Grimmer *et al*., 2016) obtained by mixing $AgNO_3$ and $KMnO_4$ (molar ratio 1:1) was dissolved in ultrapure water at 80 °C, which was acidified with a drop of 65% HNO_3. The solution was slowly cooled to 0 °C. The suspension turned into dark-blue needles and was precipitated. The $AgMn_xO_y$ was filtrated, then washed

with icy ultrapure water and dried. In the next step the $AgMnO_2$/C catalyst was synthesized using 462 mg of $AgMn_xO_y$ dissolved in 150 ml of ultrapure water at 40-50 °C. An appropriate amount of Vulcan XC-72R carbon black was added. The black slurry was dispersed by using the ultrasonic method for 15 min. After that, the water was slowly evaporated at a constant temperature of 60 °C. Finally, the $AgMn_xO_y$/C was calcined in a tubular furnace for 2 h at 400 °C in a N_2 atmosphere with a heating rate of 5 °C min^{-1} in order to obtain the $AgMnO_2$/C electrocatalyst.

Synthesis of $Ag_2V_4O_{11}$/C electrocatalyst

The $Ag_2V_4O_{11}$/C (Mao *et al*., 2005) was prepared based on a mixture of 2.5 mmol ethylenediamine ($C_2H_8N_2$), 2.5 mmol vanadium pentoxide (V_2O_5) and 2.5 mmol silver nitrate ($AgNO_3$) dissolved in 40 ml of ultra-pure water. Then, the solution was synthesized by using reflux distillation under an ethylene glycol bath at 180 ˚C for 48 h. Then the colour of the solution was dark. The catalysts nanoparticles were filtrated and washed twice with ultra-pure water and ethanol. The solvent was removed overnight at room temperature (first beaker). Next, 1.34 g of Vulcan XC-72R carbon black was dispersed in 30 ml ultrapure water with 3 ml of 2-propanol, which was stirred slowly to fast for 10 min (second beaker). A short time later, 0.53 g of $Ag_2V_4O_{11}$ nanoparticles, from first beaker, were added to the second beaker and were stirred slowly for 3 h. Finally, an oven was used to dry the $Ag_2V_4O_{11}$/C overnight at 90 ˚C.

Synthesis of V_2O_5/C electrocatalyst

The V_2O_5/C electrocatalyst was synthesized by mixing of 1.60 g Vulcan XC-72R carbon black, 30 ml of ultra-pure water and 3 ml of 2-propanol. The solution was stirred slowly for 10 min. Then, 0.4 g of V_2O_5 was added and stirred slowly for 3 h. Finally, an oven was utilized to dry the V_2O_5/C overnight at 90 ˚C.

A commercial Pt/C particles catalyst (Alfa Aesar) was used as reference material for comparing its activity, stability and ethanol tolerance to the prepared catalysts.

4.3.1 Characterisation of catalyst materials

The morphology of the Ag/C, $AgMnO_2$/C, $Ag_2V_4O_{11}$/C, V_2O_5/C and MnO_2/C electrocatalysts was investigated by using a transmission electron microscopy (TEM). Energy dispersive X-ray spectroscopy (EDX) was used to determine the element compositions in the electrocatalysts.

4.3.2 Electrode Preparation

All experiments were carried out in a 1.0 M or 0.1 M KOH working electrolyte with the standard three-electrode configuration with and without ethanol at different temperatures. The working electrolytes were prepared from ultra-pure water (18 MΩ-cm, Barnstead Nanopure). A platinum electrode was used as counter electrode and a reversible hydrogen electrode (RHE) as reference electrode. The working electrode was a glassy carbon a rotating disk electrode (RDE). Ultra-high purity nitrogen (N_2) and oxygen (O_2) were employed to flush the electrolyte for the respective cyclic voltammetry measurements. Electrocatalysts loading on the glassy carbon was 56 μg cm^{-2}. All electrochemical measuring techniques were performed using a potentionstat/galvanostat (Autolab).

4.3.3 Procedure

The electrochemical measuring procedure for the different alkaline electrolyte concentrations is shown in Table 1.

Table 1: Cyclicvoltammetry (CV) and oxygen reduction reaction (ORR) in 0.1 M and 1.0 M KOH at 30 °C.

	Method	Potential cycling	Scan rate	Purge
Condition 1. (to clean the catalyst)	CV	between 0.2 V to 1.4 V for 10 cycles	50 mV s^{-1}	N_2- atmosphere
Condition 2. (Base CV)	CV	between 0.2 V to 1.4 V for 3 cycles	10 mV s^{-1}	N_2- atmosphere
Condition 3.	ORR	between 1.2 V	10 mV s^{-1}	N_2- atmosphere

(Base ORR)		to 0.2 V for 2 cycles		
Condition 4. (Base CV)	CV	between 0.2 V to 1.4 V for 3 cycles	10 mV s^{-1}	O_2- atmosphere
Condition 5. (different rpm*)	ORR	between 1.2 V to 0.2 V for 2 cycles	10 mV s^{-1}	O_2- atmosphere
Condition 6. (different rpm**) (with 0.1MEtOH)	ORR	between 1.2 V to 0.2 V for 2 cycles	10 mV s^{-1}	O_2- atmosphere
Condition 7. (different rpm**) (with 0.5MEtOH)	ORR	between 1.2 V to 0.2 V for 2 cycles	10 mV s^{-1}	O_2- atmosphere
Condition 8. (different rpm**) (with 1.0MEtOH)	ORR	between 1.2 V to 0.2 V for 2 cycles	10 mV s^{-1}	O_2- atmosphere

*0, 400, 600, 900, 1200, 1600 and 2000 rpm

**0 and 1600 rpm

4.4 Results and Discussions

4.4.1 Physical characterization of Ag/C, $AgMnO_2$/C, $Ag_2V_4O_{11}$/C, V_2O_5/C and MnO_2/C catalysts

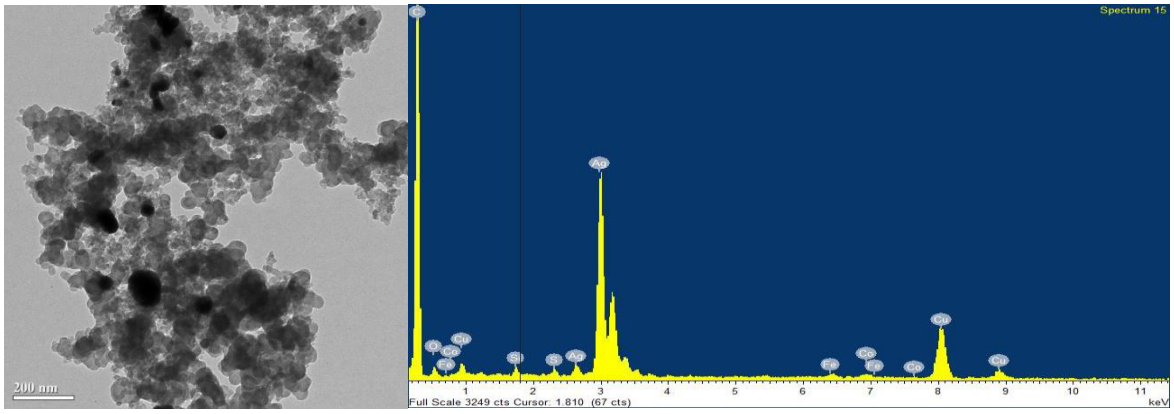

Fig. 1: Transmission electron microscopy (TEM) and Energy-dispersive X-ray spectroscopy (EDX) of the Ag/C catalyst.

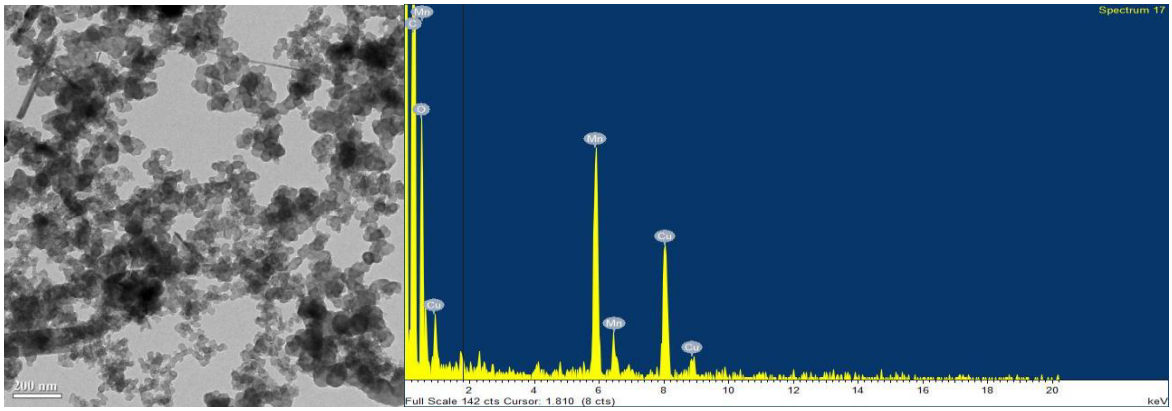

Fig. 2: Transmission electron microscopy (TEM) and Energy-dispersive X-ray spectroscopy (EDX) of the MnO_2/C catalyst.

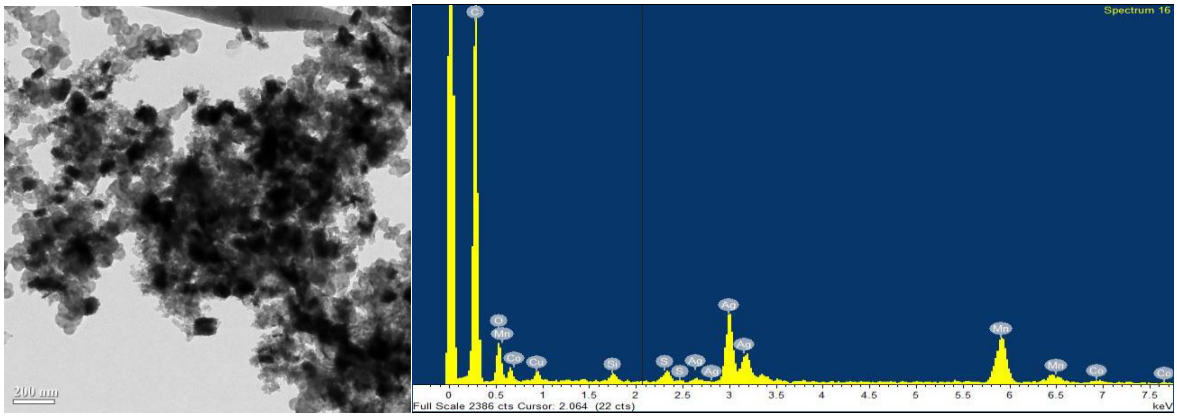

Fig. 3: Transmission electron microscopy (TEM) and Energy-dispersive X-ray spectroscopy (EDX) of the $AgMnO_2$/C catalyst.

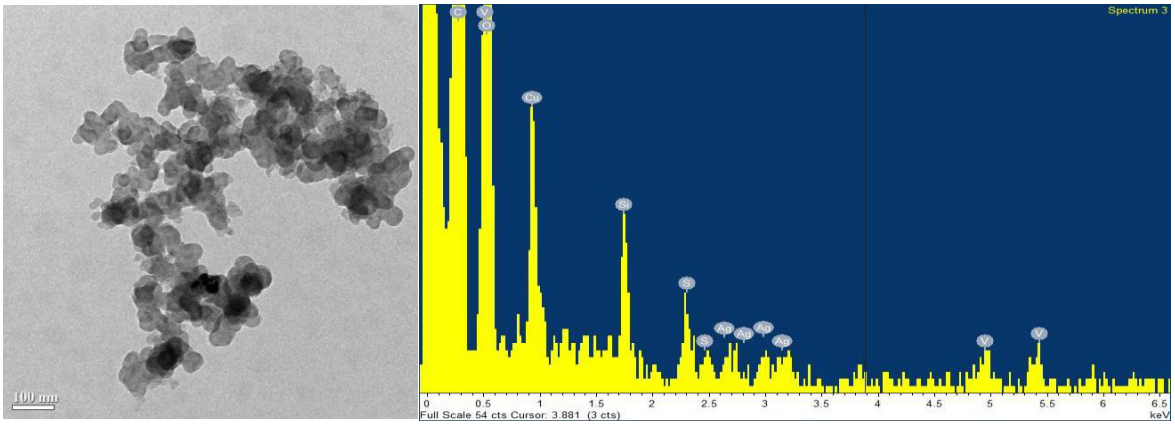

Fig. 4: Transmission electron microscopy (TEM) and Energy-dispersive X-ray spectroscopy (EDX) of the $Ag_2V_4O_{11}$/C catalyst.

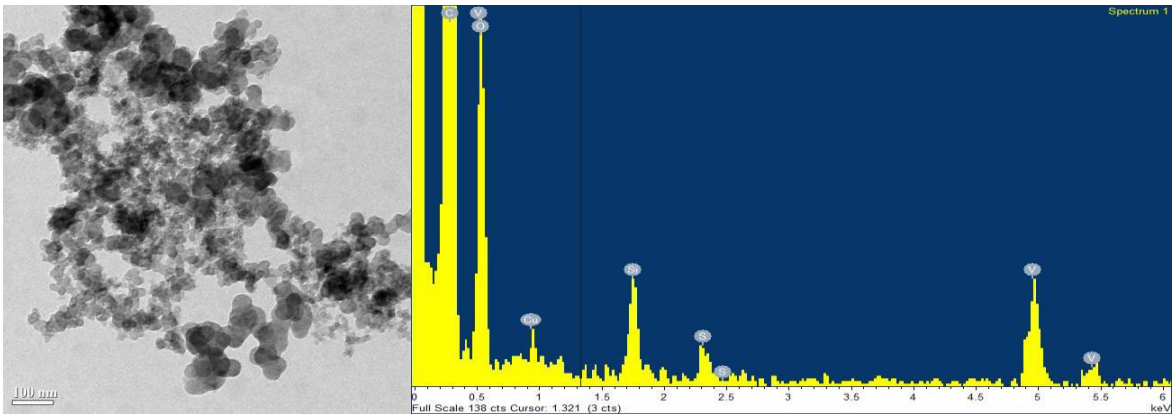

Fig. 5: Transmission electron microscopy (TEM) and Energy-dispersive X-ray spectroscopy (EDX) of the V_2O_5/C catalyst.

Aggregated spherical and branch-like particles morphologies were detected by TEM. The grey spherical particles and grey branch-like particles are carbon black, which means the branch-like particles are probably manganese oxides (see Fig. 1.-5.) (Sun *et al*., 2011). The Ag or Mn metal are the dark spherical particles. A majority of the carbon in the Ag, V and Mn composition was also observed by EDX analysis (as shown in Fig. 1.-5.). The EDX analysis shows Ag, V and Mn in quantities of *ca*. 11.6%, 11.3% and 13.6%, respectively.

4.4.2 Electrochemical measurements

4.4.2.1 Base cyclic voltammograms of Ag/C, $AgMnO_2$/C, $Ag_2V_4O_{11}$/C, V_2O_5/C and MnO_2/C catalysts

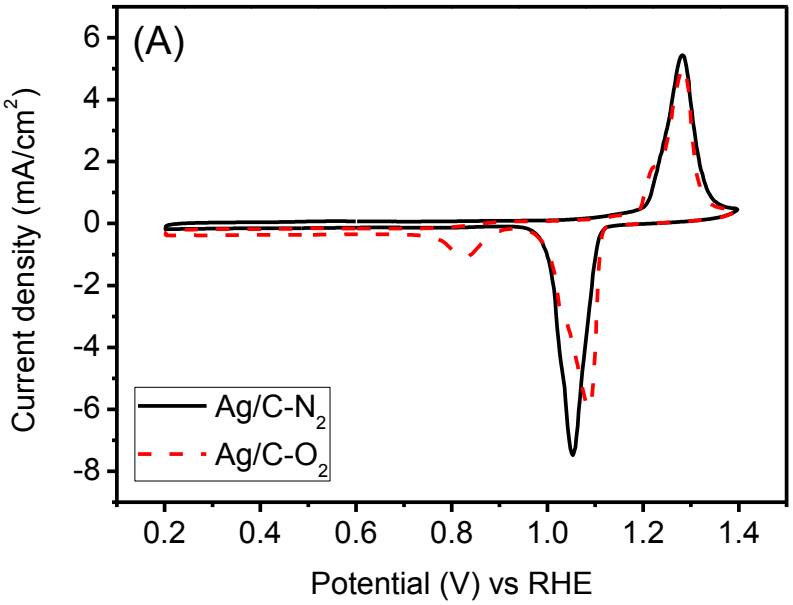

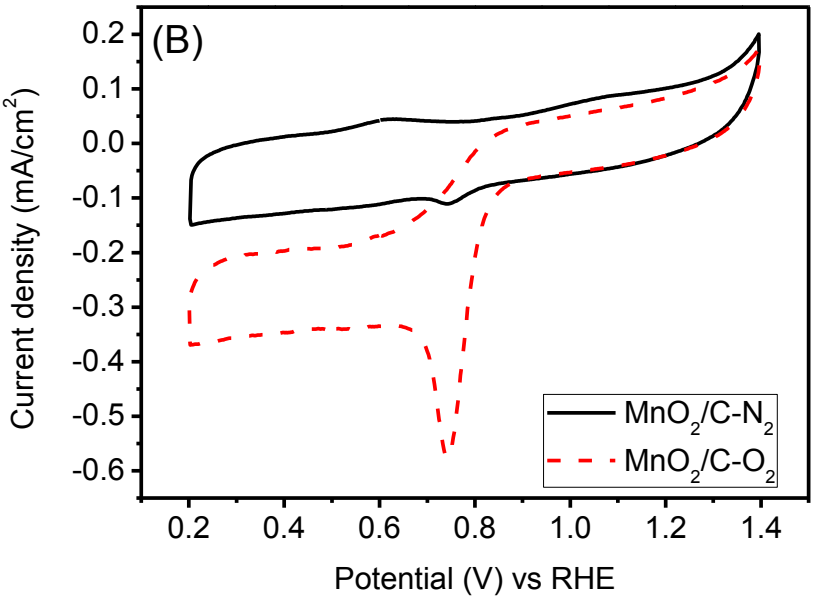
(B)
Current density (mA/cm^2)
Potential (V) vs RHE
MnO_2/C-N_2
MnO_2/C-O_2

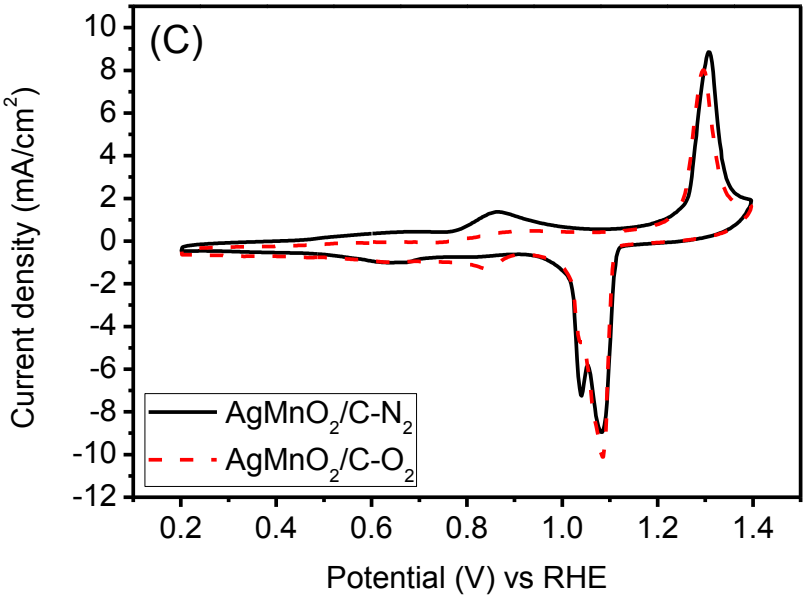
(C)
Current density (mA/cm^2)
Potential (V) vs RHE
$AgMnO_2$/C-N_2
$AgMnO_2$/C-O_2

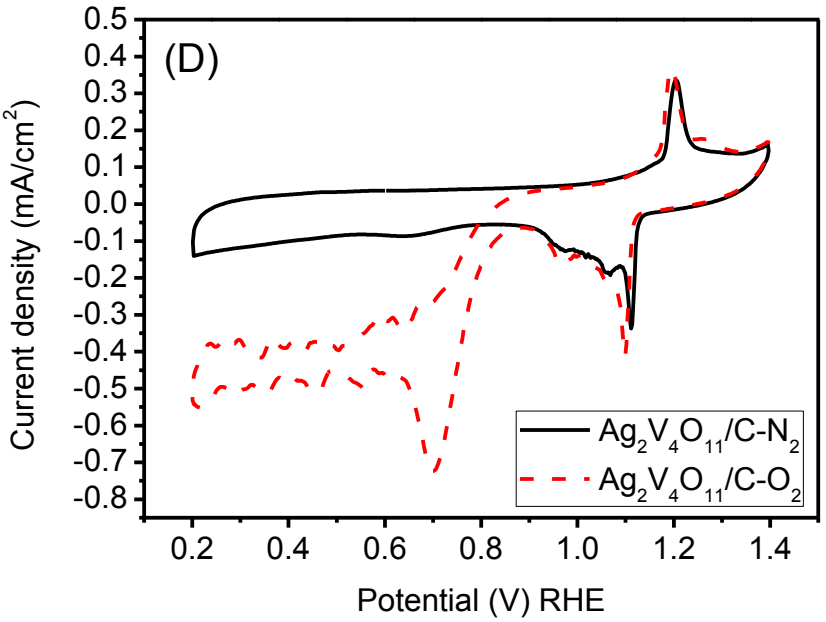
(D)
Current density (mA/cm^2)
Potential (V) RHE
$Ag_2V_4O_{11}$/C-N_2
$Ag_2V_4O_{11}$/C-O_2

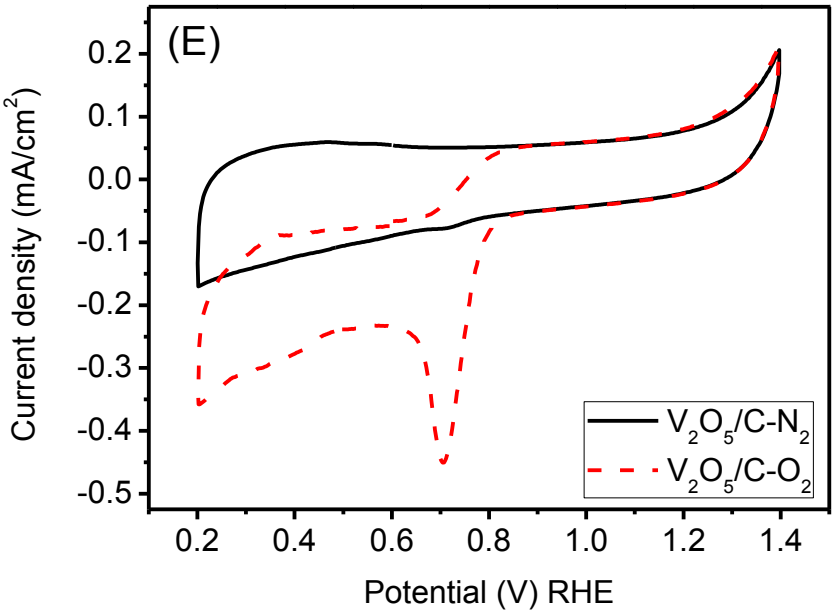
(E)
Current density (mA/cm^2)
Potential (V) RHE
V_2O_5/C-N_2
V_2O_5/C-O_2

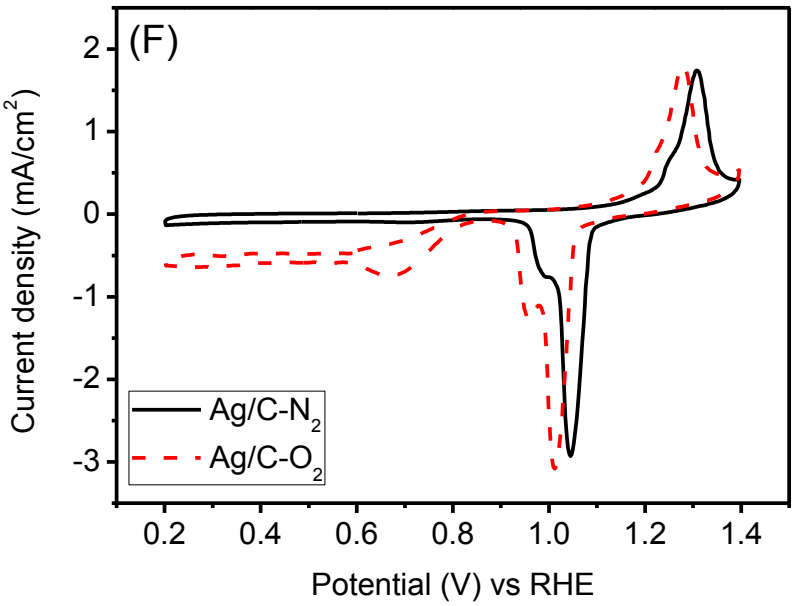
(F)
Current density (mA/cm^2)
Potential (V) vs RHE
Ag/C-N$_2$
Ag/C-O$_2$
2
1
0
-1
-2
-3
0.2
0.4
0.6
0.8
1.0
1.2
1.4

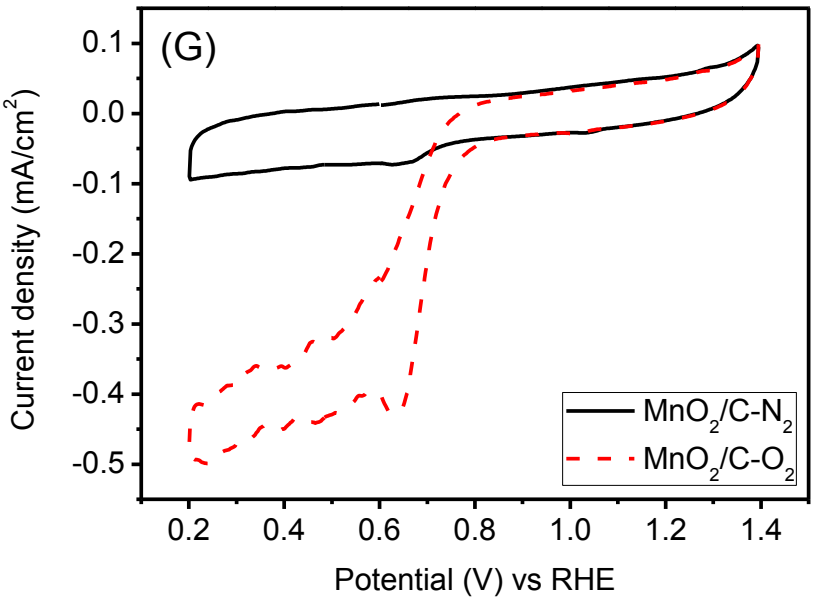
(G)
Current density (mA/cm^2)
Potential (V) vs RHE
MnO$_2$/C-N$_2$
MnO$_2$/C-O$_2$
0.1
0.0
-0.1
-0.2
-0.3
-0.4
-0.5
0.2
0.4
0.6
0.8
1.0
1.2
1.4

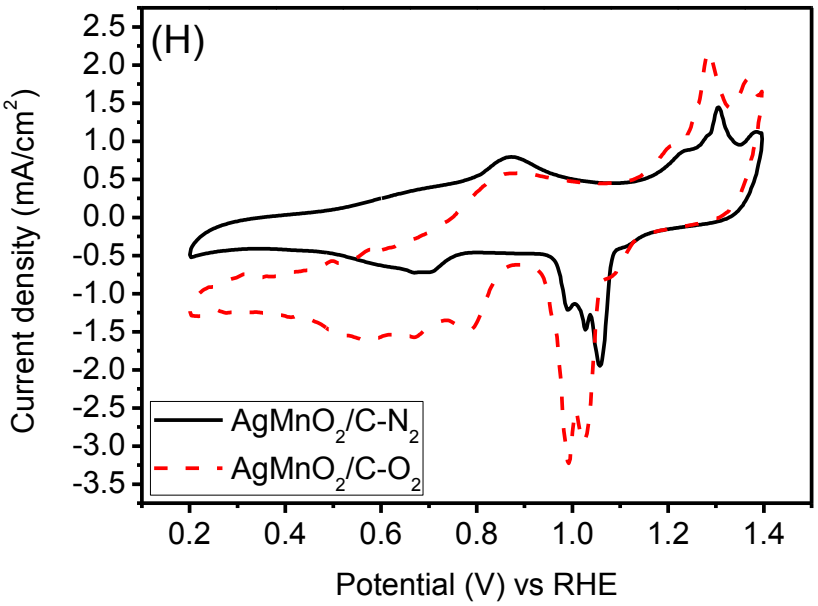
(H)
Current density (mA/cm^2)
Potential (V) vs RHE
AgMnO$_2$/C-N$_2$
AgMnO$_2$/C-O$_2$

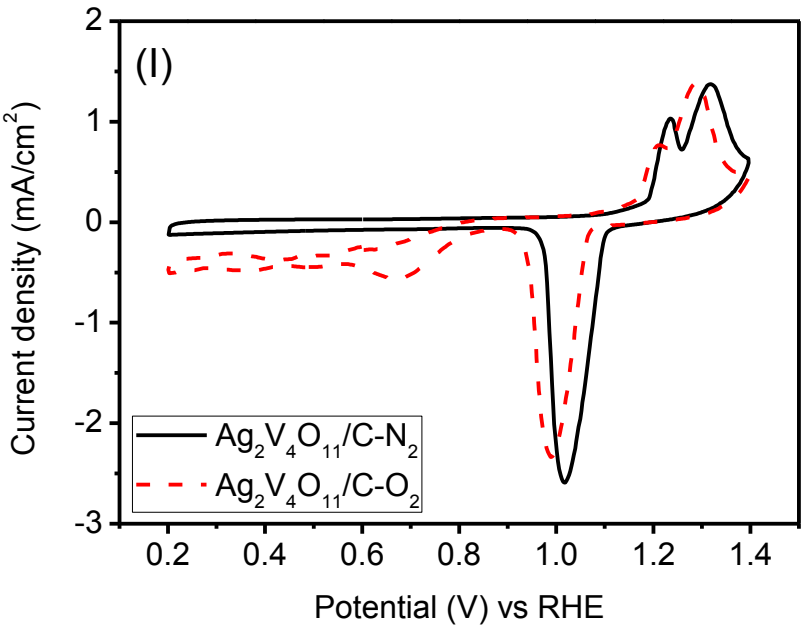
(I)
Current density (mA/cm^2)
Potential (V) vs RHE
Ag$_2$V$_4$O$_{11}$/C-N$_2$
Ag$_2$V$_4$O$_{11}$/C-O$_2$

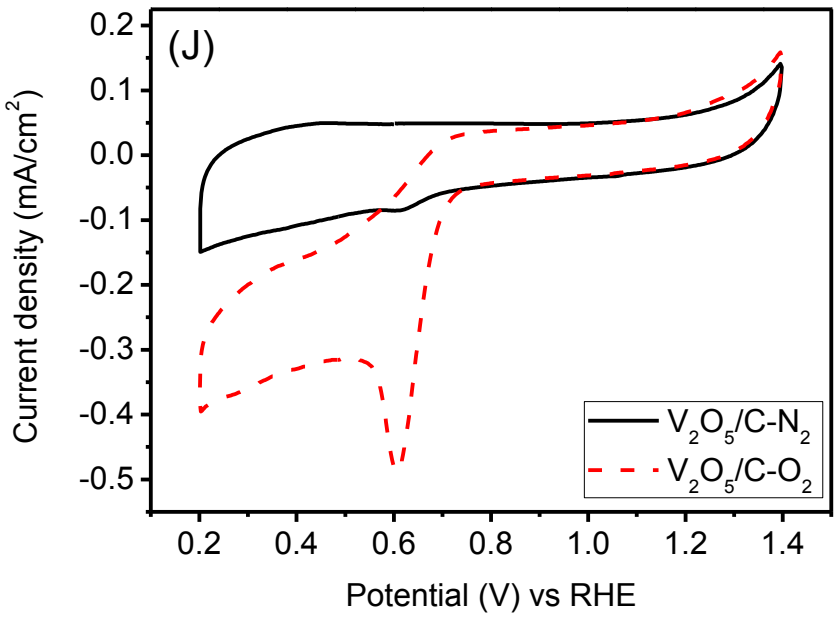

Fig. 6: Cyclic voltammograms of **(A)** Ag/C, **(B)** MnO_2/C, **(C)** $AgMnO_2$/C, **(D)** $Ag_2V_4O_{11}$/C and **(E)** V_2O_5/C catalysts in 1.0 M KOH electrolyte and **(F)** Ag/C, **(G)** MnO_2/C, **(H)** $AgMnO_2$/C **(I)** $Ag_2V_4O_{11}$/C and **(J)** V_2O_5/C catalysts in 0.1 M KOH electrolyte saturated with N_2 and O_2 at 30 °C and a sweep rate of 10 mV s^{-1}

The oxidation of Ag on the surface of the RDE showed the peak of Ag_2O films (see Figs. 6A, 6C, 6D and 6F). In the bulk, oxidation peaks of AgOH and Ag_2O are identified at the potential of around 1.29 V and 1.35 V (Tang *et al.*, 2011 and Wu *et al.*, 2014). The Ag oxidation peak occurs in the potential range between 1.3 V and 1.4 V. At potentials of 0.7 V and 0.8 V, $Mn(OH)_2$ is transformed into Mn_2O_3 and MnOOH. The oxidation peak is displayed at approximately 1.0 V, which indicates the oxidation of MnOOH to MnO_2 (Tang *et al.*, 2011). The overlap of the oxidation peaks for Ag and MnO_2 is exhibited at the $AgMnO_2$/C electrocatalysts. However, the reduction peak of $AgMnO_2$ is higher than the reduction peak of Ag in saturated N_2 and O_2. A large reduction peak with the $AgMnO_2$/C appears between the potentials of 0.2 V and 0.8 V in 0.1 M KOH in presence of O_2. The $AgMnO_2$/C electrocatalysts are shown to be advantageous for improving ORR activity.

4.4.2.2 Electrocatalytic activity for oxygen reduction reaction on $AgMnO_2$/C and Pt/C electrocatalysts in (A) 1.0 M and (B) 0.1 M of KOH at 30 °C

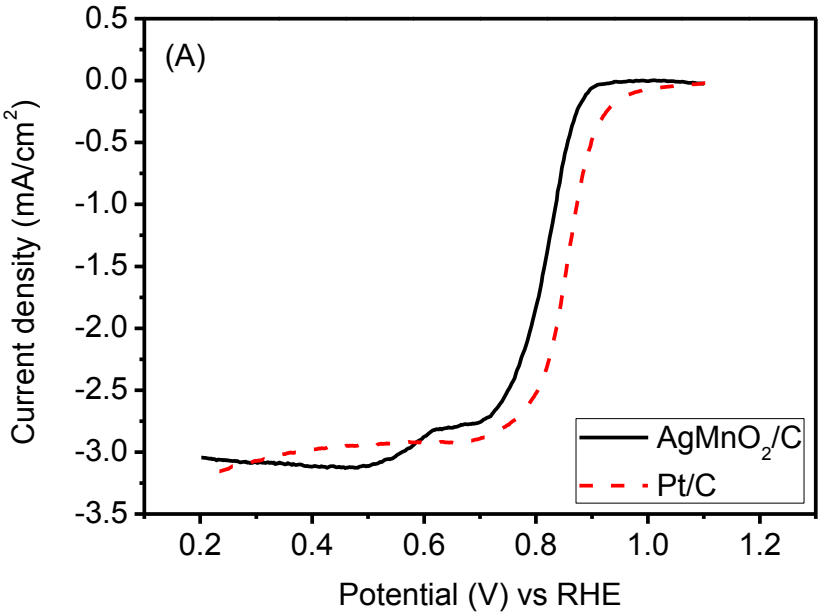

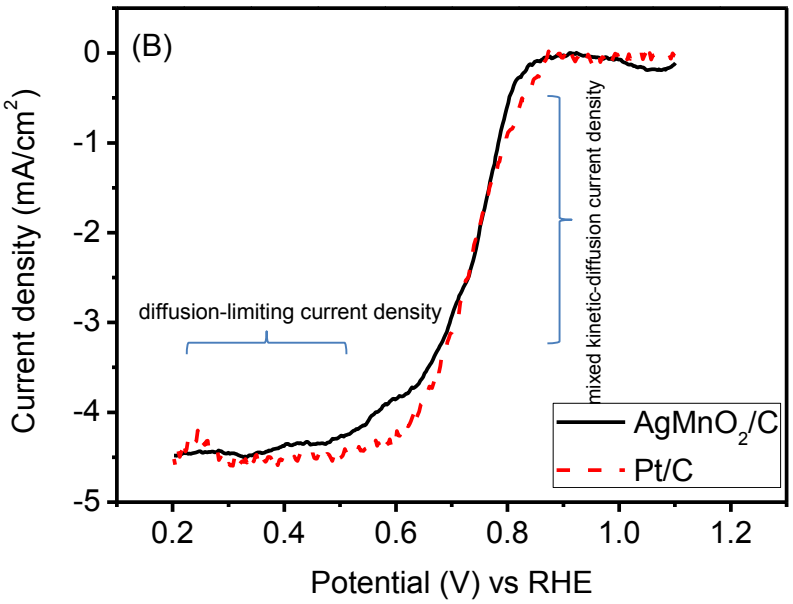

Fig. 7: Linear potential scan curves of $AgMnO_2/C$ and Pt/C electrocatalysts on a rotating disk electrode (RDE) in an O_2-saturated **(A)** 1.0 M and **(B)** 0.1 M of KOH at 30 °C, with a sweep rate of 10 mV s^{-1} and rotation rate of 1600 rpm.

The initial ORR polarisation curve of the catalysts shows a well-defined diffusion-limiting current in a potential range between 0.20 V and 0.70 V, while between the potentials of 0.70 V and 0.90 V the region under mixed kinetic-diffusion control is displayed (Fig. 7.) (Garsany *et al.*, 2012). The performance of the $AgMnO_2/C$ electrocatalyst is compared with the Pt/C electrocatalyst, which is found to have similar active at 30 °C (Fig. 3.). A comparison of the cost for the Ag-based electrocatalyst (19.09 USD/oz) shows it to be much cheaper than the Pt/C electrocatalysts (1,053.50 USD/oz) (Current prices from *www.gold-eagle.com* on September 12, 2016).

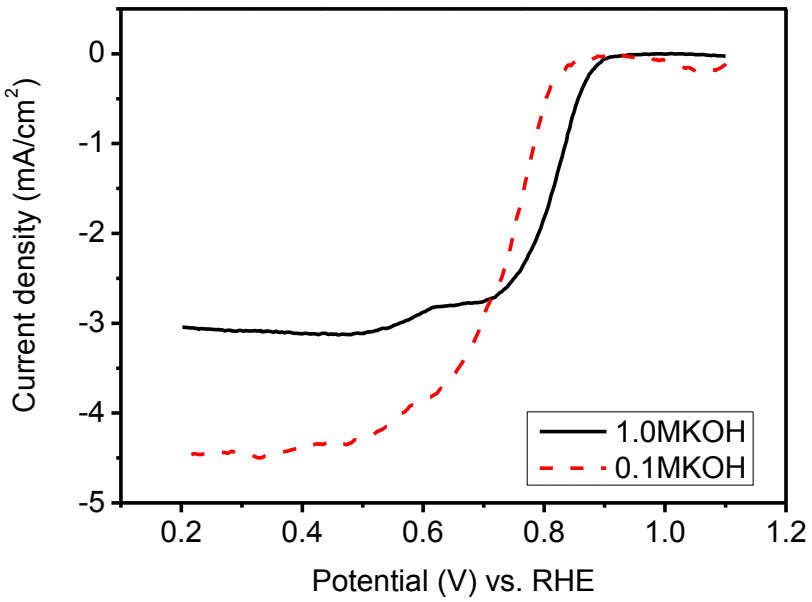

Fig. 8: Linear potential scan curves of $AgMnO_2/C$ on a rotating disk electrode in O_2 saturated 0.1 M and 1.0 M KOH at 30 °C, with a sweep rate of 10 mV s^{-1} and a rotation rate of 1600 rpm.

The ORR polarisation curves of the $AgMnO_2/C$ catalyst in an O_2 saturated 0.1 M and 1.0 M KOH are shown in Fig. 8., which imply that performance activity increases with decreasing

KOH concentration. The current density activity of reduction depends on O_2 solubility into the KOH working electrolyte. Increasing the alkaline electrolyte concentration, the O_2 diffusion coefficient indicated an increased viscosity of the alkaline electrolyte.

4.4.2.3 Base cyclic voltammograms of Ag/C, MnO_2/C, $AgMnO_2$/C, $Ag_2V_4O_{11}$/C and V_2O_5/C catalysts in 0.1 M KOH at temperatures of 30 °C, 40 °C, 50 °C and 60 °C.

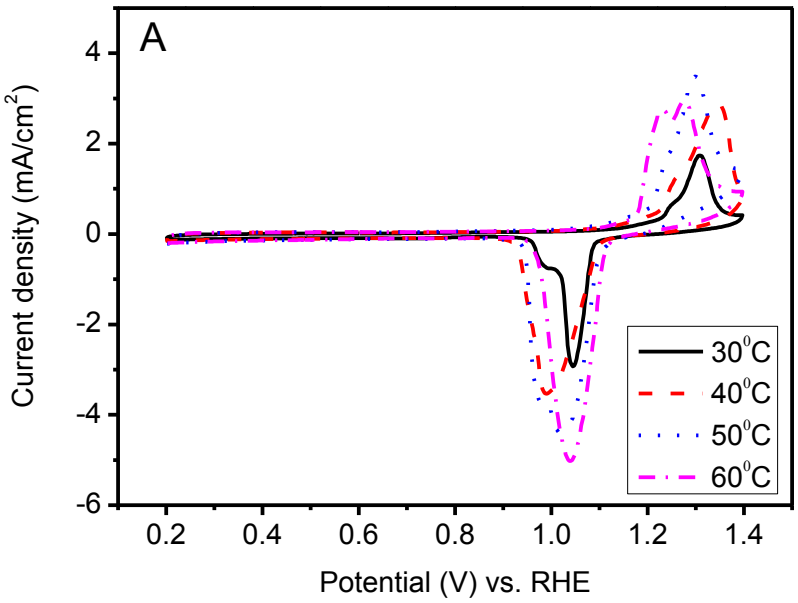

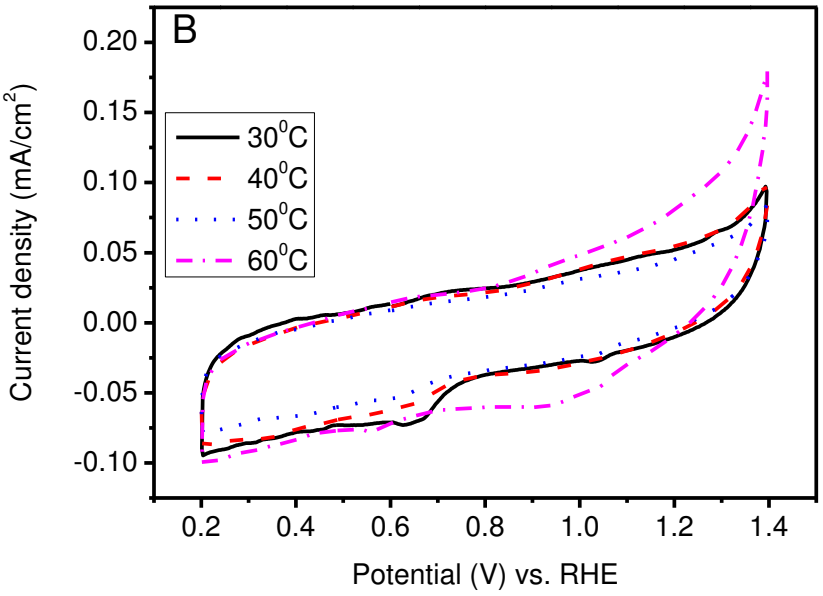
B
0.20
0.15
0.10
0.05
0.00
-0.05
-0.10
Current density (mA/cm^2)
30^{0}C
40^{0}C
50^{0}C
60^{0}C
0.2
0.4
0.6
0.8
1.0
1.2
1.4
Potential (V) vs. RHE

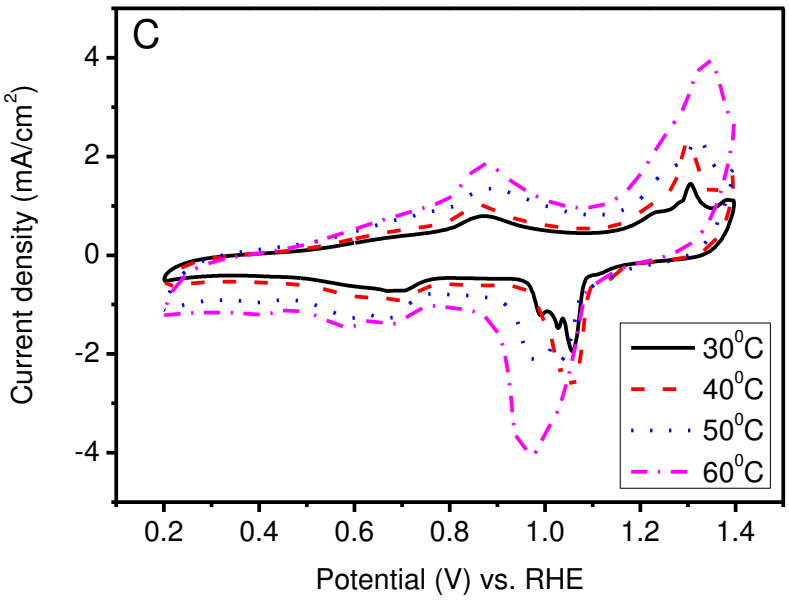
C
4
2
0
-2
-4
Current density (mA/cm^2)
30^{0}C
40^{0}C
50^{0}C
60^{0}C
0.2
0.4
0.6
0.8
1.0
1.2
1.4
Potential (V) vs. RHE

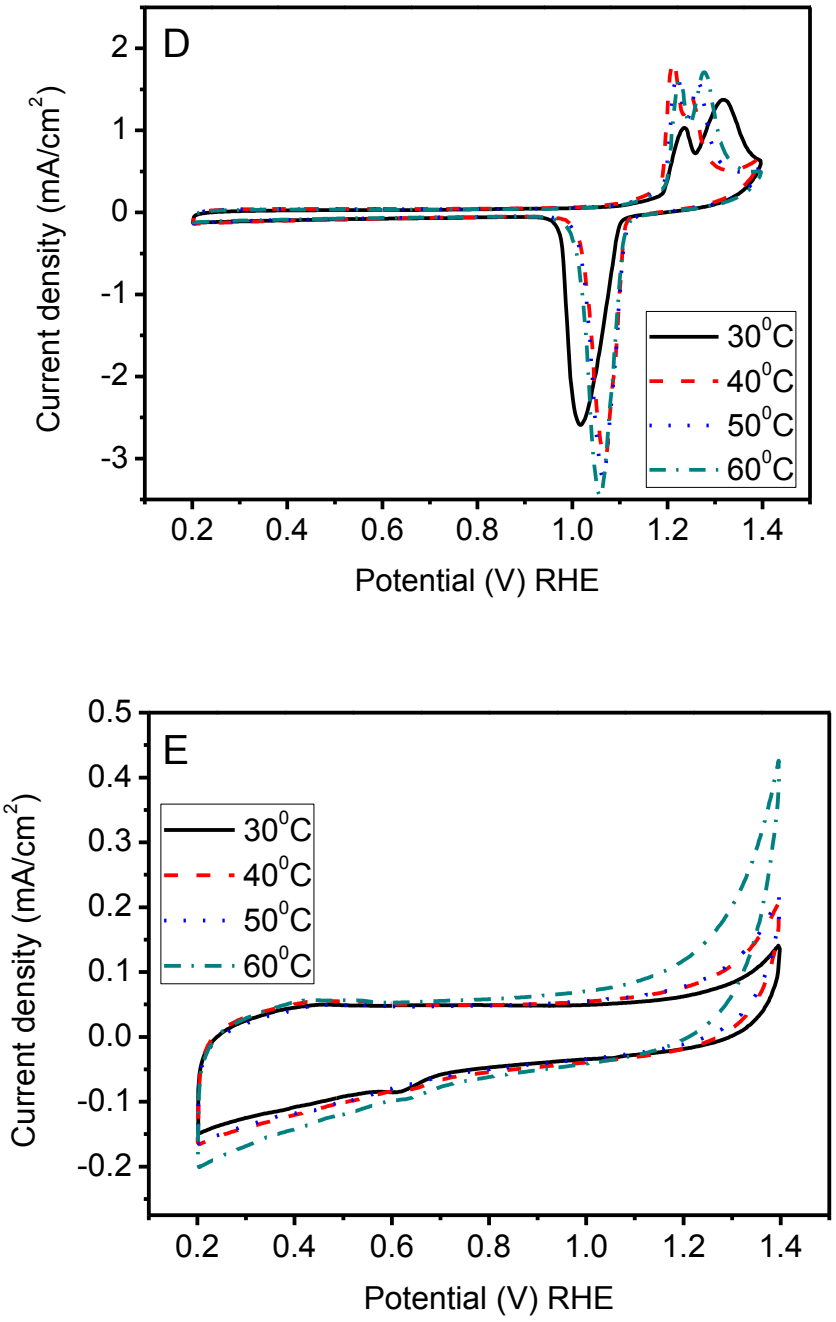

Fig. 9: Cyclic voltammograms for the **(A)** Ag/C, **(B)** MnO_2/C, **(C)** $AgMnO_2$/C, **(D)** $Ag_2V_4O_{11}$/C and **(E)** V_2O_5/C catalysts in 0.1 M KOH with N_2 saturation at a sweep rate of 10 mV s^{-1} and temperatures of 30°C, 40°C, 50°C and 60°C.

The Fig. 9. show the CV curves of Ag/C, MnO_2/C, $Ag_2V_4O_{11}$/C, V_2O_5/C and $AgMnO_2$/C electrocatalysts in N_2 saturated 0.1 M KOH at different temperatures. The Ag oxidation and reduction peak are dedicated between the potentials of 1.2 V and 1.4 V and 0.9 V and 1.1 V, respectively. The hights of the Ag oxidation and reduction peaks increases with increased temperature (see Fig. 9A and 9C). In the CV of the $AgMnO_2$/C catalyst is shown that the peak of $Mn(OH)_2$ changs to Mn_2O_3 and MnOOH at a potential of about 0.7 V to 0.9 V, respectively (see Fig. 9C). The oxidation peak is at approximately 1.0 V according to the oxidation of MnOOH to MnO_2 (Tang *et al*., 2011). $AgMnO_2$/C electrocatalysts exhibit overlap of the oxidation peaks of AgOH, Ag_2O and MnO_x (Tang *et al*., 2011). The reduction peak of the Ag/C, $Ag_2V_4O_{11}$/C and $AgMnO_2$/C catalyst at 60 °C is higher than the reduction peak at 30 °C (see Fig. 9C).

4.4.2.4 Kinetic oxygen reduction of Pt/C, Ag/C, MnO_2/C, $Ag_2V_4O_{11}$/C, V_2O_5/C and $AgMnO_2$/C catalysts in 0.1 M KOH at temperatures of 30 °C, 40 °C, 50 °C, 60 °C.

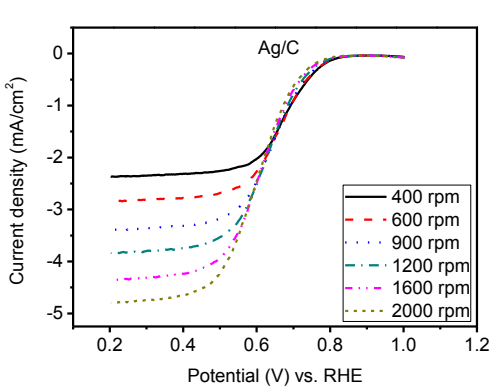

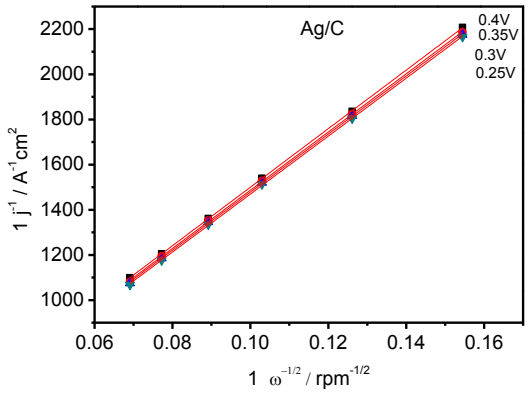

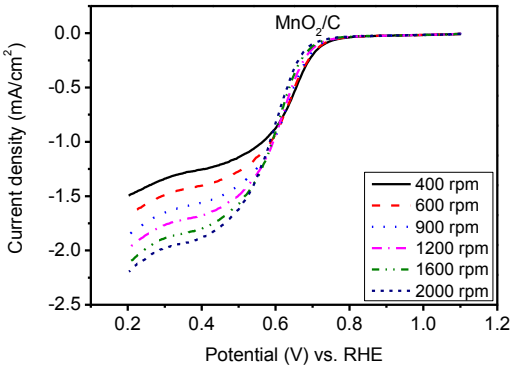
MnO2/C
Current density (mA/cm2)
Potential (V) vs. RHE
400 rpm
600 rpm
900 rpm
1200 rpm
1600 rpm
2000 rpm

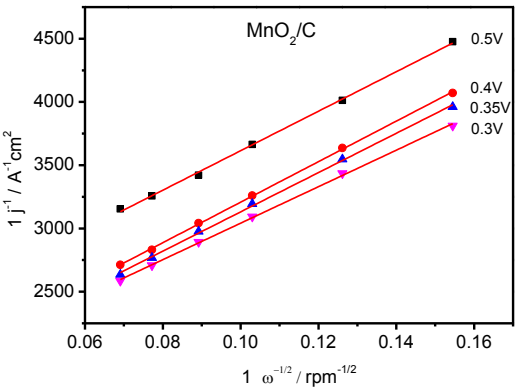
MnO2/C
0.5V
0.4V
0.35V
0.3V
1 j-1 / A-1cm2
1 ω-1/2 / rpm-1/2

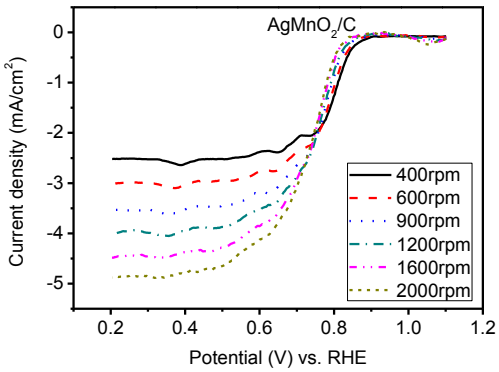
AgMnO2/C
Current density (mA/cm2)
Potential (V) vs. RHE
400rpm
600rpm
900rpm
1200rpm
1600rpm
2000rpm

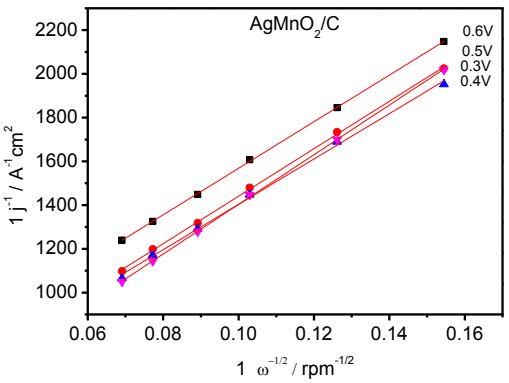
AgMnO2/C
0.6V
0.5V
0.3V
0.4V
1 j-1 / A-1cm2
1 ω-1/2 / rpm-1/2

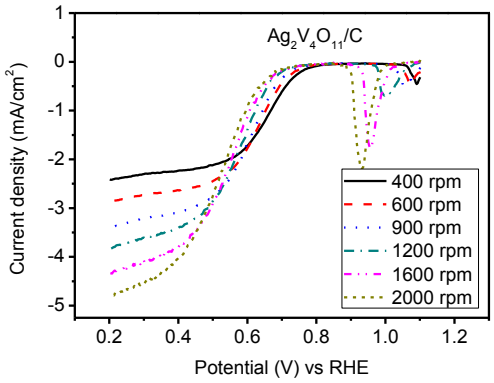
Ag2V4O11/C
Current density (mA/cm2)
Potential (V) vs RHE
400 rpm
600 rpm
900 rpm
1200 rpm
1600 rpm
2000 rpm

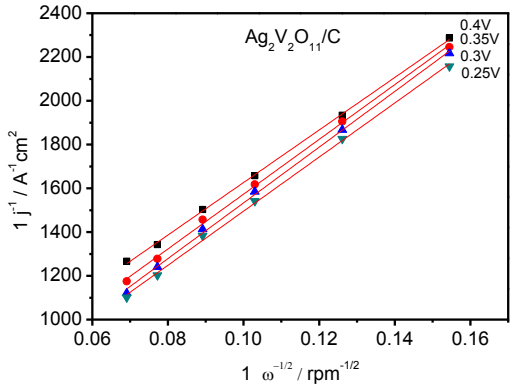
Ag2V2O11/C
0.4V
0.35V
0.3V
0.25V
1 j-1 / A-1cm2
1 ω-1/2 / rpm-1/2

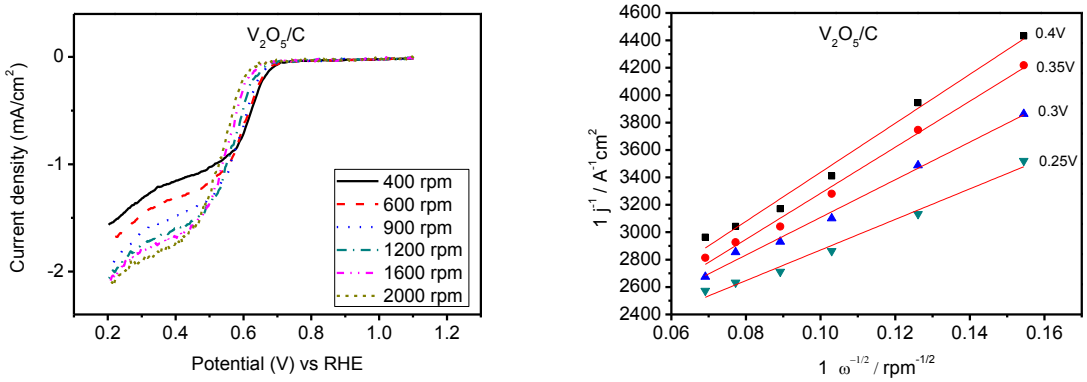

Fig. 10: Oxygen reduction reaction polarisation curves of Pt/C, Ag/C, MnO_2/C, $Ag_2V_4O_{11}$/C, V_2O_5/C and $AgMnO_2$/C catalysts on a rotating disk electrode in an O_2 saturated 0.1 M KOH at 30 °C with a sweep rate of 10 mV s^{-1}. Koutecky-Levich plots of Ag/C, MnO_2/C, $Ag_2V_4O_{11}$/C, V_2O_5/C and $AgMn_3O_4$/C at different potentials.

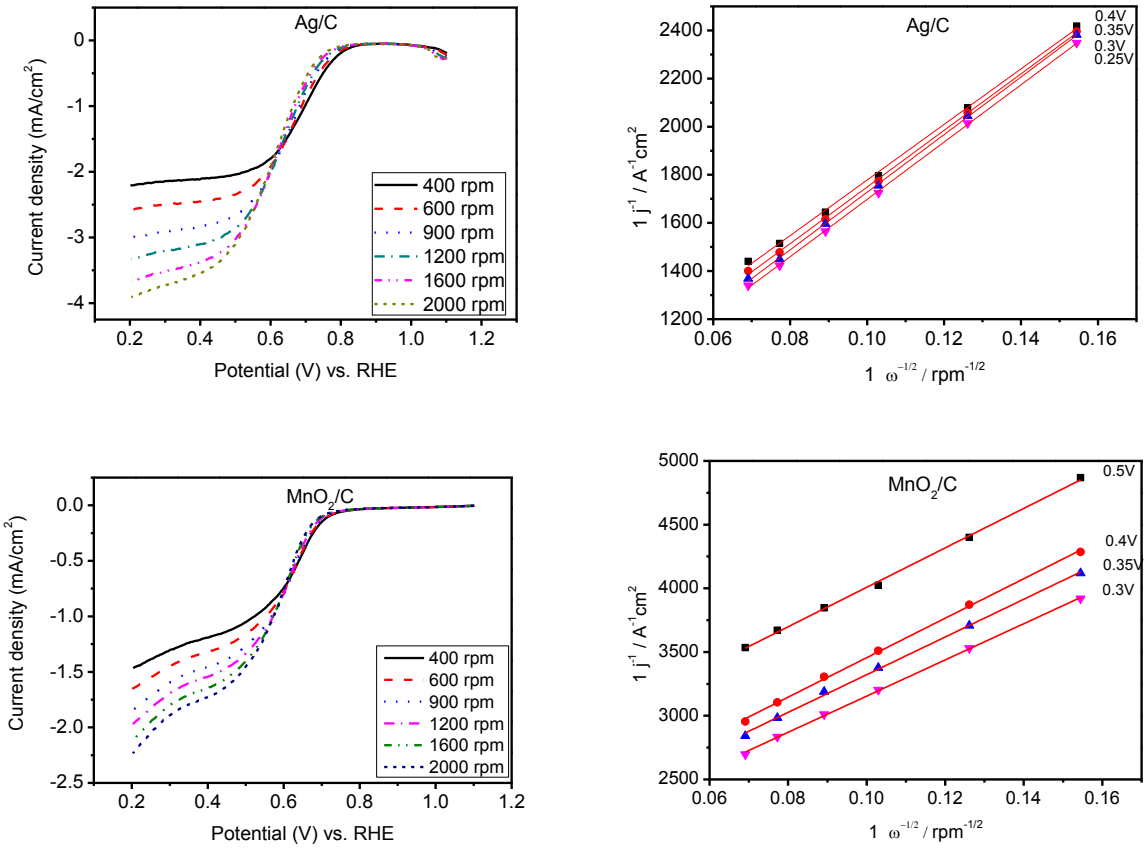

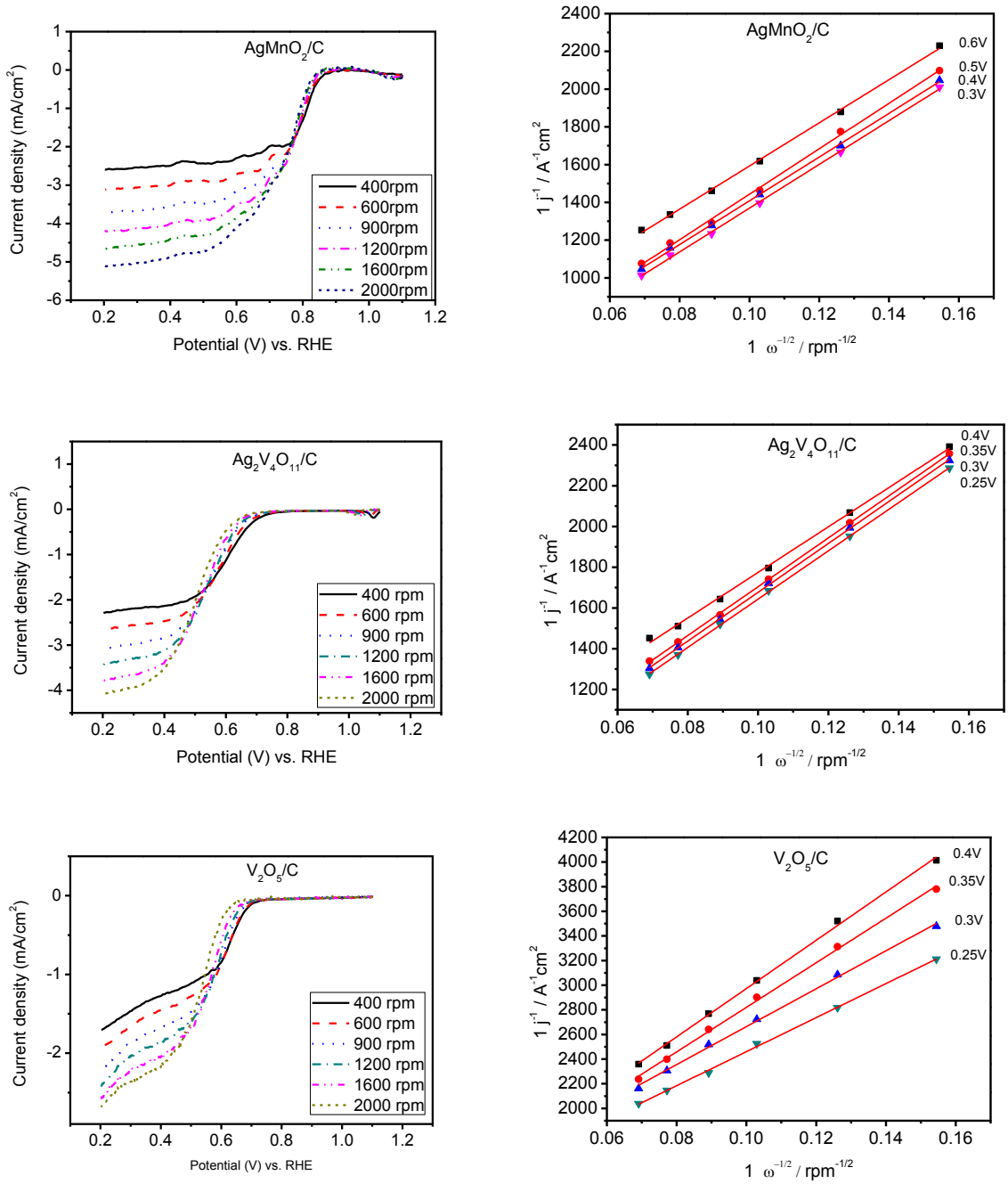

Fig. 11: Oxygen reduction reaction polarisation curves of Pt/C, Ag/C, MnO_2/C, $Ag_2V_4O_{11}$/C, V_2O_5/C and $AgMnO_2$/C catalysts on a rotating disk electrode in an O_2 saturated 0.1 M KOH at 40 °C with a sweep rate of 10 mV s^{-1}. Koutecky-Levich plots of Ag/C, MnO_2/C, $Ag_2V_4O_{11}$/C, V_2O_5/C and $AgMnO_2$/C at different potentials.

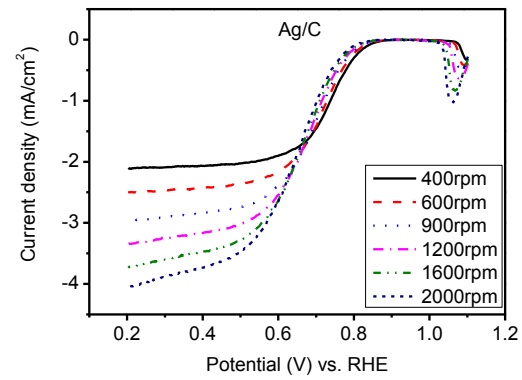
Ag/C
Current density (mA/cm^2)
Potential (V) vs. RHE
400rpm
600rpm
900rpm
1200rpm
1600rpm
2000rpm

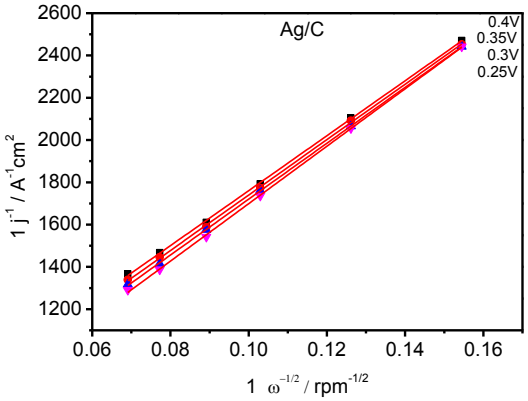
Ag/C
0.4V
0.35V
0.3V
0.25V
1 j^{-1} / A^{-1}cm^2
1 ω$^{-1/2}$ / rpm$^{-1/2}$

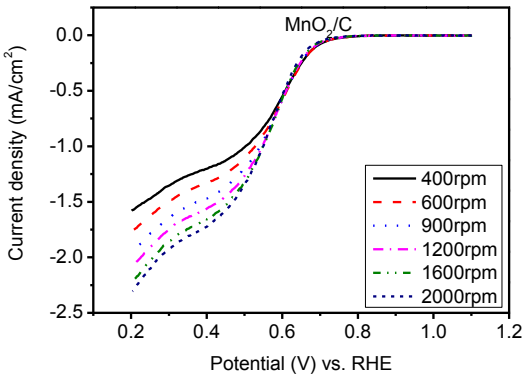
MnO$_2$/C
Current density (mA/cm^2)
Potential (V) vs. RHE
400rpm
600rpm
900rpm
1200rpm
1600rpm
2000rpm

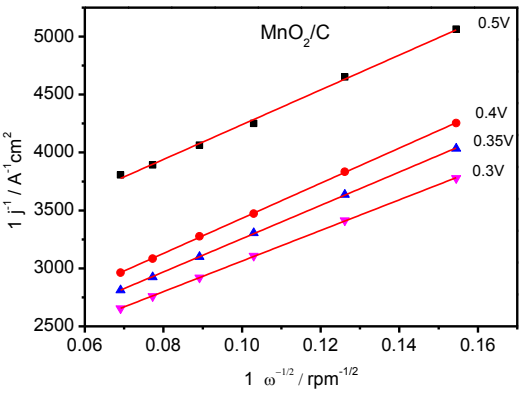
MnO$_2$/C
0.5V
0.4V
0.35V
0.3V
1 j^{-1} / A^{-1}cm^2
1 ω$^{-1/2}$ / rpm$^{-1/2}$

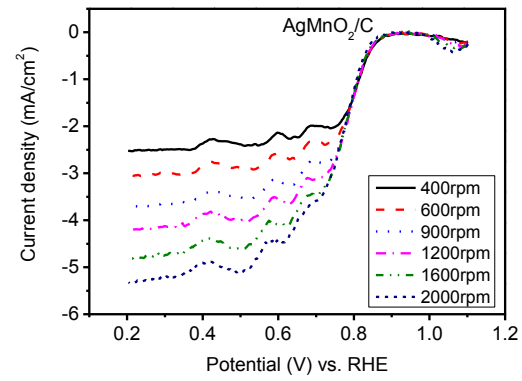
AgMnO$_2$/C
Current density (mA/cm^2)
Potential (V) vs. RHE
400rpm
600rpm
900rpm
1200rpm
1600rpm
2000rpm

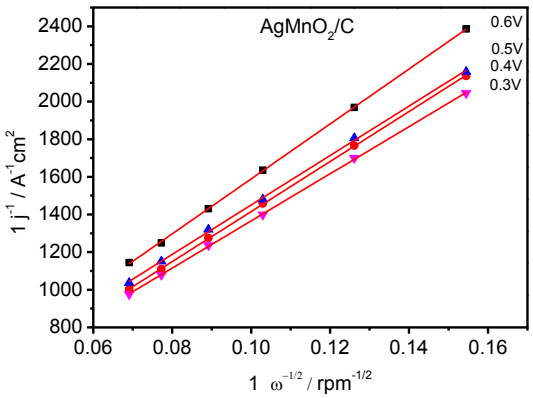
AgMnO$_2$/C
0.6V
0.5V
0.4V
0.3V
1 j^{-1} / A^{-1}cm^2
1 ω$^{-1/2}$ / rpm$^{-1/2}$

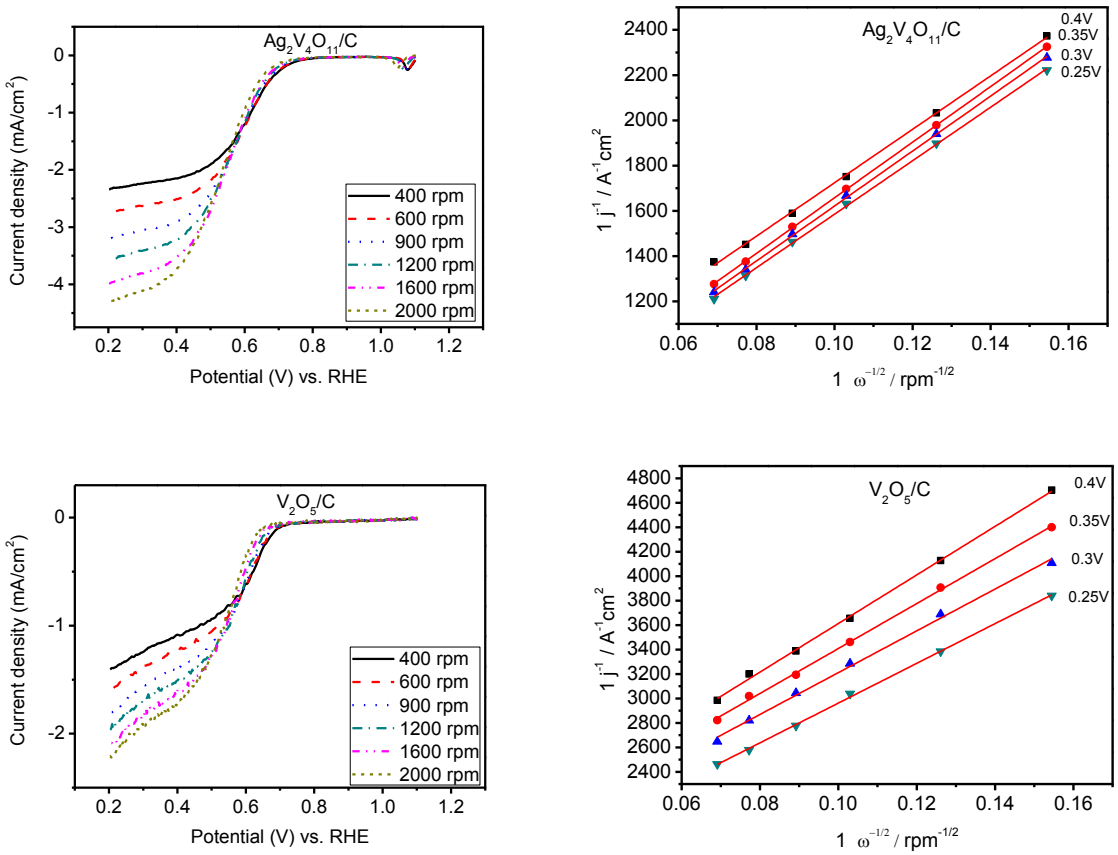

Fig. 12: Oxygen reduction reaction polarisation curves of Pt/C, Ag/C, MnO_2/C, $Ag_2V_4O_{11}$/C, V_2O_5/C and $AgMnO_2$/C catalysts on a rotating disk electrode in an O_2 saturated 0.1 M KOH at 50 °C with a sweep rate of 10 mV s^{-1}. Koutecky-Levich plots of Ag/C, MnO_2/C, $Ag_2V_4O_{11}$/C, V_2O_5/C and $AgMnO_2$/C at different potentials.

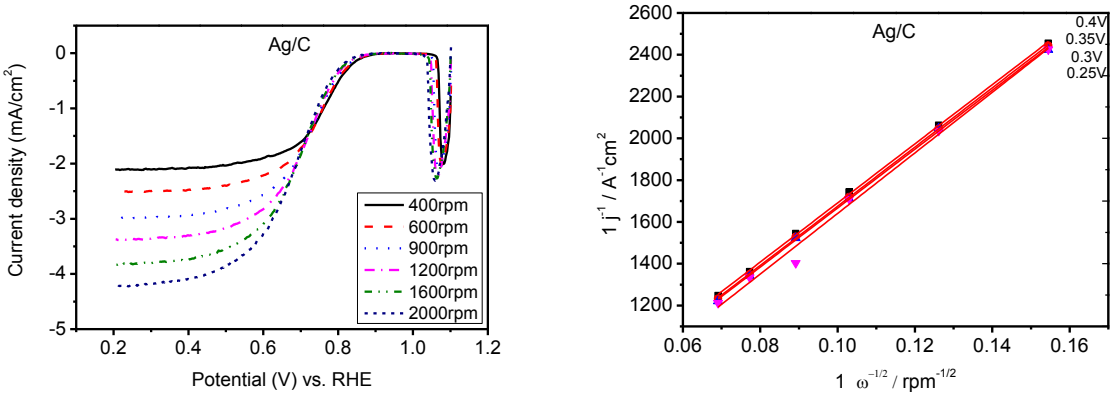

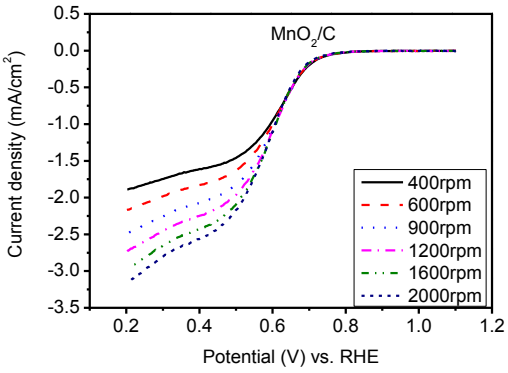
MnO2/C
Current density (mA/cm2)
Potential (V) vs. RHE
400rpm
600rpm
900rpm
1200rpm
1600rpm
2000rpm

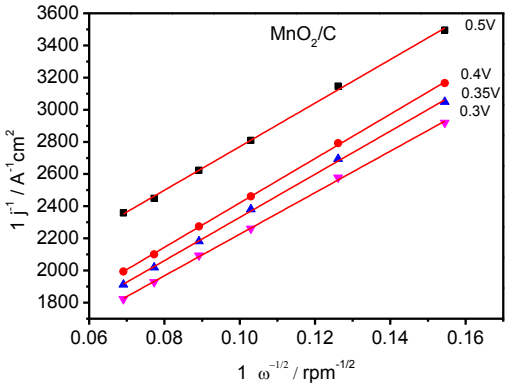
MnO2/C
0.5V
0.4V
0.35V
0.3V
1 j-1 / A-1cm2
1 ω-1/2 / rpm-1/2

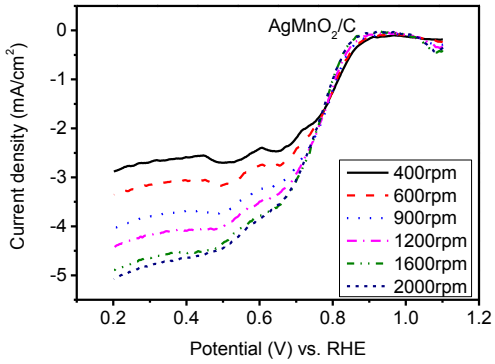
AgMnO2/C
Current density (mA/cm2)
Potential (V) vs. RHE
400rpm
600rpm
900rpm
1200rpm
1600rpm
2000rpm

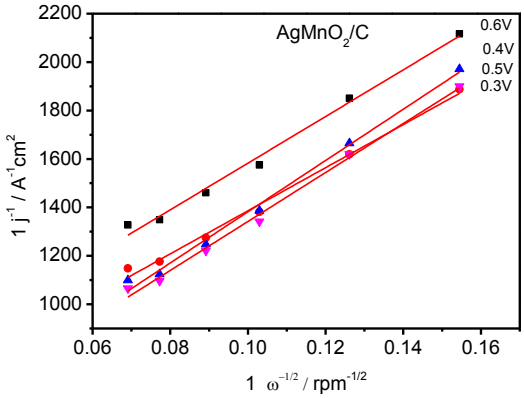
AgMnO2/C
0.6V
0.4V
0.5V
0.3V
1 j-1 / A-1cm2
1 ω-1/2 / rpm-1/2

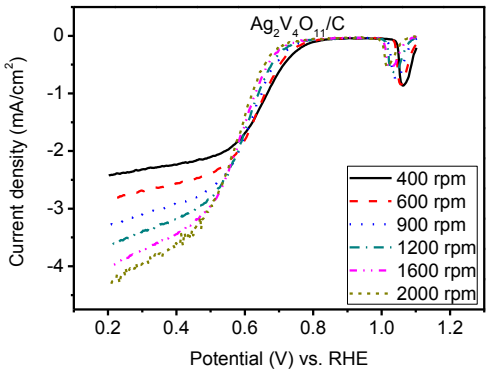
Ag2V4O11/C
Current density (mA/cm2)
Potential (V) vs. RHE
400 rpm
600 rpm
900 rpm
1200 rpm
1600 rpm
2000 rpm

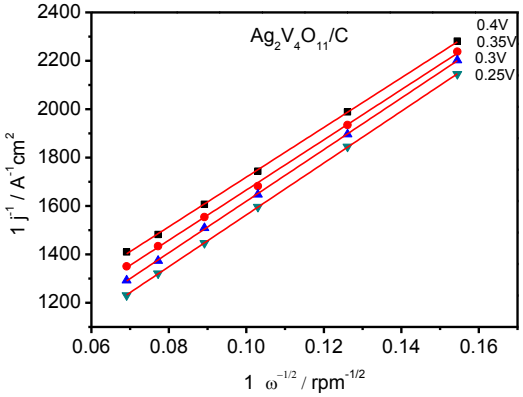
Ag2V4O11/C
0.4V
0.35V
0.3V
0.25V
1 j-1 / A-1cm2
1 ω-1/2 / rpm-1/2

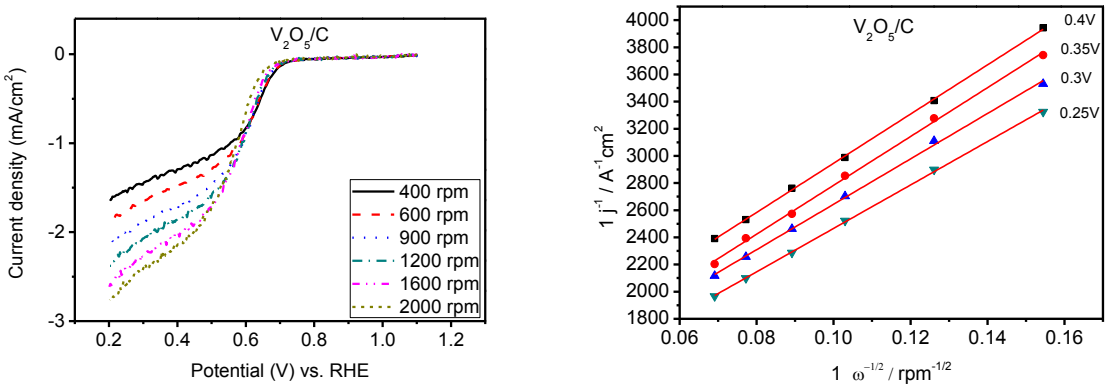

Fig. 13: Oxygen reduction reaction polarisation curves of Pt/C, Ag/C, MnO_2/C, $Ag_2V_4O_{11}$/C, V_2O_5/C and $AgMnO_2$/C catalysts on a rotating disk electrode in an O_2 saturated 0.1 M KOH at 60 °C with a sweep rate of 10 mV s^{-1}. Koutecky-Levich plots of Ag/C, MnO_2/C, $Ag_2V_4O_{11}$/C, V_2O_5/C and $AgMnO_2$/C at different potentials.

The oxygen reduction reaction (ORR) polarisation curves of Ag/C, MnO_2/C, $Ag_2V_4O_{11}$/C, V_2O_5/C and $AgMnO_2$/C electrocatalysts obtained mostly parallel curves (see Figs. 10-13). The Figures 10-13 (right) show Koutecky-Levich plots for different potentials on Ag/C, MnO_2/C and $AgMnO_2$/C electrocatalysts. The plots present linear dependence at whole potentials. The linearity and the parallelism of these curves are usually taken to imply first-order kinetics with respect to solubility of oxygen, which indicates that the current is diffusion-controlled (Meng *et al*., 2006). However, it is a pseudo 4-electron reduction pathway (2-electron reduction pathway or 4-electron reduction pathway) due to the formation of H_2O_2 on the surface of tested catalysts (Qiao *et al*., 2013, Meng *et al*., 2006). The ORR can be represented by the Koutecky-Levich equation (Meng *et al*., 2006) as:

$$i^{-1} = i_k^{-1} + i_l^{-1} \qquad (6)$$

$$i_l = 0.62nFAC_O{D_O}^{2/3}\nu^{-1/6}\,\omega^{1/2} \qquad (7)$$

where i_l is the diffusion limiting current, n is the number of electrons transfer in the reduction of oxygen, F is Faraday's constant (96,485 C mol^{-1}), A is the geometric surface area of RDE (A = 0.196 cm^2), C_O is the bulk concentration of oxygen, D_O is the diffusion coefficient of the oxygen, ν is the kinematic viscosity of the working electrolyte and ω is the angular rotation rate of the

electrode (1600 rpm = 12.946 rad s^{-1}) at 30 °C, 40 °C, 50 °C and 60 °C (Koscher *et al*., 2004, Qiao *et al*., 2013). The value of ν is collected from Table 2 at different temperatures (289 K, 293 K, 298 K and 313 K) (Chatenet *et al*., 2009).

Table 2. Kinematic viscosities (ν) measured in various concentrations of NaOH solution (Chatenet *et al*., 2009)

[NaOH]*, M	ν, cm^2s^{-1}			
	16 °C	20 °C	25 °C	40 °C
10^{-1}	0.0132±0.0004	0.0118	0.0104±0.0003	0.0075±0.0002

* Approximation: [NaOH] = [KOH]

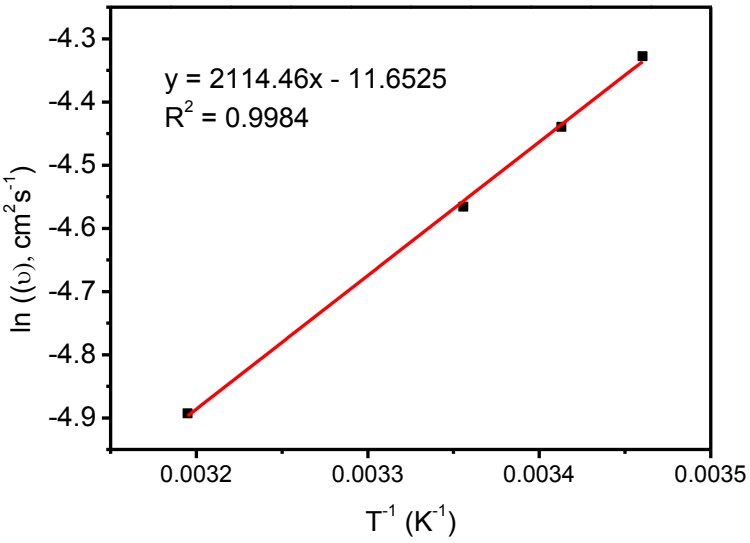

Fig. 14: Kinematic viscosity curve of 0.1 M KOH at various temperatures

The kinematic viscosity was calculated using the Arrhenius equation (Garcia *et al*., 2014):

$$\nu = A \exp \frac{B}{T} \qquad (8)$$

$$\ln \nu = \ln A - \frac{B}{T} \quad (9)$$

where ν is kinematic viscosities, A is a pre-exponential factor and B is the activation energy. The value of A is 8.719 x 10^{-6} cm^2 s^{-1} and B is 2114 K in 0.1 M KOH. The ν values are shown in Table 5. The approximate D_O was calculated from the oxygen diffusion in H_2O, shown in Table 3 at different temperatures (Garcia *et al*., 2014, Han *et al*., 1996).

Table 3. Value of oxygen diffusion (D_O) in H_2O^*(Han *et al*., 1996)

T, °C	D_O, 10^{-5} cm^2 s^{-1}
2.7	1.08
3.8	1.09
9.2	1.29
9.5	1.24
12.0	1.45
14.7	1.55
20.6	1.80
21.0	1.77
24.0	1.98
25.3	1.96
26.2	2.08
30.2	2.26
35.1	2.52
40.2	2.78
40.8	2.91

* Approximation: oxygen diffusion in H_2O = oxygen diffusion in KOH solution

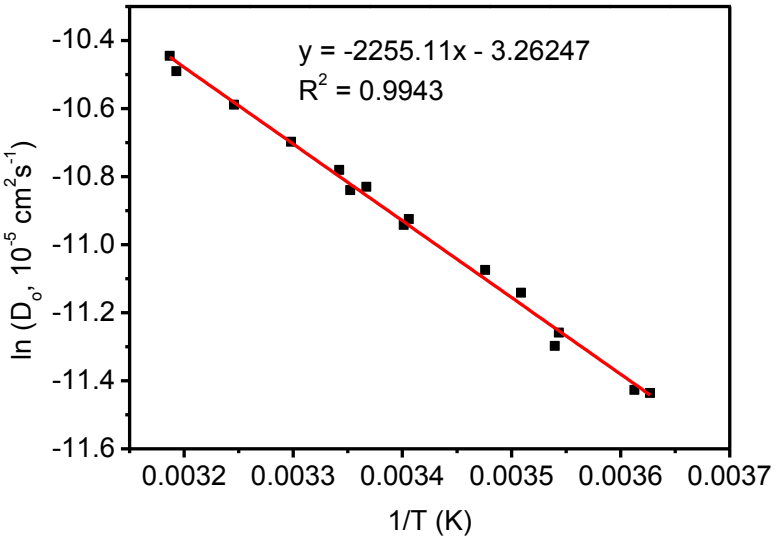

Fig. 15: Oxygen diffusion curve of 0.1 M KOH at various temperatures

The values were fitted to the curve with the Arrhenius equation (Eq. 9) (Garcia *et al*., 2014). The value of A is 3.831 x 10^{-2} cm^2 s^{-1} and B is -2255 K. The values of D_O in KOH solution at different temperatures are shown in Table 5. The value of C_O was determined from Table 4 at temperatures of 294 K, 318 K and 348 K (Allebrod, 2013).

Table 4. Value of oxygen solubility (C_O)

[KOH], M	C_O, 10^{-3} mol dm^{-3}		
	21 °C	45 °C	75 °C
0.1	1.26	0.94	0.77

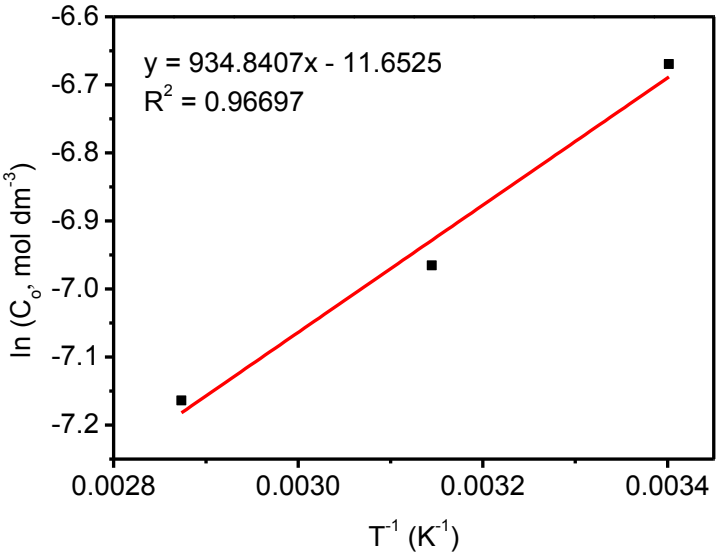

Fig. 16: Oxygen solubility curve of 0.1 M KOH at various temperatures

The values were determined from the curve with the Arrhenius equation (Eq. 9) (Garcia *et al*., 2014). The value of A is 5.18 x 10^{-5} mol dm^{-3} and B is 934.8 K in 0.1 M KOH. The C_O values are shown in Table 5.

Table 5. Value of oxygen solubility (C_O), value of oxygen diffusion (D_O) and kinematic viscosity (ν) at temperatures of 30 °C, 40 °C, 50 °C and 60 °C in 0.1 M KOH

T, °C	C_O, mol cm^{-3}	D_O, cm^2 s^{-1}	ν, cm^2 s^{-1}
30	1.13 x 10^{-6}	2.24 x 10^{-5}	0.0093
40	1.03 x 10^{-6}	2.85 x 10^{-5}	0.0074
50	9.36 x 10^{-7}	3.56 x 10^{-5}	0.0060
60	8.58 x 10^{-7}	4.39 x 10^{-5}	0.0049

The number of electrons transfer with different electrocatalysts at a potential of 0.3 V was determined by the Koutecky-Levich equation (Table 6). The kinetic current i_k can be obtained directly from y-axis intercept of Koutecky-Levich plots (see Table 7 and Figs. 10-13).

Table 6. Comparison of the total number of electrons transfer (n) with different electrocatalysts at different temperatures determined by RDE at potential of 0.3 V, a rotation rate of 1600 rpm, in 0.1 M KOH

Temperature, °C	n @ 0.3 V					
	Ag/C	MnO_2/C	$AgMnO_2$/C	$Ag_2V_4O_{11}$/C	V_2O_5/C	Pt/C
30	3.37	3.00	3.81	3.63	3.37	3.70
40	3.28	2.76	3.38	3.28	2.55	3.00
50	2.71	2.71	2.86	2.95	2.10	2.59
60	2.33	2.54	2.25	3.08	1.97	2.25

Table 7. Comparison of kinetic current activities (i_k) of all electrocatalysts at different temperatures determined by y-axis intercept of Koutecky-Levich plots at a potential of 0.3 V and a rotation rate of 1600 rpm in 0.1 M KOH

Temperature, °C	i_k, A/cm^2					
	Ag/C	MnO_2/C	$AgMnO_2$/C	$Ag_2V_4O_{11}$/C	V_2O_5/C	Pt/C
30	0.0052	0.00062	0.0037	0.0038	0.00057	0.021
40	0.0019	0.00057	0.0048	0.0021	0.00088	0.066
50	0.0025	0.00057	0.0088	0.0025	0.00066	0.035
60	0.0039	0.00011	0.0030	0.0018	0.00100	0.062

The Koutecky-Levich curves exhibit good linear fit for each potential of Ag/C, MnO_2/C, $Ag_2V_4O_{11}$/C, V_2O_5/C and $AgMnO_2$/C electrocatalyst (see Figs. 10-13). The number of transferred electron for $AgMnO_2$/C and Pt/C are approximately 4 in 0.1 M KOH at 30 °C. The kinetic current activity result of the Pt/C shows high values (see Table 7). The value for oxygen solubility (C_O) is reduced at higher temperatures than 30 °C (see Table 5). Oxygen solubility

(C_O) depends on the temperature. It can be explained as in the equation follows (Xing *et al*., 2014).

$$C_O = \frac{55.56\, P_{O_2}}{\exp(3.71814 + \frac{5596.17}{T} - \frac{1049668}{T^2} - P_{O_2})} \qquad (10)$$

where P_{O2} is the partial pressure above the solution (atm) and T is the absolute temperature (K).

The kinematic viscosity (υ) is decreased (see Table 5), in which the value for oxygen diffusion (D_O) is increased at higher temperatures than 30 °C (see Table 5). Oxygen diffusion (D_O) in the electrolyte can be described by the Stoke-Einstein equation (Xing *et al*., 2014):

$$D_{O_2} = \frac{kT}{6\pi r\eta} \qquad (11)$$

where k is the Boltzmann constant (kg cm^2/s^2), T is the absolute temperature (K), η is the dynamic viscosity of the solution (kg/cm^2) and r is the radius of the O_2 molecule (cm^2).

4.4.2.5 Electrocatalytic activity of Pt/C, Ag/C, MnO_2/C, $Ag_2V_4O_{11}$/C, V_2O_5/C and $AgMnO_2$/C electrocatalysts towards oxygen reduction in 0.1 M KOH with different ethanol concentrations.

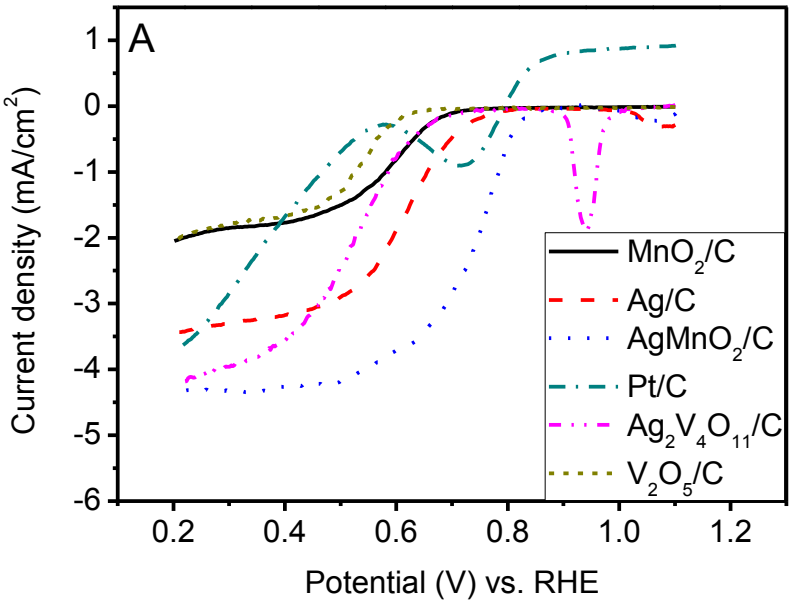

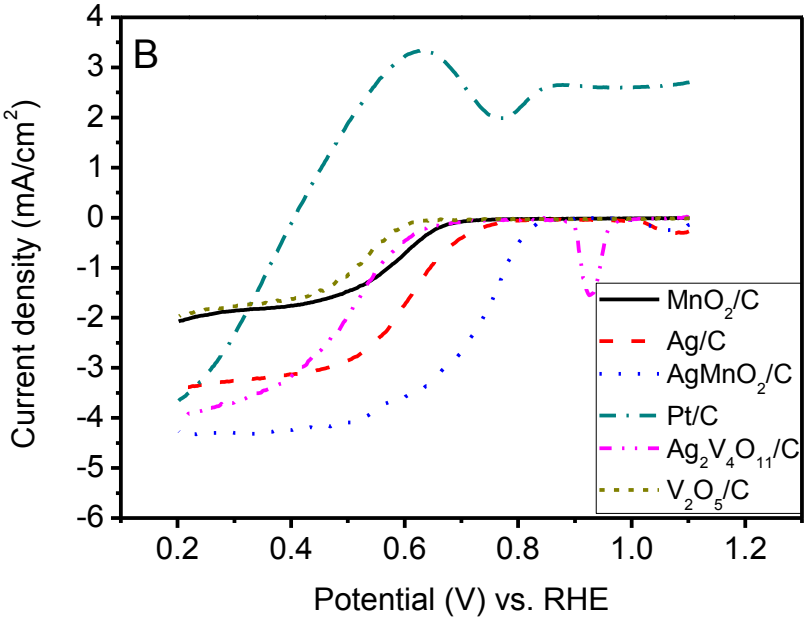

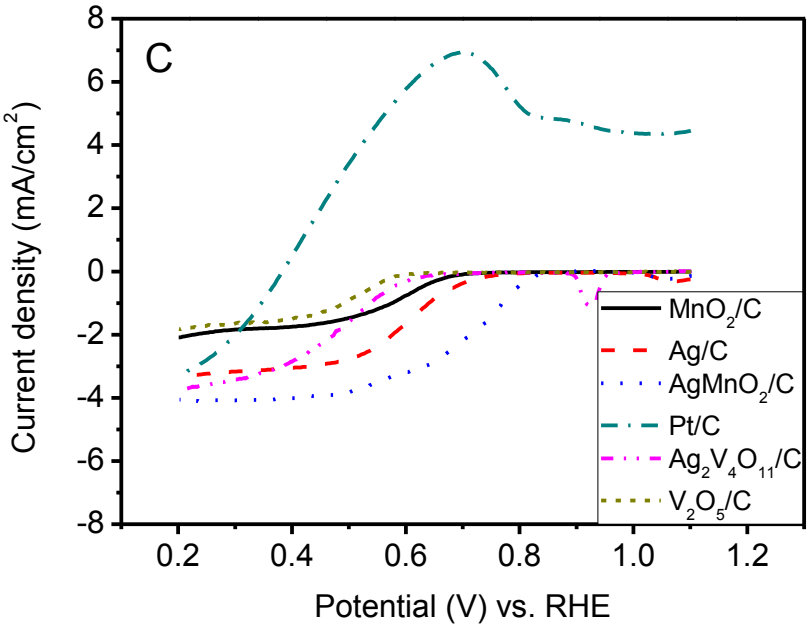

Fig. 17: Linear potential scan curves of Pt/C, Ag/C, MnO_2/C, $Ag_2V_4O_{11}$/C, V_2O_5/C and $AgMnO_2$/C catalysts on a rotating disk electrode in O_2 saturated alkaline containing ethanol electrolytes: **(A)** 0.1 M KOH with 0.1 M EtOH **(B)** 0.1 M KOH with 0.5 M EtOH and **(C)** 0.1 M KOH with 1.0 M EtOH at 30 °C, at a sweep rate of 10 mV s^{-1} and a rotation rate of 1600 rpm.

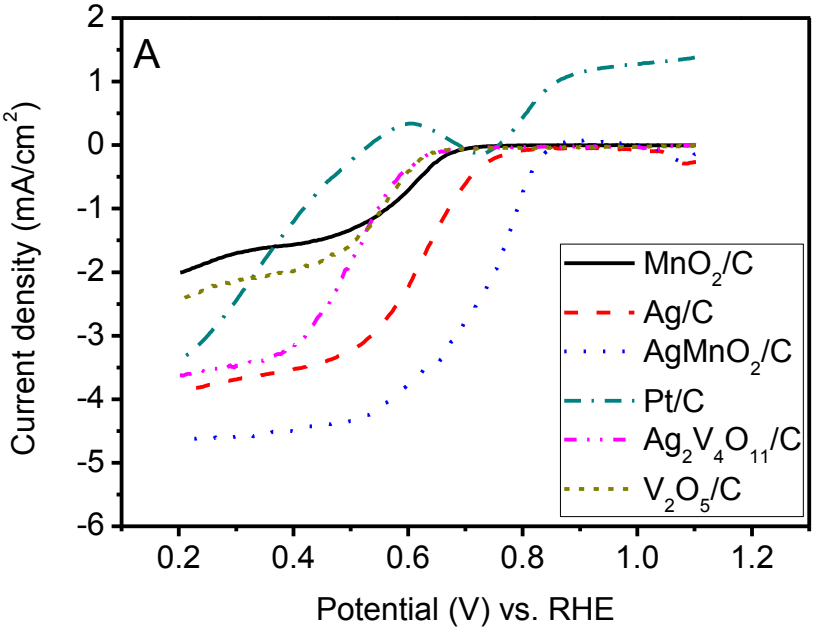

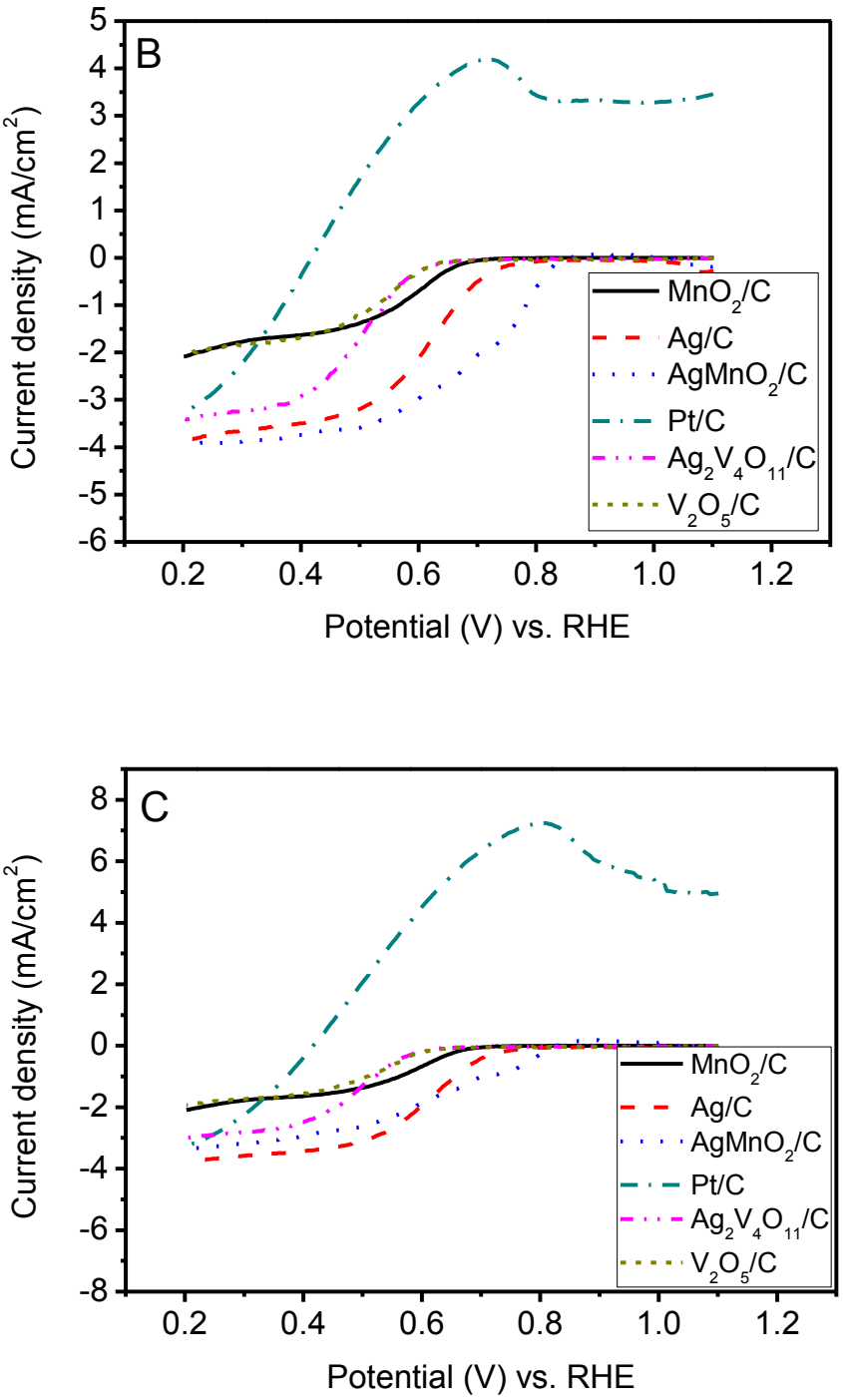

Fig. 18: Linear potential scan curves of Pt/C, Ag/C, MnO_2/C, $Ag_2V_4O_{11}$/C, V_2O_5/C and $AgMnO_2$/C catalysts on a rotating disk electrode in O_2 saturated alkaline containing ethanol electrolytes: **(A)** 0.1 M KOH with 0.1 M EtOH **(B)** 0.1 M KOH with 0.5 M EtOH and **(C)** 0.1 M KOH with 1.0 M EtOH at 40 °C, at a sweep rate of 10 mV s^{-1} and a rotation rate of 1600 rpm.

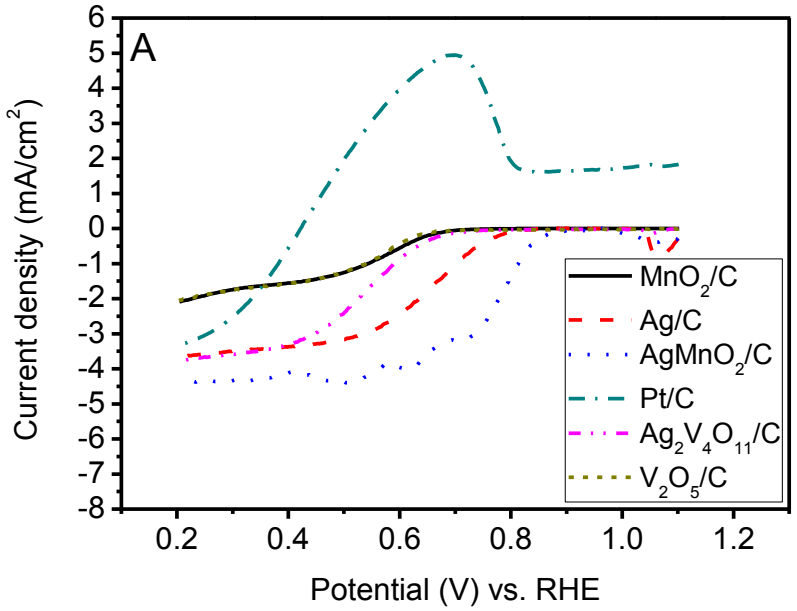
A
Current density (mA/cm^2)
Potential (V) vs. RHE
MnO_2/C
Ag/C
$AgMnO_2$/C
Pt/C
$Ag_2V_4O_{11}$/C
V_2O_5/C

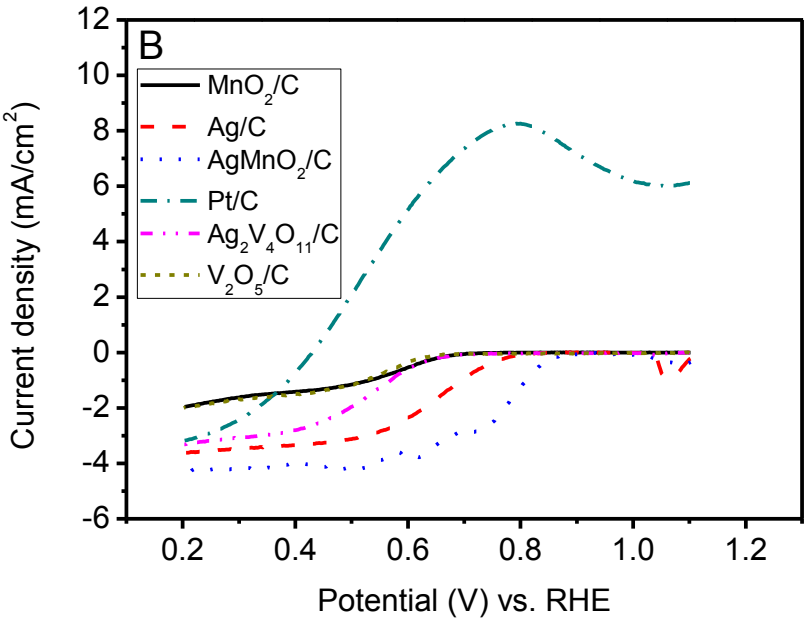
B
Current density (mA/cm^2)
Potential (V) vs. RHE
MnO_2/C
Ag/C
$AgMnO_2$/C
Pt/C
$Ag_2V_4O_{11}$/C
V_2O_5/C

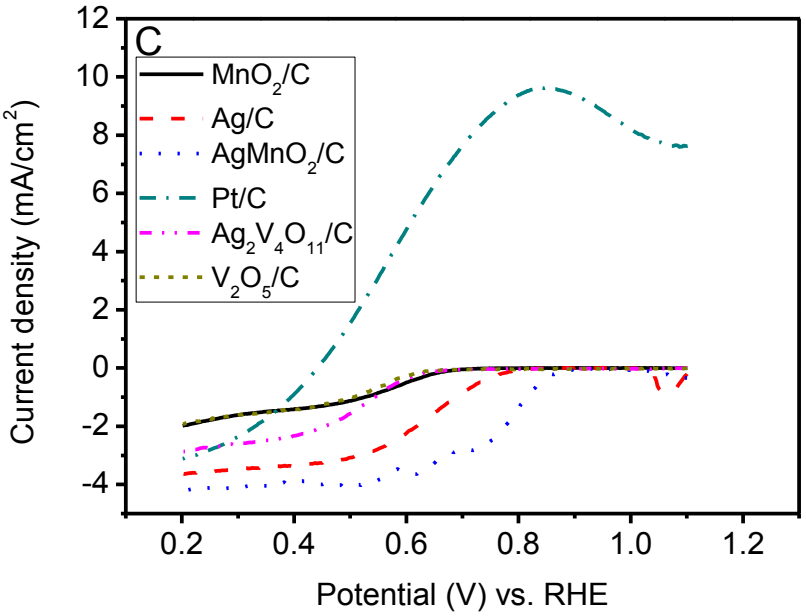

Fig. 19: Linear potential scan curves of Pt/C, Ag/C, MnO_2/C, $Ag_2V_4O_{11}$/C, V_2O_5/C and $AgMnO_2$/C catalysts on a rotating disk electrode in O_2 saturated alkaline containing ethanol electrolytes: **(A)** 0.1 M KOH with 0.1 M EtOH **(B)** 0.1 M KOH with 0.5 M EtOH and **(C)** 0.1 M KOH with 1.0 M EtOH at 50 °C, at a sweep rate of 10 mV s^{-1} and a rotation rate of 1600 rpm.

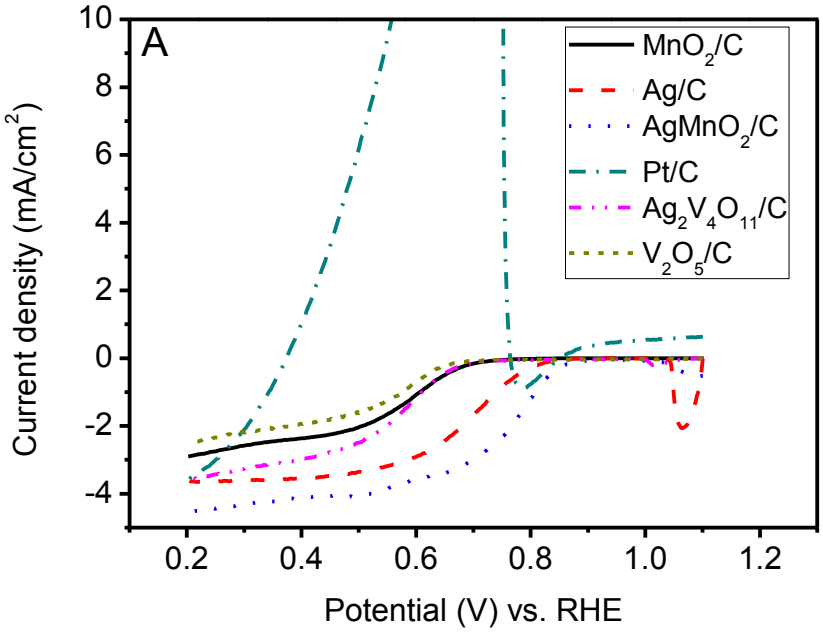

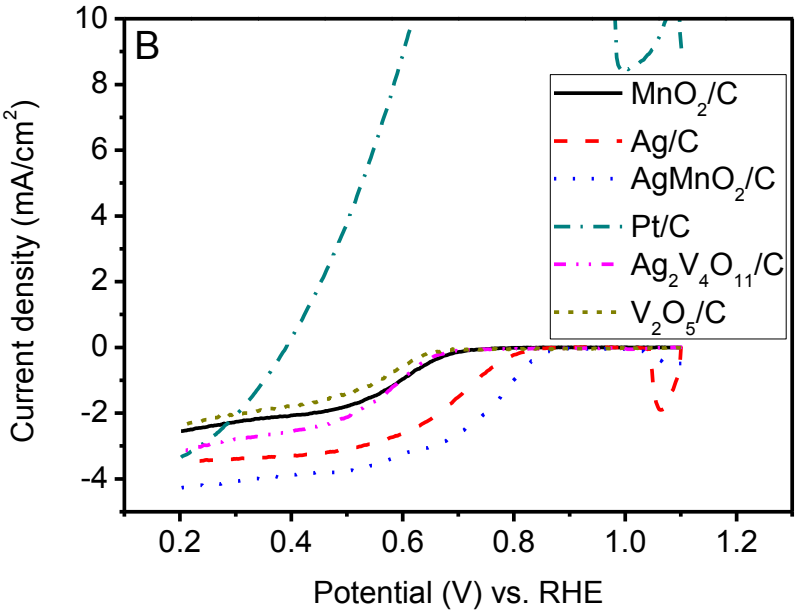

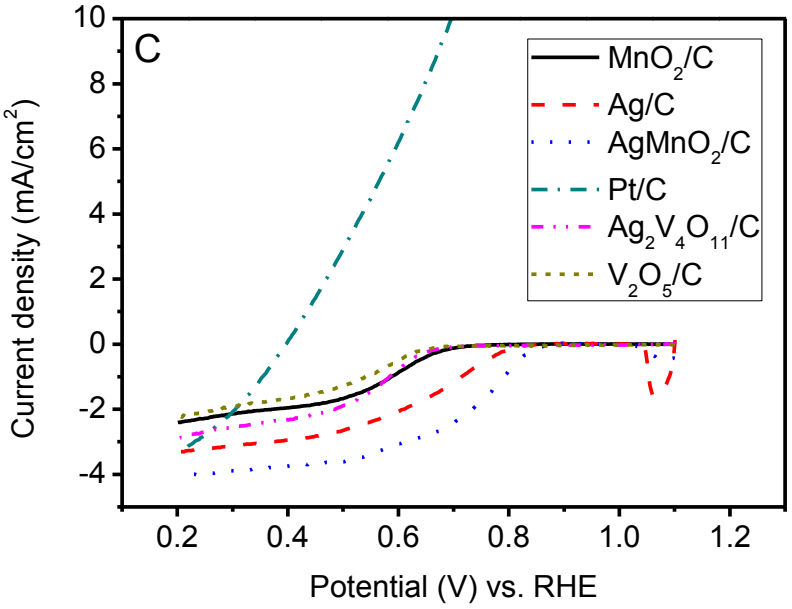

Fig. 20: Linear potential scan curves for Pt/C, Ag/C, MnO_2/C, $Ag_2V_4O_{11}$/C, V_2O_5/C and $AgMnO_2$/C catalysts on a rotating disk electrode in O_2 saturated alkaline containing ethanol electrolytes: **(A)** 0.1 M KOH with 0.1 M EtOH **(B)** 0.1 M KOH with 0.5 M EtOH and **(C)** 0.1 M KOH with 1.0 M EtOH at 60 °C at a sweep rate of 10 mV s^{-1} and a rotation rate of 1600 rpm.

The linear potential scan curves of the Pt/C electrocatalysts showed ethanol oxidation at various temperatures and different alkaline electrolyte concentrations (see Figs 17-20). The proposed ethanol electro-oxidation mechanism in alkaline medium can be written as follows for platinum electrocatalysts (Suib, 2013).

$$Pt + OH^- \rightarrow Pt\text{-}OH_{ads} + e^- \quad (12)$$

$$Pt + CH_3CH_2OH \rightarrow Pt\text{-}[CH_3CH_2OH]_{ads} \quad (13)$$

$$Pt\text{-}[CH_3CH_2OH]_{ads} + 3OH^- \rightarrow Pt\text{-}[CH_2CO]_{ads} + 3H_2O + 3e^- \quad (14)$$

$$Pt\text{-}[CH_2CO]_{ads} + Pt\text{-}OH_{ads} \rightarrow Pt\text{-}CH_3COOH + Pt \quad (15)$$

$$Pt\text{-}CH_3COOH + OH^- \rightarrow Pt + CH_3COO^- + H_2O \quad (16)$$

The rate determining step is step (15). The ethoxy ion intermediates of produced acetate via adsorption of hydroxyl ions (OH^-) (Suib, 2013). Ag/C, Mn_3O_4/C, $Ag_2V_4O_{11}$/C, V_2O_5/C and $AgMn_3O_4$/C electrocatalysts are ethanol-tolerant. According to the results, the $AgMnO_2$/C electrocatalysts shows significant enhancement of ORR activity (see Figs. 17-20).

4.4.2.6 Tafel plots of Pt/C, Ag/C, MnO_2/C, $Ag_2V_4O_{11}$/C, V_2O_5/C and $AgMnO_2$/C electrocatalysts in 0.1 M KOH.

Tafel plots exhibit a linear correlation of the potential (E) and the log i_k. The kinetic current i_k can be calculated by Equation 17.

$$i_k = \frac{(i_d x i_o)}{(i_d - i_o)} \quad (17)$$

where i_o is the observed current and i_d is the limiting current that can be obtained directly from the ORR polarisation curve (see Figs. 10-13).

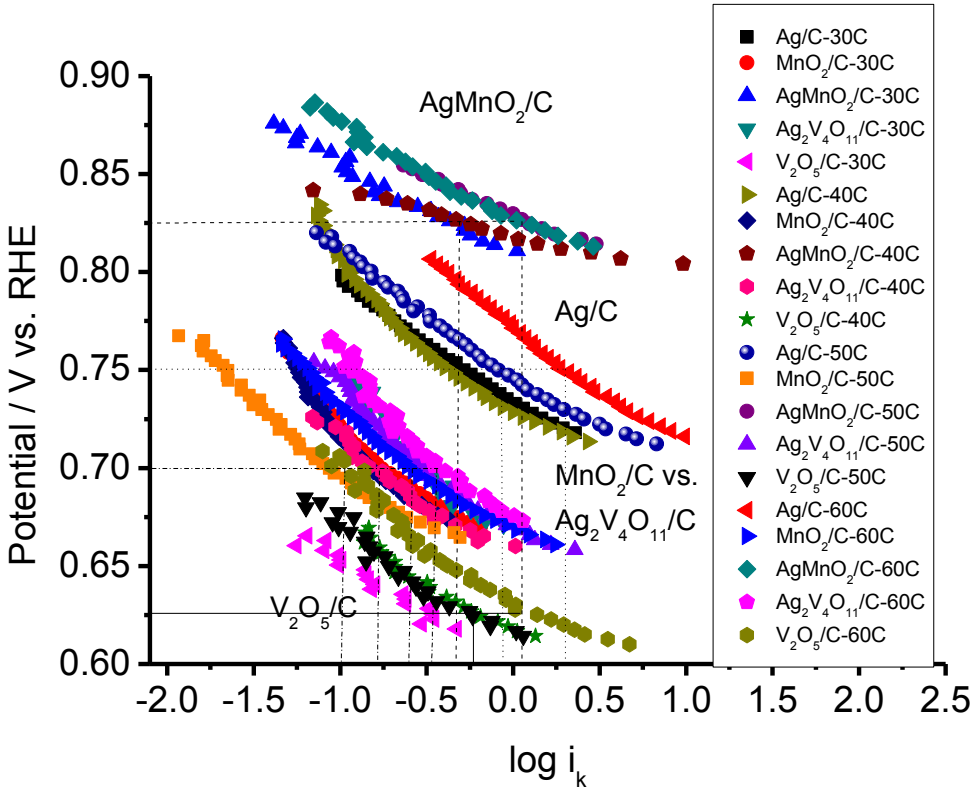

Fig. 21: Tafel plots of oxygen reduction for Ag/C, MnO_2/C, $Ag_2V_4O_{11}$/C, V_2O_5/C and $AgMnO_2$/C electrocatalysts in 0.1 M KOH at temperatures of 30 °C, 40 °C, 50 °C, and 60 °C

The performance of the electrocatalysts was evaluated from the kinetic current density (i_k), as seen in Figure 21. All electrocatalysts display at 60 °C higher mass activity than at 30 °C. The average Tafel slope of $AgMnO_2$/C, Ag/C, MnO_2/C $Ag_2V_4O_{11}$/C and V_2O_5/C are 39.17 mV dec^{-1}, 62.97 mV dec^{-1}, 81.69 mV dec^{-1}, 80.53 mV dec^{-1} and 59.45 mV dec^{-1}, respectively

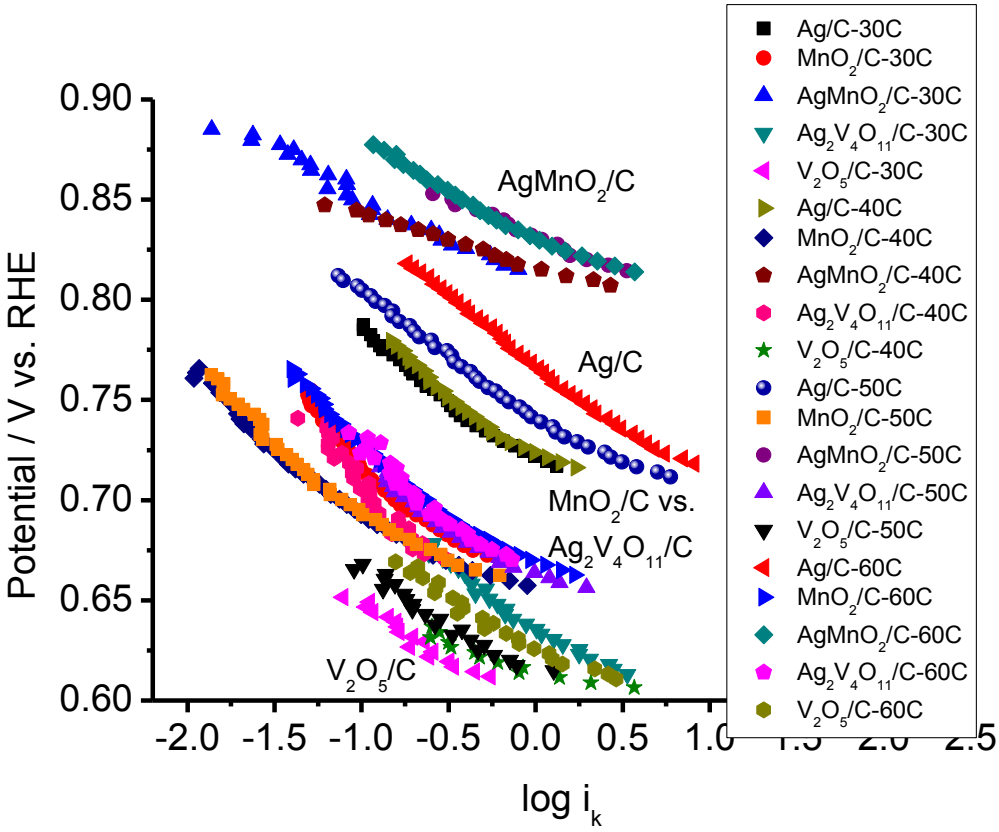

Fig. 22. Tafel plots of oxygen reduction for Ag/C, MnO_2/C, $AgMnO_2$/C, $Ag_2V_4O_{11}$/C and V_2O_5/C electrocatalysts in 0.1 M KOH with 0.1 M EtOH at temperatures of 30 °C, 40 °C, 50 °C, and 60 °C

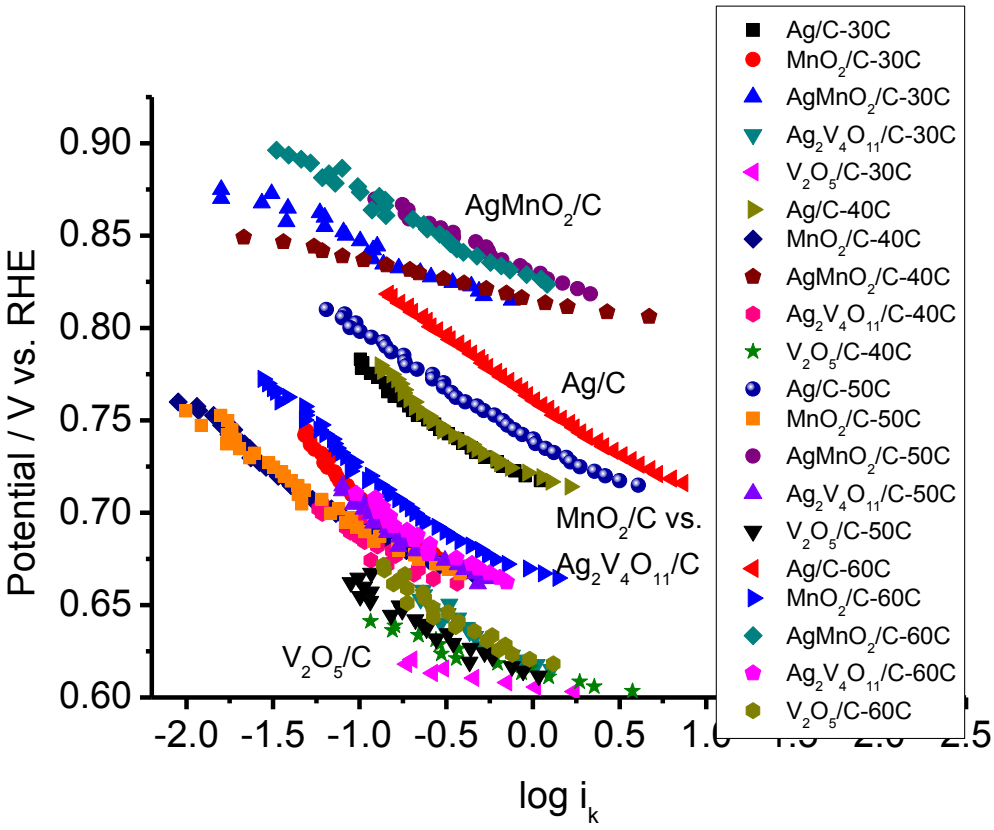

Fig. 23. Tafel plots of oxygen reduction for Ag/C, MnO_2/C, $AgMnO_2$/C, $Ag_2V_4O_{11}$/C and V_2O_5/C electrocatalysts in 0.1 M KOH with 0.5 M EtOH at temperatures of 30 °C, 40 °C, 50 °C, and 60 °C

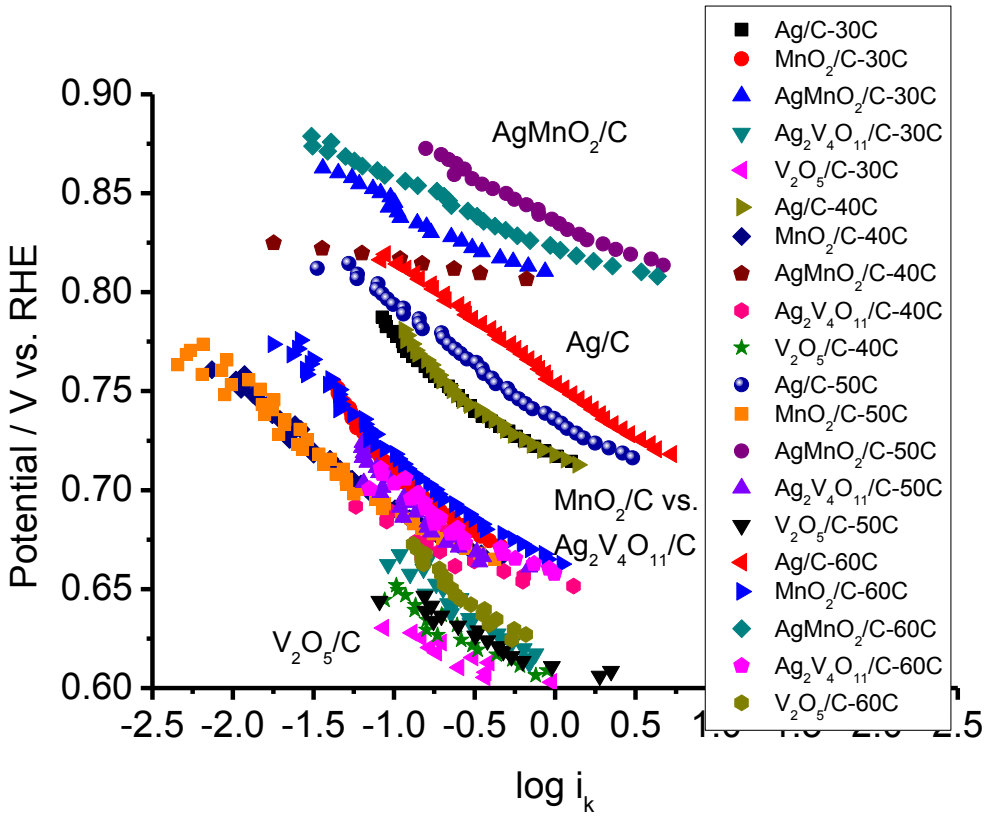

Fig. 24. Tafel plots of oxygen reduction for Ag/C, MnO_2/C, $AgMnO_2$/C, $Ag_2V_4O_{11}$/C and V_2O_5/C electrocatalysts in 0.1 M KOH with 1.0 M EtOH at temperatures of 30 °C, 40 °C, 50 °C, and 60 °C

Table 8. Tafel slope of oxygen reduction for Ag/C, MnO_2/C, $Ag_2V_4O_{11}$/C, V_2O_5/C and $AgMnO_2$/C electrocatalysts in 0.1 M KOH with various ethanol concentration at temperatures of 30 °C, 40 °C, 50 °C, and 60 °C

	Tafel slope (mV dec^{-1})			
Ag/C	30˚C	40˚C	50˚C	60˚C
0.1MKOH+0.1MEtOH	65.45	64.56	57.54	65.10
0.1MKOH+0.5MEtOH	65.23	64.72	57.14	63.53
0.1MKOH+1.0MEtOH	64.89	64.94	57.01	59.63
Average Tafel slope	65.19	64.74	57.23	62.75
$AgMnO_2$/C	30˚C	40˚C	50˚C	60˚C
0.1MKOH+0.1MEtOH	45.89	26.14	36.98	45.09

0.1MKOH+0.5MEtOH	40.54	20.38	43.23	49.53
0.1MKOH+1.0MEtOH	42.05	20.22	41.63	34.36
Average Tafel slope	42.82	22.24	40.61	42.99
MnO_2/C	30˚C	40˚C	50˚C	60˚C
0.1MKOH+0.1MEtOH	80.78	61.96	66.18	68.45
0.1MKOH+0.5MEtOH	82.24	61.16	61.54	70.67
0.1MKOH+1.0MEtOH	83.13	60.13	61.35	70.17
Average Tafel slope	82.05	61.08	63.02	69.76
$Ag_2V_4O_{11}$/C	30˚C	40˚C	50˚C	60˚C
0.1MKOH+0.1MEtOH	58.62	97.31	54.71	73.88
0.1MKOH+0.5MEtOH	61.84	63.46	62.18	57.90
0.1MKOH+1.0MEtOH	65.38	50.61	77.45	49.91
Average Tafel slope	61.95	70.46	64.78	60.56
V_2O_5/C	30˚C	40˚C	50˚C	60˚C
0.1MKOH+0.1MEtOH	56.15	44.26	54.58	49.53
0.1MKOH+0.5MEtOH	58.09	43.73	53.29	59.12
0.1MKOH+1.0MEtOH	43.57	48.07	41.46	71.74
Average Tafel slope	52.60	45.35	49.78	60.13

As shown in Figures 22-24, the performance of the electrocatalysts in electrolytes with different ethanol-concentrations in 0.1 M KOH was evaluated from the kinetic current density (i_k). Most of electrocatalysts display higher mass activity at 60 °C than at 30 °C. The values of Tafel slopes of $AgMnO_2$/C, Ag/C, $Ag_2V_4O_{11}$/C, V_2O_5/C and MnO_2/C at different temperatures and electrolytes are shown in Table 8.

4.5 Summary and conclusion

The Ag, V and Mn metal (TEM image) were displayed as dark spherical particles. According to the base cyclic voltammograms of Ag/C and $AgMnO_2$/C catalysts, the oxidation peak of Ag_2O was shown as well as the peaks for AgOH and Ag_2O were found. Moreover, the Ag oxidation appeared at a potential of 1.3 V-1.4 V. At potentials of 0.7 V and 0.8 V, the cyclic voltammograms of MnO_2/C and $AgMnO_2$/C catalyst in KOH indicates the peak of $Mn(OH)_2$,

which changed into Mn_2O_3 and MnOOH. Additionally, the oxidation peak was obtained at approximately 1.0 V that indicated the oxidation of MnOOH to MnO_2, while the cyclic votammograms of $AgMnO_2$/C eletrocatalysts show an overlap of oxidation peaks for both Ag and MnO_2. Nevertheless, the reduction peak of $AgMnO_2$ was higher than those of Ag with saturated N_2 and O_2. The cyclic voltammograms in the presence of O_2, a large reduction peak of the $AgMnO_2$/C is also shown at a potential of 0.2-0.8 V in 0.1 M KOH. According to the results, the $AgMnO_2$/C electrocatalysts are deemed helpful in improving the ORR activity. In addition, the performance of the $AgMnO_2$/C electrocatalyst is compared with the Pt/C electrocatalyst and they had similar activity in both alkaline electrolytes at 30 °C. The CV of the Ag/C catalyst also shows high current density for the Ag_2O-Ag peaks at 60 °C. The current density of reduction peak of $AgMnO_2$/C is increased at 60 °C compared to at 30 °C.

Ethanol oxidation is observed for Pt/C electrocatalysts, while Ag/C, MnO_2/C, $Ag_2V_4O_{11}$/C, V_2O_5/C and $AgMnO_2$/C show high ethanol-tolerance. All electrocatalysts thus prevented an ethanol oxidation reaction from ethanol crossover at the cathode side in alkaline direct ethanol fuel cells. The Koutecky-Levich curves exhibited good linear fits for each potential of Ag/C, MnO_2/C, $Ag_2V_4O_{11}$/C, V_2O_5/C and $AgMnO_2$/C electrocatalysts. The number of electron transfer (n) is *ca*. 4 in 0.1 M KOH for $AgMnO_2$/C and Pt/C at 30 °C, while the kinematic viscosity (υ) and the value for oxygen solubility (C_O) are reduced at 60 °C. However, the value of oxygen diffusion (D_O) is increased at temperatures higher than 30 °C. Kinetic current density (i_k) is used to assess the performance of these electrocatalysts, and both with and without various the concentrations of ethanol. Almost all electrocatalysts show higher mass activity at 60 °C than at 30 °C. During all investigations, the $AgMnO_2$/C electrocatalyst showed the highest performance for ORR in the presence of ethanol due to its superior tolerance toward ethanol poisoning, thus making it a promising cathode catalyst for ADEFCs.

5. Conclusions and outlook

Fuel cells have been designed for the continuous conversion of different kinds of fuel to electrical energy. Various gaseous and liquid fuels are applied in fuel cells. A benefit of fuel cells is their ability to operate with little or no noise. The cathode, anode and membrane comprise the core components of a fuel cell to realize the electrochemical oxidation at the anode and the corresponding reduction at the cathode. Electrochemical reactions in the fuel cell convert fuel and oxygen directly into electricity and heat. Reaction products are water or steam and in case of hydrocarbon fuel, carbon dioxide.

Excessive heat can be expelled from the fuel cell efficiently with liquid coolants due to their heat transfer coefficients in the range of 500-1000 W m^{-2} K^{-1} compared to the heat transfer coefficient of air of approx. 15-30 W m^{-2} K^{-1}. The influence of coolant leakage into the cell was the main focus of the investigations.

Ethylene glycol (EG) is a widely used coolant due to its optimal properties concerning toxicity, costs, freezing and boiling point as well as viscosity. However, because of the adsorption of EG on the Pt catalyst surface, it may block active sites and as an intermediate reaction product during the oxidation of the molecule CO might be formed.

The investigation of the reaction kinetics including the oxygen adsorption at the catalytic sites of electrocatalysts for the oxygen reduction reaction (ORR) in case of coolant leakage was a main focus of research. Coolant leakage has a similar effect on molecular level like the fuel crossover of the liquid fuel in a direct ethanol cell. Ethanol crosses through the membrane from the anode to the cathode side and influences the cell potential directly. Ethanol adsorption on the surface of the electrocatalyst results, similar to EG, in limitation of adsorption in oxygen molecules on the surface of an electrocatalysts. The evaluation and the development of ethanol-tolerant cathode electrocatalysts (for utilization in alkaline direct ethanol fuel cells) were investigated.

According to the results for coolant leakage, the coolant consisting of ethylene glycol and Triton-X, reduced ethylene glycol electrooxidation at 0.5-0.9 V vs. RHE, cycle by cycle, compared to coolant consisting of ethylene glycol/water. Hence, Triton-X, a non-ionic surfactant, decreases the electrooxidation reaction of ethylene glycol. Initially, the EG molecules may be introduced into Triton-X micelles preventing CO formation and poisoning of the active sites. On the

electrode surfaces, the CO species, the EG molecules and the Triton-X compete for adsorption on the Pt electrocatalyst. Therefore, the CO may create oxidation reaction on the surface of the Pt electrocatalyst. Coolant such as ethylene glycol / Triton-X shows obstruction of CO poisoning on the Pt electrocatalyst. Furthermore, the results of the coolant ethylene glycol / Triton-X show the loss of Pt ECSA after coolant contamination as changing new electrolyte and during contamination as presence the coolant into the electrolyte of 0.02% and 37.74%, respectively. ORR during contamination with ethylene glycol only shows ethylene glycol oxidation at potentials of 0.5-0.9 V. On the other hand, ORR during contamination with coolant consisting of ethylene glycol / Triton-X demonstrates that Triton-X reduces ethylene glycol electrooxidation.

According to the results for ethanol crossover, Ag/C, MnO_2/C, $Ag_2V_4O_{11}$/C, V_2O_5/C and $AgMnO_2$/C exhibited ethanol-tolerance during oxygen reduction reaction. Therefore, all electrocatalysts prevent ethanol oxidation reaction from ethanol crossover at the cathode side in alkaline direct ethanol fuel cells. Most of the ORR results confirm that $AgMnO_2$/C electrocatalysts significantly improve the cathode performance. In addition, the performance of $AgMnO_2$/C electrocatalysts was compared to state-of-the-art Pt/C electrocatalysts showing that both exhibited similar characteristics in alkaline electrolyte at 30 °C.

6. References

An, L., Zhao, T.S., Chen, R., Wu, Q.X., J. Power Sources 196 (2011) 6219–6222.

An, L., Zhao, T.S., Xu, J.B., Int. J. Hydrogen Energy 36 (2011) 13089–13095.

Antolini, E., J. Power Sources 170 (2007) 1–12.

Allebrod, F., High Temperature and Pressure Alkaline Electrolysis, PhD Thesis 2013.

Bae, S.J., Yoo, S.J., Lim, Y., Kim, S., Lim, Y., Choi, J., Nahm, K.S., Hwang, S.J., Lim, T.H., Beak, S., Jung, D., Nahm, K.S., Kim, P., Catal. Lett. 134 (2010) 288-294.

Bard, A.J., Faulkner, L.R., Electrochemical methods: fundamentals and applications. New York: John Wiley & Sons Ltd, 1980.

Bin, W., Lu, B., Qian-Ming, G., Ji, L., Acta Phys. –Chim. Sin., 25 (2009) 1065-1069.

Chaiburi, C., Hacker, V., 10 Minisymposium Verfahrentechnik, Vienna University of Technology, (2014) 124-127.

Chain, E.E., Appl. Opt. 30 (1991) 2782-2787.

Chakrabarti, A., Hermann, K., Druzinic, R., Witko, M., Wagner, F., Petersen, M., Physical Review B. 59 (1999) 10583-10590.

Chaparro, A.M., Martin, A.J., Daza, L., ECS Transactions, 23 (2010) 125-133.

Chatenet, M., Molina-Concha, M. B., El-Kissi, N., Parrour, G., Diard, J. P., Electrochimica Acta 54 (2009) 4426-4435.

Chauhan, S., Jyoti, J., Kumar, G., J. Molecular Liquids. 159 (2011) 196-200

Cheng, X., Shi, Z., Glass, N., Zhang, L., Zhang, J., Song, D., Liu, Z.S., Wang, H., Shen, J., J. Power Sources. 165 (2007) 739-756.

Delime, F., Le´Ger, J., Lamy, C., J. Appl. Electrochem. 28 (1998) 27–35.

EG&G Technical Services Inc, Fuel Cell Hand Book, 7th edn., US Department of Energy, 2004.

Garcia, A. C., Linares, J. J., Chatenet, M., Ticianelli, E. A., Electrocatalysis 5 (2014) 41–49.

Garsany, Y., Dutta, S., Swider-Lyons, K.E., J. Power Sources. 216 (2012) 515-525.

Gasteiger, H.A., Vielstich, W., Yokokawa, H., Handbook of Fuel Cells, Chichester: John Wiley & Sons Ltd, 2009.

Ge, L., Zhang, X., Guo, R., Polymer. 48 (2007) 2681-2691.

Grimmer, C., Zacharias, R., Grandi, M., Pichler, B. E., Kaltenböck, I., Gebetsroither, F., Wagner, J., Cermenek, B., Weinberger, S., Schenk, S., Hacker, V., Journal of the Electrochemical Society 163 (2016) 278-283.

Gómez-Marin, A.M., Rizo, R., Feliu, J.M., Beilstein Journal of Nanotechnology 4 (2013) 956-967.

Han, P., Bartels, D. M., J. Phys. Chem. 100 (1996) 5597-5602.

He, Q., Mukerjee, S., Electrochimica Acta. 55 (2010) 1709-1719.

Heath, J., Energy Dispersive Spectroscopy. West Sussex: John Wiley & Sons Ltd, 2015

Huang, T., Mao, S., Zhou, G., Wen, Z., Huang, X., Ci, S., Nanoscale. 6 (2014) 9608-9613.

Incropera, F., Liquid Cooling of Electronic Devices by Single-Phase Conversion, New York: John Wiley & Son Ltd, 1999.

Jiang, L., Hsu, A., Chu, D., Chen, R., Int. J. Hydrogen Energy 35 (2010) 365–372.

Jung, J.H., Kim, S.H., Hur, S.H., Joo, S.H., Choi, W.M., Kim, J., J. Power Sources. 226 (2013) 320-328.

Kim, S.K., Kim, P., J. Materials Chemistry. 22 (2012) 8820-8825.

Kissinger, P.T., Heineman, W.R., Journal of Chemical Education, 60 (1983) 702- 706.

Koscher, G., Kordesh, K., J. Power Sources. 136 (2004) 215-219.

Kutz, R.B., Braunschweig, B., Mukherjee, P., Behrens, R.L., Dlott, D.D., Wieckowski, A., J. Catal. 278 (2011) 181–188.

Lai, S.C.S., Kleijn, S.E.F., Öztürk, F.T.Z., van Rees Vellinga, V.C., Koning, J., Rodriguez, P., Koper, M.T.M., Catal. Today 154 (2010) 92–104.

Lai, S.C.S., Koper, M.T.M., Phys. Chem. Chem. Phys. 11 (2009) 10446–10456.

Lamy, C., Rousseau, S., Belgsir, E.M., Coutanceau, C., Léger, J.M., Electrochim. Acta 49 (2004) 3901–3908.

Liu, H., Zhang, J., Electrocatalysis of Direct Methanol Fuel Cells, Chichester: John Wiley & Sons Ltd, 2009.

Mao, C., Wu, X., Pan, H., Zhu, J., Chen, H., Nanotechnology. 16 (2005) 2892-2896.

Markovic, N.M., Ross, P.N.,Surf. Sci. Rep. 45 (2002) 117–229.

Meng, H., Shen, P. K., Electrochem. Commun. 8 (2006) 588–594.

Miley, G.H., Luo, N., Mather, J., Burton, R., Hawkins, G., Gu, L., Byrd, E., Gimlin, R., Shrestha, P.J., Benavides, G., J. Laystrom, D. Carroll, J. Power Sources 165 (2007) 509–516.

Modestov, A.D., Tarasevich, M.R., Leykin, A.Y., Filimonov, V.Y., J. Power Sources 188 (2009) 502–506.

Norskov, J.K., Rossmeisl, J., Logadotir, A., Lindqvist, L., Kitchin, J.R., Bligaard, T., J. Phys. Chem. B. 108 (2004) 17886–17892.

Parsons, R., Vandernoot, T., J. Electroanal. Chem. Interfacial Electrochem. 257 (1988) 9–45.

Pham, Q.T., Food Freezing and Thawing Calculations, London: Springer, 2014.

Pilatowsky, I., Romero, R.J., Isaza, C.A., Gamboa, S.A., Sebastian, P.J., Rivera, W., Cogeneration Fuel Cell-Sorption Air Conditioning System, London: Springer, 2011.

Qiao, J., Xu, L., Ding, L., Shi, P., Baker, R., Zhang, J., International Journal of Electrochemical Science 8 (2013) 1189-1208.

Rayment, C., Sherwin, S., Introduction to Fuel Cell Technology, Department of Aerospace and Mechanical Engineering, University of Notre Dame, 2003.

Selvaraj, V., Alagar, M., Nanotechnology 19 (2008) 1-8.

Shi, Z., Zhang, J., Liu, Z., Wang, H., Wilkinson, D.P., Electrochim. Acta. 51 (2006) 1905–1916.

Spendelow, J.S., Wieckowski, A., Phys. Chem. Chem. Phys. 9 (2007) 2654–2675.

Suib, S. L., New and Future Developments in Catalysis, Batteries, Hydrogen Storage and Fuel Cells. Amsterdam: Elsevier (2013) 437.

Tang, Q., Jiang, L., Qi, J., Jiang, Q., Wang, S., Sun, G., Applied Catalysis B: Environmental 104 (2011) 337-345.

Taylor, R.J., Humffray, A.A., J. Electroanal. Chem. 64 (1975) 63–84.

Taylor, R.J., Humffray, A.A., J. Electroanal. Chem. 64 (1975) 85–94.

Varcoe, J.R., Slade, R.C.T., Fuel Cells 5 (2005) 187–200.

Vigier, F., Coutanceau, C., Hahn, F., Belgsir, E.M., Lamy, C., J. Electroanal. Chem. 563 (2004) 81–89.

Vijh, A.K., Can. J. Chem. 49 (1971) 78-88.

Wang, J., Wasmus, S., Savinell, R.F., J. Electrochem. Soc. 142 (1995) 4218–4224.

Wang, Y., Li, L., Hu, L., Zhuang, L., Lu, J., Xu, B., Electrochem. Commun. 5 (2003) 662–666.

Wieland, B., Lancaster, J.P., Hoaglund, C.S., Holota, P., Tornguist, W.J., Langmuir 12 (1996) 2594-2601.

Wu, Q., Jiang, L., Qi, L., Yuan, L., Wang, E., Sun, G., Electrochimica Acta. 123 (2014) 167-175.

Xing, W., Yin, G., Zhang, J., Rotating Electrode Methods and Oxygen Reduction Electrocatalysts. Amsterdam: Elsevier (2014) 1-31.

Yang, H., Kumar S., Zou S., Journal of Electroanalytic Chemistry 688 (2013) 180-188.

Yeager, E., J. Mol. Catal. 38 (1986) 5–25.

Yu E.H., Krewer, U., Scott, K., Energies 3 (2010) 1499–1528.

Zhang, J., PEM Fuel Cell Electrocatalysts and Catalyst layer. London: Springer, 2008.

Zhang, L., Zhang, J., Wilkinson, D.P., Wang, H., J. Power Sources 156 (2006) 171–182.

Zhang, Z., Qu, C., Zheng, T., Lai, Y., Li, J., International Journal of Electrochemical Science. 8 (2013) 6722-6733.

Zhdanov, V.P., Kasemo, B., Electrochem. Commun. 8 (2006) 1132–1136.

7. Appendix

LIST OF FIGURES

2. Fundamental

3. Performance decrease of platinum fuel cell catalyst by coolant leakage (section 1)

4. Investigation of performance decrease of non-Pt based electrocatalysts in presence of ethanol leakage (section 2)

LIST OF TABLES

3. Performance decrease of platinum fuel cell catalyst by coolant leakage (section 1)

4. Investigation of performance decrease of non-Pt based electrocatalysts in presence of ethanol leakage (section 2)

LIST OF SYMBOLS

2. Fundamental

AADEFCs is Alkaline acid direct ethanol fuel cells

A is the electrode geometric surface area (cm^2)

ATR-FTIR is attenuated total reflectance fourier transform infrared spectroscopy

C* is the electrolyte concentration (mol/cm^3)

CV is cyclicvoltammetry

C_P is the heat capacities

D is the diffusion coefficient (cm^2/s)

DEFCs is Direct ethanol fuel cells

DMFCs is Direct methanol fuel cells

E is the ideal potential of the cell

EDX is energy dispersive X-ray spectroscopy

EMF is electromotive force

F is Faraday's constant (96,487 $Cmol^{-1}$)

G_i^0 is the partial molar Gibbs free energy for species i at temperature T

i_l is limiting current or levich current (A/cm^2)

i_k is the kinetic current density

n is the number of electrons participating in the reaction

ORR is oxygen reduction reaction

PEMFCs is Proton exchange membrane fuel cells

RDE is a rotating disk electrode

SEM is the scanning electron microscopy

T is the temperature

TEM is the transmission electron microscopy

W_{el} is the maximum electrical work

ΔG is the Gibbs free energy change

ΔG^0 is the Gibbs free energy change at the standard pressure (1atm)

ΔG_f is the Gibbs free energy of formation

ΔH is the enthalpy change

ΔH_f is the enthalpy of formation

ΔS is the entropy change

ω is the rotation rate (rad/s)

υ is the kinematic viscosity (cm^2/s)

3. Performance decrease of platinum fuel cell catalyst by coolant leakage (section 1)

A is geometric surface area of the glassy carbon working electrode

CV is cyclicvoltammetry

ECSA is electrochemical surface area

EDX is energy dispersive X-ray spectroscopy

EG is ethylene glycol

H_{upd} is the underpotentially electrodeposited

hcd is the high current densities

i_d is the limiting current

i_k is the kinetic current

i_o is the observed current

lcd is the low current densities

L_{Pt} is Pt loading on the surface of the working electrode

MA is mass activity

ORR is oxygen reduction reaction

PEMFCs is Polymer electrolyte membrane fuel cells

RDE is a rotating disk electrode

RHE is a reversible hydrogen electrode

SEM is the scanning electron microscopy

4. Investigation of performance decrease of non-Pt based electrocatalysts in presence of ethanol leakage (section 2)

ADEFCs is Alkaline direct ethanol fuel cells

A is geometric surface area of the glassy carbon working electrode

C_O is the bulk concentration of the oxygen

D_O is the diffusion coefficient of the oxygen

EDX is energy dispersive X-ray spectroscopy

F is the Faraday constant (96,485 $Cmol^{-1}$)

i_d is the limiting current

i_k is the kinetic current

i_l is the diffusion limiting current

i_o is the observed current

n is the number of electrons transfer

ORR is oxygen reduction reaction

RDE is a rotating disk electrode

RHE is a reversible hydrogen electrode

TEM is the transmission electron microscopy

ν is the kinematic viscosity of the working electrolyte

ω is the angular rotation rate of the electrode

8. Annex


PBFC 2013
Ulm, Germany
June 3-7, 2013
6th International Conference
on
Polymer Batteries and Fuel Cells
ZSW
HIU
Helmholtz Institute Ulm
Electrochemical Energy Storage
WBZU
www.pbfc.eu

Preparation of PtNi/C catalysts for polymer electrolyte membrane fuel cells

Chakkrapong Chaiburi, Viktor Hacker
Institute of Chemical Engineering and Environmental Technology,
Graz University of Technology, Steyrergasse 21, 8010 Graz, Austria
E-mail : chakkrapong.chaiburi@student.tugraz.at

A major challenge for commercialization of the fuel cells are the high manufacturing costs of PEMFCs. The costs of the catalysts represent approx. 30% of the overall manufacturing costs because currently platinum is the catalyst for both anodes and cathodes in PEMFCs. This work focuses on PtNi supported on carbon. The kinetic current density (i_k) of the ORR of $Pt_{3.36}Ni/C$ and $PtNi_{1.15}/C$ catalysts was investigated. Carbon-supported PtNi nanoparticles were prepared in a two step method. Nickel (II) chloride ($NiCl_2 \cdot 6H_2O$), $H_2PtCl_6 \cdot 6H_2O$ and sodium borohydride ($NaBH_4$) were dissolved in 0.26 g ethylene glycol (EG) and stirred at 60°C for 0.5 h. The solution was kept at this temperature 90°C for 0.5 h. Carbon black Vulcan®XC72 was added to the mixture. The morphology of the carbon-supported bimetallic nanoparticles was characterized by Scanning Electron Microscope (SEM) and the amount of Pt and Ni in catalysts was measured by X-Ray Fluorescence Spectrometer (XRF). The electrocatalytic oxygen reduction reaction (ORR) activities were measured in 0.1 M NaOH using cyclic voltammetry and rotating disk electrode method. The Plot curve showed linear oxidation and reduction behavior the Levich plot's equation and the Koutecky-Levich plot showed the result of slope clearly varies depending on the catalyst layer. The Levich plot (Fig.1) and Koutecky-Levich plot (Fig.2) are presented below.

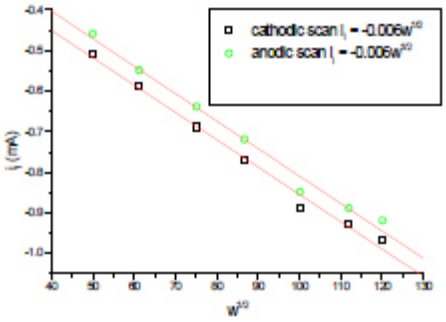

Figure 1.Levich plot of $Pt_{3.36}Ni/C$

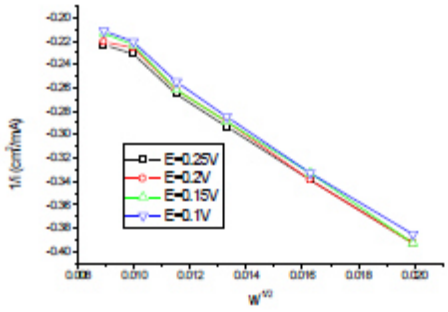

Figure 2.Koutecky-Levich plot of $Pt_{3.36}Ni/C$

10. Minisymposium Verfahrenstechnik

June 17th - June 18th, 2014

Vienna University of Technology

Proceedings

Performance decrease of platinum fuel cell catalyst by coolant leakage

Chakkrapong Chaiburi, Viktor Hacker
Institute of Chemical Engineering and Environmental Technology, Graz University of Technology, Inffeldgasse 25 C, 8010 Graz, Austria
chakkrapong.chaiburi@student.tugraz.at

Abstract

A fuel cell is an electrochemical generator of electricity and heat by the electrochemical reactions. The leakage of the coolant during operation of the fuel cell but can influence the performance of the platinum (Pt) electrocatalyst. The degradation effects of the glycol-based coolant formulations on the active sites of the Pt electrocatalysts were investigated.

Introduction

Polymer electrolyte fuel cells (PEMFCs) are generator systems for hydrogen and air supply, with the fuel cell stack consisting of steel endplates, bipolar plates and the membrane electrode assembly (MEA), humidifier and cooling loops. They convert electrochemical reactions, such as the oxidation of the hydrogen at the anode and the reduction of the oxygen at the cathode, directly into electricity, giving water as the only by-product. It emits heat generated by the electrochemical reactions or by the electron passing through the fuel cells. Generally, ethylene glycol (EG) is used as a coolant in traditional engines and it (bp. 198°C) can also be used to cool a fuel cell. However, coolant might decrease the performance of the PEMFC when it causes a leak to the PEMFC. The coolant can poison the catalyst via the oxidation reaction of ethylene glycol on the Pt catalyst sites. Garsany *et al.* studied coolants such as glycol/water and glycol/water/surfactant mixtures which cause the loss of Pt electrochemical surface area (ECSA), but the Pt fully recovered after being contaminated (clean electrolyte). The surfactant was an ethoxylated nonylphenol [1]. In this study, we investigate glycol-based coolant formulations to show the decrease poisoning effects on the active sites of Pt electrocatalysts when the coolant leakage occurs into the system by using the cyclic voltammetry (CV) method. For the Pt ECSA, comparisons are given of the Pt ECSA between initial CV and CV after being contaminated, and then the loss of Pt electrochemical surface area (ECSA) is calculated.

Experimental

Physical characterization methods

Morphology of 30 wt. % Pt/C commercial catalysts (E-Tek) was determined using scanning electron microscopy, (SEM).The element compositions of Pt/C catalysts was analysed by the energy dispersive X-ray spectroscopy, (EDX).

Coolant materials

The coolant was made from ethylene glycol, water and a non-ionic surfactant. The non-ionic surfactant was Triton X ($C_{14}H_{22}O(C_2H_4O)_n$).

Electrochemical measurements

All electrochemical measuring techniques were carried out with standard three-electrodes at 303 K. The 0.10 M H_2SO_4 working electrolyte was prepared from nanopure water (18 MΩ-cm, Barnstead Nanopure). The reference electrode was used as a reversible hydrogen electrode (RHE) and a platinum electrode was used as the counter electrode. The working electrode was glassy carbon. Ultra high purity nitrogen (N_2) and oxygen (O_2) were employed. The catalysts were carried out on a commercial 30 wt % Pt supported on vulcan carbon XC-72, Pt/C (E-Tek). For a rotating disk electrode, (RDE), the catalyst ink was prepared on a glassy carbon electrode ∅ equal to 5 mm, surface area equal to 0.196 cm^2. The working electrode Pt-loading was 28 $\mu g_{Pt} cm^{-2}$. The electrochemical measurement applied is for cyclic voltammetry (CV)and the results were calculated for the loss of Pt ECSA.

$$ECSA_{Pt,cat}(m^2 g_{Pt}^{-1}) = \frac{[Q_{H-adsorption}(C)]}{[210\mu C cm_{Pt}^{-2} L_{Pt}(mg_{Pt}cm^{-2})Ag(cm^2)} X10^5$$

where ECSA is the Pt ECSA ($m^2 g_{Pt}^{-1}$) obtained from calculating and Q_H =210 μCcm^{-2}. L_{Pt} ($mg_{Pt}cm^{-2}$) is Pt loading on the surface of the working electrode and A_g (cm^{-2}) is the geometric surface area of the glassy carbon working electrode [1]. The loss of Pt ECSA due to a contaminant is calculated:

$$ECSA_{loss}(\%) = \frac{(ECSA_{initial} - ECSA_{final})}{ECSA_{initial}} \text{x}100$$

Results

Physical characterization

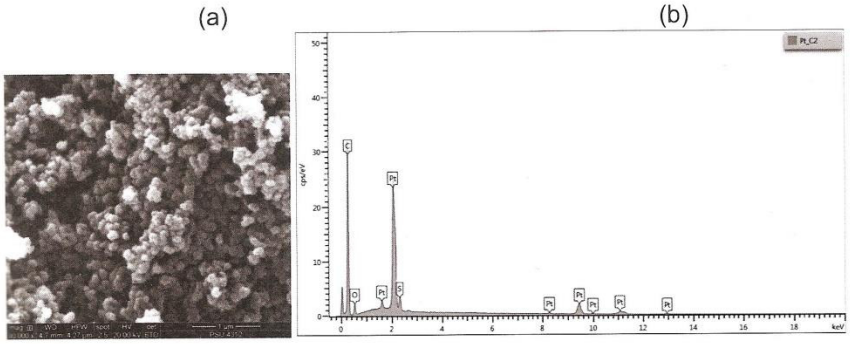

Figure 1: (a) Typical of SEM for a commercial 30% Pt/C (E-Tek) (magnification is 30000) (b)Typical of EDX for a commercial 30% Pt/C (E-Tek)

In Figure 1a, the morphology of a commercial 30% Pt/C catalyst sample shows the sphere powder aggregated structure. The composition of commercial 30% Pt/C catalyst shows an average of the elements at 63.80% of C, 4.65% of O, 1.11% of S and 30.44% of Pt (Figure 1b).

Effect of the ethylene glycol-based coolant on CV characteristics

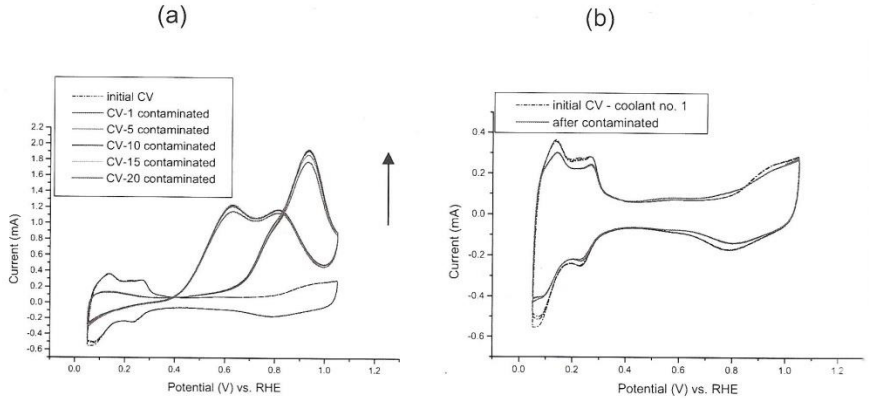

Figure 2: (a) Comparison of initial cyclic voltammogram of Pt/C and cyclic voltammogram of Pt/C (during contamination with coolant no. 1 (a mixture of ethylene glycol and water)) in N_2 purged 0.10 M H_2SO_4 electrolyte (b) Comparison of initial cyclic voltammogram of Pt/C and cyclic voltammogram of Pt/C (after contamination) in N_2 purged 0.10 M H_2SO_4 electrolyte

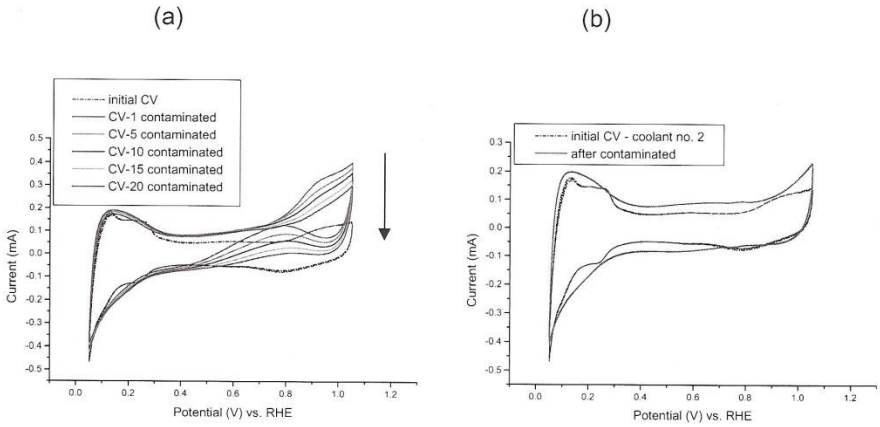

Figure 3: (a) Comparison of initial cyclic voltammogram of Pt/C and cyclic voltammogram of Pt/C (during contamination with coolant no. 2 (a mixture of ethylene glycol, water and triton X 100)) in N_2 purged 0.10 M H_2SO_4 electrolyte (b) Comparison of initial cyclic voltammogram of Pt/C and cyclic voltammogram of Pt/C (after being contaminated) in N_2 purged 0.10 M H_2SO_4 electrolyte

Figure 2a, the CV cycle increases, the anodic current peaks enhancing very slowly cycle by cycle. As viewed from Figure 2a, an oxidation peak around 0.9 V is observed in the anodic scan region. Ethylene glycol started increasing to the electrooxidation at 0.5-0.9 V (Figure 2a). A probable mechanism as suggested by Vaithilingam Selvaraj [2, 3]. The loss of Pt ECSA after recovery is 25.09% (Figure 2b).

The CV cycle decrease and the anodic current peaks decrease cycle by cycle (Figure 3a). The ethylene glycol causes oxidation at 0.5-0.9 V during contamination with 1 ml of coolant no. 2. The loss of Pt ECSA after clean electrolyte is 3.48% (Figure 3b).From the data obtained it is most likely that the Triton-X prevents CO from being adsorbed on the surface of the Pt catalyst during coolant contamination. On the electrode surfaces, the EG molecules and the Triton-X will compete to adsorb the CO on the surface of the active sit of the Pt.The CO will be hindered to adsorb on the surface of Pt. Therefore the anodic current peaks electrooxidation reduce cycle by cycle (Figure 3a). As shown in Figure 4, it is expected that first the EG chains may insert into Triton-X micelles. After that Triton-X wraps around the micelles of EG. Figure 4 shows the aggregate structure [4]. This is the reason why Triton-X inhibits EG and generates CO for adsorption on the Pt catalyst sites and prevents EG adsorbing on the working electrode. Figure 3a, shows that EG oxidation decreased.

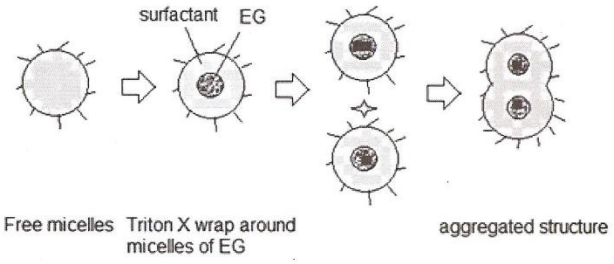

Figure 4: Micelles of Triton-X wrap around EG

Conclusion

The loss of Pt ECSA after clean electrolyte of coolant no. 2 (a mixture of ethylene glycol, water and Triton-X) and coolant no. 1 (a mixture of ethylene glycol and water) show 3.48% and 25.09%, respectively. Performance of the loss of Pt ECSA after clean electrolyte of coolant no. 2 is better than the coolant no. 1. Then the Triton-X prevents CO from ethylene glycol poisoning on the active sites of Pt electrocatalyst during coolant contamination. Triton-X can decrease electrooxidation reaction of ethylene glycol.

References

[1] Y. Garsany, S. Dutta, K.E. Swider-Lyons, J. Power Sources. 216(2012) 515-525
[2] V. Selvaraj, M. Alagar. Nanotechnology 19(2008) 1-8.
[3] J.H. Jung, S.H. Kim, S.H. Hur, S.H. Joo, W.M. Choi, J. Kim, J. Power Sources. 226(2013) 320-328.
[4] L. Ge, X. Zhang, R. Guo, Polymer. 48(2007) 2681-2691.

11. Minisymposium
Verfahrenstechnik

April 14th/15th, 2015

and

2. Österreichisches Partikelforum

April 15th, 2015

University of Natural Resources and Life Sciences, Vienna (BOKU)

Proceedings

Investigation of performance reduction of fuel cells during coolant leakage

Chakkrapong Chaiburi, Viktor Hacker
Institute of Chemical Engineering and Environmental Technology, Graz University of Technology, NAWI Graz, Inffeldgasse 25C, 8010 Graz, Austria
chakkrapong.chaiburi@student.tugraz.at

Abstract

A fuel cell converts chemical energy directly into electrical energy. During the conversion heat and water are generated. To prevent overheating a coolant is used for heat removal in fuel cells. Ethylene Glycol has good cooling charactersitics for an fuel cell. But if it leaks into the fuel cell, it reacts to CO, which results in a performance loss due to poisoning of the Pt catalyst. The comparison of EG+water and EG+water+Triton X shows, that the latter produces less CO due to capture of EG by Triton X. The influence on the oxygen reduction reaction (ORR) was investigated. The applied coolants have an effect on the poisoning of the electrocatalyst.Triton-X reduces carbon monoxide (CO) poisoning at active sites of the Pt electrocatalyst and decreases the electrooxidation reaction of ethylene glycol. The ORR of coolant consisting of ethylene glycol, water and Triton-X inhibits the ethylene glycol electrooxidation.

Introduction

Polymer electrolyte membrane fuel cells (PEMFCs) are energy conversion systems that generate electric energy directly from hydrogen. A PEMFC stack consists of steel endplates, bipolar plates and the membrane electrode assembly (MEA), humidifier and cooling loops. They convert hydrogen and oxygen via electrochemical reaction directly into electricity, giving water as the only by-product. The system ejects heat generated by the electrochemical reactions or by the electrons passing through the fuel cells. Using a liquid coolant has become attractive, owing to the higher heat transfer coefficient achieved as compared with air-cooling [1]. Ethylene glycol (EG) is used as a coolant in traditional engines (boiling point 198 ºC and freezing point less than -40 °C) and it can also be used to cool a fuel cell. However, it might decrease the performance of the PEMFCs if it leaks into the cell. The coolant can poison the catalyst via the oxidation reaction of EG on the Pt catalyst sites. Wieland *et al.* suspected that CO_2 and CO are generated when the C-C bond is broken by the oxidation of EG with the Pt electrocatalyst [2]. Carbon monoxide (CO) is a well-known catalyst poison in fuel cells. The CO is strongly adsorbed and blocks the Pt catalyst sites [3]. However, there have been few studies to determine the deleterious quantity of a coolant such as EG which affects the performance of the PEMFC. Garsany *et al.* studied coolants such as glycol+water and glycol+water+surfactant mixtures which cause the loss of Pt electrochemical surface area (ECSA). The surfactant was an ethoxylated nonylphenol. The Pt fully recovered after being contaminated in ex-situ experiments (by replacing the electrolyte) [4].
In this research, the ex-situ oxygen reduction reaction (ORR) method was used to investigate glycol-based coolant formulations to show any deleterious poisoning effects on the active sites of Pt electrocatalysts when coolant leakage occurs into the system. Triton-X ($C_{14}H_{22}O(C_2H_4O)_n$) as a non-ionic surfactant was added to ethylene glycol based coolants.

Experimental

Selected coolants

The coolant made from a mixture of ethylene glycol and water is called coolant no. 1. The coolant with additional Triton-X is called coolant no. 4.

Electrochemical measurements

All electrochemical *measuring* techniques were carried out with standard three-electrodes configuration at 30° C. The 0.10 M H_2SO_4 working electrolyte was prepared from nanopure water (18 MΩ-cm, Barnstead Nanopure). The reference electrode was a reversible hydrogen electrode (RHE) and a platinum electrode was used as the counter electrode. The working electrode was a rotating disk electrode (RDE) with glassy carbon substrate. Ultra high purity nitrogen (N_2) and oxygen (O_2) were employed. As catalyst 30 wt % Pt supported on vulcan carbon XC-72, Pt/C (E-Tek) was used. The Pt-loading of the working electrode was 28 μg_{Pt} cm^{-2}. The kinetic current i_k is calculated by equation 1, where i_o is the observed current at 0.90 V vs. RHE and i_d is the diffusion limited current that can be obtained from the ORR curve.

$$i_k = \frac{(i_d i_o)}{(i_d - i_o)} \qquad (1)$$

The mass activity (MA) of the catalyst is calculated by equation 2,

$$MA = \frac{i_k}{L_{Pt}} \qquad (2)$$

where MA (mA/ μg_{Pt}) is mass activity, L_{Pt} (mg_{Pt} cm^{-2}) is Pt loading of the working electrode.

Results

The initial ORR curve of the Pt/C has a defined diffusion-limiting current around E = 0.10-0.50 V and a kinetic-diffusion mixed region at *approx.* 0.70 < E < 0.90 V (Fig. 1A). The MA value is calculated using the mass transport-correction from equation (2) where the kinetic current, i_k, is obtained from the value of the polarization curve at 0.90 V vs. RHE and i_d at E = 0.30 V vs. RHE. These Pt MAs are compared in Fig. 1C. The MA measured for the clean Pt/C electrode is 21.75 ± 3.4 mA/mg_{Pt}. After the contamination occured, the MA obtained after 20 ORR cycle is equal to 16.35 ± 2.0 mA/ mg_{Pt}. By extending the cyclic voltammetry (CV) procedure, the MA is 17.41 ± 1.1 mA/ mg_{Pt}. Fig. 1B, the ORR during contamination shows ethylene glycol oxidation at potential *ca.* 0.5-0.9 V (Fig.1B).

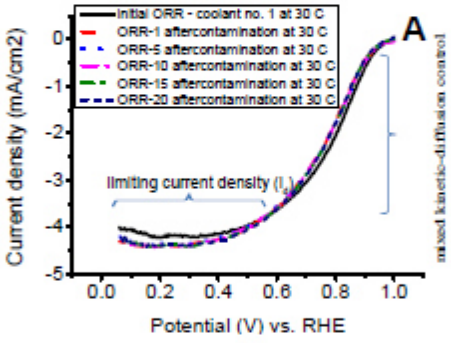

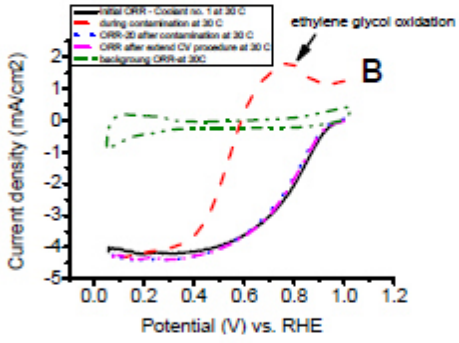

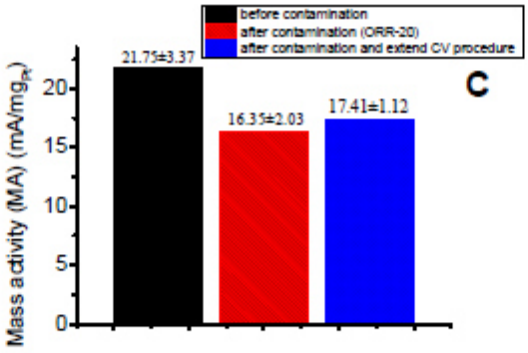

Fig. 1. A) Comparison of initial ORR to after contamination with coolant no. 1 of ORR-1, ORR-5, ORR-10, ORR-15 and ORR-20 of the ORR polarization curve obtained in a 0.1M H_2SO_4 electrolyte B) Comparison of initial ORR, during contamination, after contamination with coolant no. 1 of ORR-20 and ORR after extended CV procedure C) Comparison of MA calculated before contamination, after contamination of ORR-20 and ORR after extended CV procedure. (ORR-1 as 1st cycle, ORR-5 as 5th cycle, ORR-10 as 10th cycle, ORR-15 as 15th cycle, ORR-20 as 20th cycle).

These Pt MAs are compared in Fig. 2C. The MA measured for the initial Pt/C is equal to 23.28 ± 4.9 mA/mg$_{Pt}$. After contamination, the MA obtained for ORR-20 is 13.71 ± 3.5 mA/mg$_{Pt}$. After contamination and extended CV procedure, the MA is 14.18 ± 3.6 mA/ mg$_{Pt}$. Fig. 2B shows decreasing ethylene glycol oxidation during ORR contamination.

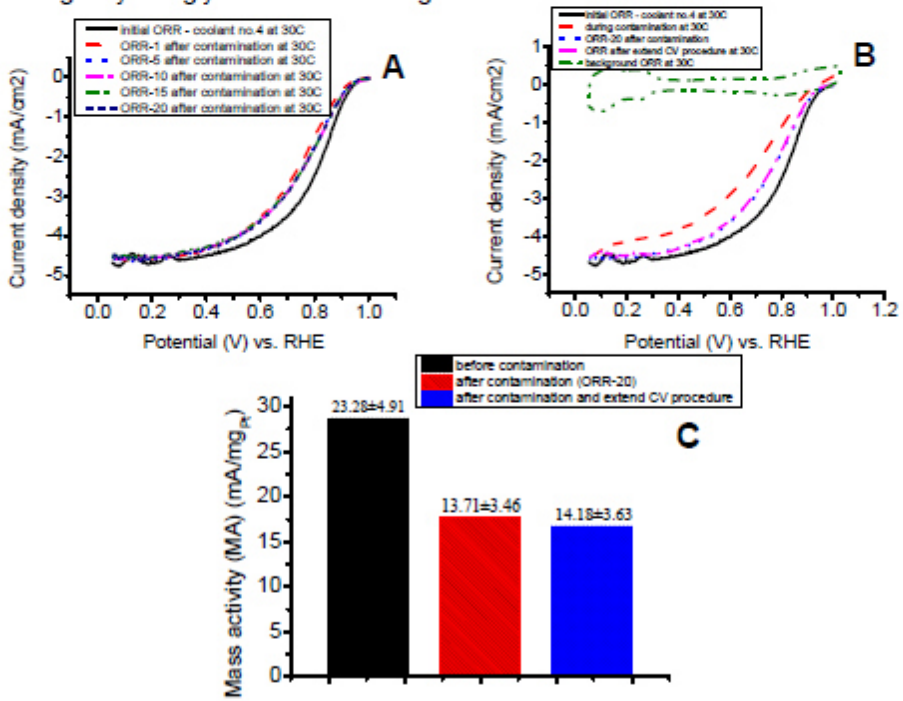

Fig. 2. A) Comparison of initial ORR to after contamination with coolant no. 4 of ORR-1, ORR-5, ORR-10, ORR-15 and ORR-20 of the ORR polarization curve obtained in a 0.1M H_2SO_4 electrolyte B) Comparison of initial ORR, during contamination, after contamination with coolant no. 4 of ORR-20 and ORR after extended CV procedure C) Comparison of MA

calculated before contamination, after contamination of ORR-20 and ORR after extended CV procedure. (ORR-1 as 1st cycle, ORR-5 as 5th cycle, ORR-10 as 10th cycle, ORR-15 as 15th cycle, ORR-20 as 20th cycle).

As shown in Fig. 3, it is expected that first the EG molecules may insert into Triton-X micelles. Fig. 3 shows the aggregate structure [5]. Therefore, Triton-X reduces CO from ethylene glycol that poisons the active sites of the Pt electrocatalyst during coolant contamination. According to this machanism, Triton-X inhibits EG from being oxidized to CO on the working electrode.

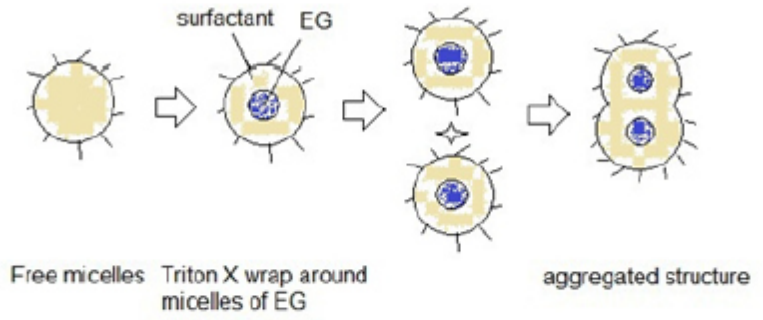

Fig. 3. Micelles of Triton-X wrap around EG [6]

Conclusions

The ORR during contamination with coolant no. 1 shows ethylene glycol oxidation at potentials of 0.5-0.9 V vs. RHE. Coolant no. 4 illustrates the decreasing electrooxidation kinetics of ethylene glycol during ORR. From the data obtained it is most likely that the Triton-X prevents CO formation due to the aggregation of micelles.

References

[1] F. Incropera, Liquid Cooling of Electronic Devices by Single-Phase Conversion, John Wiley & Son (New York, 1999), pp. 125-163
[2] B. Wieland, J.P. Lancaster, C.S. Hoaglund, P. Holota, W.J. Tornguist, Langmuir 12(1996) 2594-2601.
[3] X. Cheng, Z. Shi, N. Glass, L. Zhang, J. Zhang, D. Song, Z.S. Liu, H. Wang, J. Shen, J. Power Sources. 165(2007) 739-756.
[4] Y. Garsany, S. Dutta, K.E. Swider-Lyons, J. Power Sources. 216(2012) 515-525.
[5] L. Ge, X. Zhang, R. Guo, Polymer. 48(2007) 2681-2691.
[6] C.Chaiburi, V. Hacker, 10 Minisymposium Verfahrentechnik, Vienna University of Technology, (2014) 124-127.

Conference Proceedings

Graz, March 30th and 31st, 2016

organized by the

Institute of Paper, Pulp and Fibre Technology
Institute of Process and Particle Engineering

Study on ethanol-tolerant electrocatalysts for oxygen reduction reaction in alkaline media

Chakkrapong Chaiburi, Bernd Cermenek, Birgit Elvira Pichler, Christoph Grimmer, Viktor Hacker
Institute of Chemical Engineering and Environmental Technology, Fuel Cell Systems Group, Graz University of Technology, NAWI Graz, Inffeldgasse 25C, 8010 Graz, Austria
chakkrapong.chaiburi@student.tugraz.at

Abstract

Ag/C, Mn_3O_4/C and $AgMn_3O_4$/C electrocatalysts were synthesized by means of colloid method and their ethanol tolerance was investigated by cyclic voltammetry using a rotating disc electrode. Further, the morphology, structure and element composition of electrocatalysts were characterized by transmission electron microscopy and energy dispersive X-ray spectroscopy, respectively. The electrocatalysts showed ethanol-tolerance for oxygen reduction reaction in KOH electrolyte. As a result all of the electrocatalysts prevented ethanol oxidation reaction. The most recent result confirmed that the $AgMn_3O_4$/C electrocatalyst improved the catalytic activity significantly.

Introduction

There are varying reasons for performance loss during lifetime of an alkaline direct ethanol fuel cells (ADEFCs), including exposure to crossover compounds like ethanol. The fuel is ethanol containing KOH. At the cathode compartment, the oxidant is air. However, the ADEFCs efficiency is influenced by ethanol crossover via a membrane from the anode to cathode side. The ethanol are adsorbed on the active surface of the electrocatalyst, thereby blocking and preventing the adsorption of oxygen molecules. Therefore, the development of ethanol-tolerant cathode catalysts for ADEFCs is necessary. In this research, the activities of Ag/C, Mn_3O_4/C and $AgMn_3O_4$/C electrocatalysts towards oxygen reduction reaction (ORR) were investigated in a KOH/EtOH electrolyte by cyclic voltammetry using a rotating disk electrode (RDE).

Experimetal investigation

Synthesis of cathode electrocatalysts

The Ag/C electrocatalyst was synthesized by colloid method [1]. The 20 wt. % Ag/C catalyst was prepared using mixture of trisodium citrate dihydrate and $AgNO_3$, which were dissolved in ultrapure water (~18 MΩ-cm). The solution was stirred until it clearified completely. After some minutes of stirring a drop of $NaBH_4$ solution was added to the Ag solution. The colloid solution exhibited a yellowish-brown colour. Over a period of 15-20 min the whole $NaBH_4$ solution was dropped slowly to the fast stirred Ag solution. The solution became dark brown. The Ag nanomaterial was stirred for 15-30 min. Afterwards, Vulcan XC-72R carbon black as support material was dispersed in ultrapure water with an ultrasonic probe approximately 10 min and added slowly to fast stirred Ag solution. The Ag was precipitated on the carbon back. The mixture was stirred approximately 3 h. The suspension was centrifuged at 11400 rpm for 10 min. The Ag nanoparticles were filtrated and washed twice with ultrapure water. After that, the Ag/C catalyst was dried over night at 90 °C. The yield exhibited between 88% and 93%. The Mn_3O_4/C electrocatalyst [1] was

prepared by blending Vulcan XC-72R dispersed in ethanol-water mixed solution (8:2 v/v). Afterwards, $Mn(NO_3)_2{\cdot}4H_2O$ was added and the solvent of the slurry was removed by stirring over night at 60 °C. Finally, the Mn_3O_4/C was calcined in a furnace at 400 °C for 2 h under N_2 atmosphere (heating rate 5 °C min^{-1}). The $AgMn_xO_y$ electrocatalyst [1, 2, 3] was obtained by two-step synthesis. In the first step $AgNO_3$ and $KMnO_4$ (molar ratio 1:1) were dissolved in ultrapure water at 80 °C, which was acidified with a drop of 65% HNO_3. The solution was slowly cooled to 0 °C. The suspension came dark-blue needles and precipitated. The $AgMnO_4$ was filtrated, washed with ice ultrapure water and dried. In the next step, the $AgMn_3O_4$/C catalyst was synthesized dissolving of $AgMnO_4$ in ultrapure water at ca. 40-50 °C. An approximate amount of Vulcan XC-72R carbon black was added. The black slurry was dispersed with ultrasonic for 15 min. After that, the water in black slurry was slowly evaporated at constant 60 °C. Finally, the dry powder was calcined in a tubular furnace for 2 h at 400 °C under N_2 atmosphere with a heating rate 5 °C min^{-1} and $AgMn_3O_4$/C electrocatalyst obtained.

Characterisation of cathode electrocatalysts

The morphology of Ag/C, Mn_3O_4/C and $AgMn_3O_4$/C electrocatalysts were determined by transmission electron microscopy (TEM), which is a type of electron microscope that can transmit via an ultra-thin specimen and present high resolution images of the sample surface. The element compositions of Ag/C, Mn_3O_4/C and $AgMn_3O_4$/C electrocatalysts were measured by energy dispersive X-ray spectroscopy (EDX).
The activities of all electrocatalysts were determined by cyclic voltammetry using a rotating disk electrode (RDE). All electrochemical measurements were carried out with a standard three-electrode configuration in a 0.1 M KOH electrolyte at 30° C. For the experimental setup, a reversible hydrogen electrode (RHE) as reference electrode , a platinum electrode as counter electrode and a rotating disk electrode (RDE) as working electrode were used. The electrocatalyst loading on the RDE was 56 μg cm^{-2}. A commercial Pt/C electrocatalyst was used as reference.

Physical characterisation of $AgMn_3O_4$/C catalysts

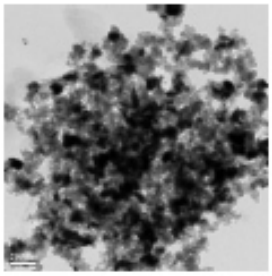

***Fig. 1.** Transmission electron microscopy (TEM) of the $AgMn_3O_4$/C electrocatalyst.*

The TEM image shows three morphologies, including (1) dark spherical particles, (2) gray spherical particles and (3) branch-like particles. The dark spherical particles are attributed to Ag or Mn and the gray spherical particles as activated carbon. The branch-like particles are likely manganese oxides [4].

Electrochemical measurements

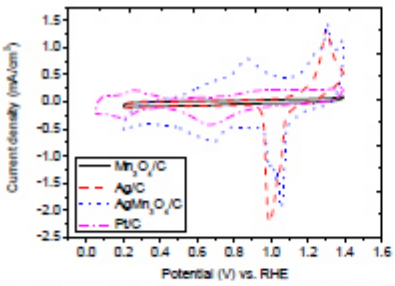

Fig. 2. Base cyclic voltammograms of Ag/C, Mn_3O_4/C and $AgMn_3O_4$/C electrocatalysts in a deaerated 0.1 M KOH at 30 °C, with sweep rate of 10 mV s^{-1}.

The $AgMn_3O_4$/C electrocatalysts exhibits overlapping of the oxidation peaks of Ag and Mn_3O_4 (at a potential of 1.2-1.4 V). However, the reduction peak of $AgMn_3O_4$ (at a potential of 0.9-1.1 V) is higher than the reduction peak of Ag (Fig. 2). The $AgMn_3O_4$/C electrocatalysts are believed to be advantageous for improving ORR activity [5].

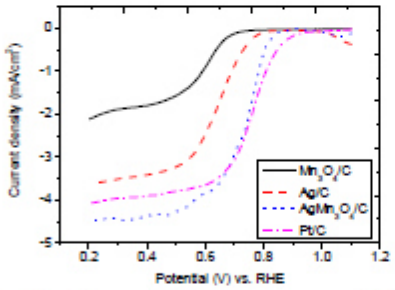

Fig. 3. Linear potential scan curves of Pt/C, Ag/C, Mn_3O_4/C and $AgMn_3O_4$/C electrocatalysts on a rotating disk electrode in an O_2 saturated 0.1 M KOH at 30 °C, with a sweep rate of 10 mV s^{-1} and a rotation rate of 1600 rpm.

ORR polarisation curves of Ag/C, Mn_3O_4/C and $AgMn_3O_4$/C electrocatalysts under an O_2 atmosphere 0.1 M KOH electrolyte at 30 °C with a scan rate of 10 mV s^{-1} and a rotating rate of 1600 rpm are shown in Figure 3. The initial ORR polarisation curves of the electrocatalysts possess a well defined diffusion-limiting current at a potential between 0.20 and 0.70 V, followed by a region under mixed kinetic-diffusion control at $0.70 < E < 0.90$ V (Fig. 3). The performance of the $AgMn_3O_4$/C electrocatalyst was compared to Pt/C electrocatalyst and found to be nearly the same in 0.1 M KOH at 30 °C.
Electrocatalytic activities towards oxygen reduction of Pt/C, Ag/C, Mn_3O_4/C and

$AgMn_3O_4/C$ electrocatalysts in a 0.1 M KOH with different ethanol concentrations are shown in Figure 4.

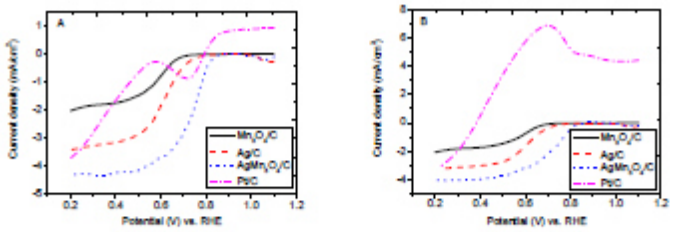

Fig. 4. *(A) Linear potential scan curves of Pt/C, Ag/C, Mn_3O_4/C and $AgMn_3O_4/C$ on a rotating disk electrode in an O_2 saturated 0.1 M KOH with 0.1 M ethanol at 30 °C, a sweep rate of 10 mV s^{-1} and a rotation rate of 1600 rpm. (B) Linear potential scan curves of Pt/C, Ag/C, Mn_3O_4/C and $AgMn_3O_4/C$ on a rotating disk electrode in an O_2 saturated 0.1 M KOH with 1.0 M ethanol at 30 °C, a sweep rate of 10 mV s^{-1} and a rotation rate of 1600 rpm.*

The effect of various ethanol concentrations in alkaline electrolyte on the performance of oxygen reduction of Pt/C working electrode is shown in Figure 4. The results of linear potential scan curves of Pt/C electrocatalyst exhibits ethanol oxidation (at a potential of 0.4-0.75 V) in the presence of ethanol. The opposite way, Ag/C, Mn_3O_4/C and $AgMn_3O_4/C$ electrocatalysts are tolerant towards ethanol for oxygen reduction reaction. This confirms the result of $AgMn_3O_4/C$ electrocatalyst showing significantly enhancement of its ORR activity (Fig.4) towards oxygen reduction.

Conclusion

Ag/C, Mn_3O_4/C and $AgMn_3O_4/C$ electrocatalysts were investigated for oxygen reduction reaction for cathodes of alkaline fuel cells in the presence of different ethanol-concentrations with KOH electrolyte. The electrocatalysts did not oxidise ethanol oxidation and therefore are suitable as cathode catalysts in alkaline direct ethanol fuel cells. $AgMn_3O_4/C$ electrocatalysts showed the best performance for oxygen reduction reaction in presence of ethanol.

References

[1] Q. Tang, L. Jiang, J. Qi, Q. Jiang, S. Wang, G. Sun, Applied Catalysis B: Environmental 104 (2011) 337-345.
[2] Q. Wu, L. Jiang, L. Qi, L. Yuan, E. Wang, G. Sun, Electrochimica Acta 123 (2014) 167-175.
[3] C. Grimmer, R. Zacharias, M. Grandi, B. E. Pichler, I. Kaltenböck, F. Gebetsroither, J. Wagner, B. Cermenek, S. Weinberger, S. Schenk, V. Hacker, Journal of the Electrochemical Society 163 (2016) 278-283.
[4] W. Sun, A. Hsu, R. Chen, J. Power Sources 196 (2011) 627-635.
[5] S. Park, H. Lim, Y. Kim, ACS Catal. 5 (2015) 3993-4002.

TU Graz

Institut für Chemische Verfahrenstechnik und Umwelttechnik
Leitung: Univ.-Prof. Dipl.-Ing. Dr.techn. Matthäus Siebenhofer, Univ.-Prof. Dr.-Ing. Andreas Pfennig

CEET

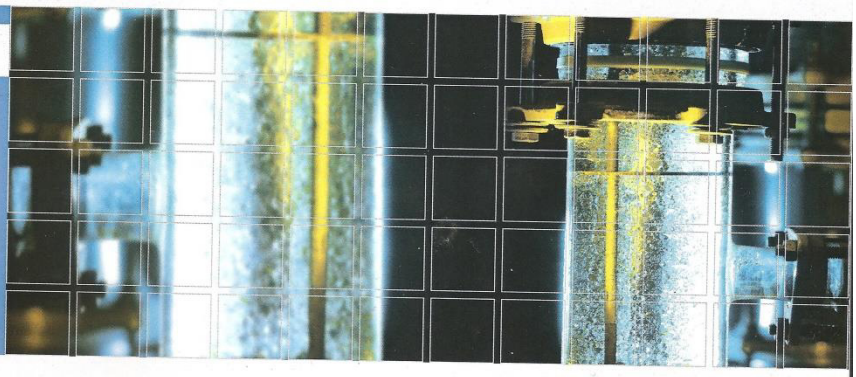

CEET Konkret 2013

Effects of contamination on performance of Polymer Electrolyte Fuel Cells

Chakkrapong Chaiburi

1. Introduction

Polymer electrolyte fuel cells (PEFCs), as illustrated in Fig. 1, convert chemical energy of hydrogen and oxygen directly and efficiently into useful electrical energy with heat and water as the only byproducts. In the last decades fuel cell systems got more and more complex, similar to modern internal combustion engines. The main components are: the fuel system for hydrogen and air supply, the fuel cell stack, consisting of steel endplates, bipolar plates and the membrane electrode assembly, humidifier and cooling loops. However, fuel cells are prone to various sources of contamination due to the complexity of the systems and tend to loose performance during operation. For the widespread uptake of fuel cells it is necessary to gain a better understanding on the impact of impurities on the fuel cells performance [1].

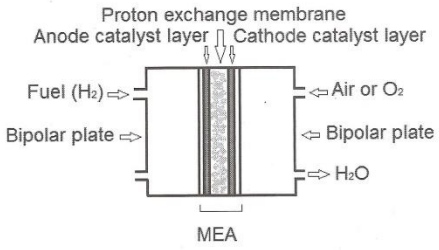

Fig. 1: Basic components of PEFC

2. Sources of contamination in PEFCs

2.1 Anode contamination

Hydrogen is mainly produced by steam reforming of fossil fuels. Therefore, the production process itself leads to unavoidable contaminants, such as CO, CO_2, H_2S and sulfur containing organics in the hydrogen stream. Carbon monoxide (CO) is a well-known catalyst poison in fuel cells. CO adsorbs strongly onto the catalyst surface and blocks the desired oxidation of hydrogen. CO_2 poisoning is not as severe as CO poisoning, but the used catalysts inside the fuel cell converts CO_2 into CO through the reverse water-gas shift reaction [1,2]. Sulfur containing molecules, e.g. hydrogen sulfide (H_2S), adsorb strongly on the Pt catalyst surface. Hence, there is a considerable competition between hydrogen oxidation and the adsorption of sulfur containing molecules. To mitigate the negative impact of fuel contaminants on the performance of the fuel cell, it is necessary to either purify the hydrogen before usage in fuel cells or to increase the tolerance of the catalysts towards contamination. [1-3].

2.2 Cathode contamination

The slow kinetics of the cathode oxygen reduction reaction (ORR) is the key of limiting PEFC performance. Therefore, improving the catalytic activity for ORR has gained the highest attention in fuel cell research. Although contamination of the cathode also reduces the overall performance of fuel cells, cathode contamination has attracted much less attention, even compared to anode contamination. Since air is the most feasible way of supplying the cathode with oxygen, air pollution from industry and traffic has to be taken into account. Pollutants in the air include NO_x (NO_2 and NO), SO_x (SO_2 and SO_3), NH_3, O_3, and some volatile organic compounds (VOCs) such as benzene and toluene. Sulfur oxides (SO_x) poison the cathode catalysts in the same way as described previously for anode catalysts [1,3].
In contrast to anode contamination, cathode contamination mainly affects the electrolyte instead of the catalyst layer. Small amounts of NO_x cause fuel cell performance drops, which can be recovered by supplying pure oxygen or fresh clean air to the cathode. Ammonia, NH_3, reacts with the protons in the ionomer and thus reduces proton conductivity in the catalyst layer. [1,4]. VOCs, e.g. the toluene, decrease the fuel cell performance as well by changing the hydrophilicity of the cathode catalyst support resulting in easy flooding of the cathode side [5].

2.3 Other sources of contamination

The common methods for rejection of excessive heat are air-cooling, evaporative cooling or dissipation of the heat into a coolant loop system. Ethylene glycol (EG) is used as a coolant in traditional combustion engines and therefore it is obvious to use EG for PEFC cooling. But in contrast to ICEs a leakage in

the cooling loop might decrease the performance of a PEFC severely.

EG is electrochemically oxidized at the Pt catalyst surface. Wieland et al. suggested that CO_2 and CO are generated when the C-C bond is broken during oxidation of EG with Pt electrodes in an acidic environment [6]. However, there have been only few studies to examine how the leak time and quantity of coolant (EG) affects the performance of the PEFC, including the membrane electrode assembly (MEA).

3. Goal

The aim of our investigations is to get a better understanding on how coolant leakage affects the catalysts and furthermore to develop strategies to protect the Pt electrocatalysts in case of coolant leakage into the PEFC system.

4. Methods

The comparison of contamination effects of the EG based coolants with and without the addition of non-ionic surfactants was performed by cyclic voltammetry (CV). The obtained CV data was used to calculate the electrochemical active surface area (ECSA) of the catalysts (see Fig. 2). ECSA values of the catalysts were compared before, during and after poisoning by the addition of coolant.

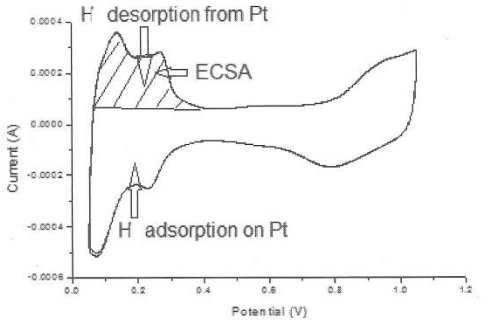

Fig. 2: Cyclic voltammogram of Pt/C in N_2 purged 0.1 M H_2SO_4 electrolyte

5. Results and discussion

Fig. 3 shows the effect of an EG based coolant with additional non-ionic surfactant. From the obtained data it is most likely that the surfactant prevents poisoning of the Pt electrocatalyst during coolant contamination.

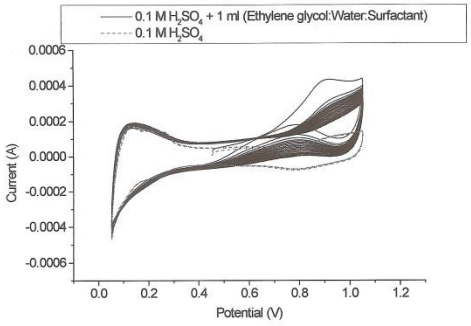

Fig. 3: Comparison of cyclic voltammograms of a Pt/C catalyst in 0.1 M H_2SO_4 without (dash line) and with contamination of coolant (EG:Water:surfactant; solid line)

6. Future work

The experimental work will focus on the investigation of the protective effect of the surfactant at usual PEFC operating temperatures.

7. References

[1] Zamel, N., Li, X., 2011: Effect of contaminats on polymer electrolyte membrane fuel cells. Prog. Energ. Combust. 37, 292 - 329

[2] Cheng, X., Zheng, S., Glass, N., Zhang, L., zhang, J., Song, D., Liu, Z., Wang, H., Shen, J., 2007: A review of PEM hydrogen fuel cell contamination: Impacts, mechanisms and mitigation. J.Power Sources 165, 739 - 756

[3] Mohtadi, R., Lee, W., Van Zee, J.W., 2004: Assessing durability of cathodes exposed to common air impurities. J. of Power Sources. 138, 216–25.

[4] Halseid, R., Vie, P.J.S., Tunold, R., 2006: Effect of ammonia on the performance of polymer electrolyte membrane fuel cells. J Power Sources. 154, 343–50.

[5] Li, H., Zhang, J., Shi, Z., Song, D., Fatih, K., Wu, S., Wang, H., Zhang, J., Jia, N., Wessel, S., Abouatallah, R., Joos, N., 2009:PEM fuel cell contamination: testing and diagnosis of toluene-induced cathode degradation. J. The Electrochem. Soc. 156, B252.

[6] Wieland, B., Lancaster, J.P., Hoaglund, C.S., Holota, P., Tornquist, W.J., 1996: Langmuir12, 2594.

Fragen und Anregungen bitte an:
C. Chaiburi: chakkrapong.chaiburi@student.tugraz.at
V. Hacker: viktor.hacker@tugraz.at

YNU
YOKOHAMA National University

TU Graz

Advanced Studies of Polymer Electrolyte Fuel Cells 6th International Summer School

Shigenori Mitsushima, Takuto Araki, Ken-ichiro Ota, Viktor Hacker, Matthäus Siebenhofer (eds.)

Performance decreaseof platinum fuel cell catalyst by coolant leakage

Chakkrapong CHAIBURI[1] and Viktor HACKER[1]
Institute of Chemical Engineering and Environmental Technology, Graz University of Technology, Steyrergasse 21, 8010 Graz, Austria.chakkrapong.chaiburi@student.tugraz.at

Keywords: Coolant leakage, Pt/C, PEMFC, Fuel Cell

Introduction

Coolant leakages lead to a decrease in performance during the operation of polymer electrolyte fuel cells (PEFCs). The common coolants for heat rejection are air, water or liquids based on ethylene glycol in combination with water. In this work, a glycol-based coolant with triton x-100 was studied. The catalysts were prepared on a glassy carbon electrode. All electrochemical measurements were carried out in standard three-electrode electrochemical glass cells maintained at room temperature. 0.1 M H_2SO_4 was used as working electrolyte. The electrochemical measurements were performed by cyclicvoltammetry (CV) and oxygen reduction reaction (ORR), ECSA was determined.

Methods

Experiments were performed using a commercial catalyst 20 wt% Pt supported on Vulcan carbon XC-72 with Pt loading of 28 μg_{Pt} cm^{-2}. The catalysts were prepared on a glassy carbon electrode (∅ 5mm, 0.196 cm^2. The 0.1 M H_2SO_4 working electrolyte was prepared from nanopurewarter. Platinum was used as counter electrode, reversible hydrogen electrode for the reference electrode and glassy carbon as working electrode. The experimental procedure to study the effect of coolant containing ethylene glycol/water with the addition of the surfactant triton x-100 was developed. The loss of Pt electrochemical surface area (ECSA) due to "adsorbed" contaminate was calculated using the equation:

$$ECSA_{loss}(\%) = [(ECSA_{initial} - ECSA_{final})/ ECSA_{initial}]x100$$

Results and Discussions

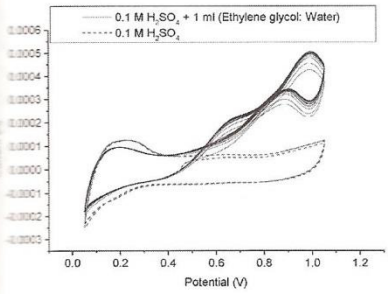

Fig. 1. CV of Pt/C catalysts in 0.1 M H_2SO_4 (initial CV, dashed line) and 0.1 M H_2SO_4 with 1 ml coolant (EG:Water)

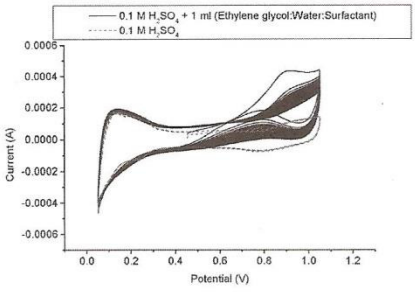

Fig. 2. CV of Pt/C catalysts in 0.1 M H_2SO_4 (initial CV,dashed line) and 0.1 M H_2SO_4 with 1 ml coolant (EG:Water:Surfactant)

As shown in Fig.1 and Fig. 2, an oxidation peak around 1.0 V and 0.9 V,respectively were observed in the anodic scan region. At the lower potentials, ethylene glycol adsorbs on the electrode surface and when the potential reaches 0.6-0.9 V, the current started increasing to the electrooxidation of ethylene glycol [2]. The loss of Pt (ECSA) was determined (1 ml coolant) with 22.92% and 27.72% respectively.

References

[1] Y. Garsany, S. Dutta, K. E. Swider-Lyons, Journal of Power Sources 216 (2012) 515-525.
[2] V. Selvaraj, M. Vinoba, M. Alagar. Journal of Colloid and Interface Science 322 (2008) 537-544.